Investigating the Curvature Effects of Substrates on Wrinkling Patterns through an Innovative Imaging Technique

Megha Emerse

A thesis submitted in partial fulfilment of the requirements of Nottingham Trent University for the degree of Doctor of Philosophy

September 30, 2023

Abstract

Patterns are ubiquitous in the world around us, often arising from underlying physical, chemical, or biological processes. Wrinkling patterns on thin elastic shells, such as dried fruits, are examples of such patterns, and can result from mechanical instabilities driven by differences in lengths and strains. Controlling these wrinkles on flat and curved surfaces made from various materials is vital for customising material properties and strengthening structures. The wrinkling of thin surfaces also has practical applications across a range of research fields, including flexible electronic sensors and displays, solar cells, optical gratings etc., and understanding the process of wrinkling is important for better control of such systems. This thesis aims to investigate the influence of substrate curvature on the characteristics of wrinkling patterns, and also involves the development of a novel imaging technology. The innovative imaging approach involves measuring surface topography using patterns of projected dots, and is implemented in MATLAB; accuracy and reliability are enabled through rigorous validation procedures. The research meticulously analyses key wrinkle characteristics, such as wavelength and amplitude, under both positive and negative substrate curvatures. A further segment of the work explores patterns on photonic wafers induced by laser annealing, and demonstrates the link of these patterns to the thermal treatments involved. Additionally, the study also includes an effort to obtain insights into pattern formation resulting from swelling in hydrogel materials like gelatin and polyacrylamide. Through this comprehensive exploration of wrinkling patterns and their dependencies on substrate curvature, this research contributes valuable insights to our understanding and manipulation of pattern formation. These findings have broad applications across scientific and engineering disciplines, enhancing the understanding of the intricate interplay between form and function in the natural world.

Acknowledgments

I would like to express my heartfelt gratitude to all who have played a pivotal role in shaping my PhD journey.

My director of studies, Dr. Lucas Goehring, has been an unwavering source of support and a true mentor throughout this research endeavour. His consistent encouragement, guidance and support with regular meetings, greatly contributed to my academic growth during my PhD journey. His dedication to my progress was instrumental in shaping the trajectory of my research.

I would also like to acknowledge my supervisor Dr. Kyle Baldwin and my independent assessor, Dr. Martin Bencsik, whose valuable feedback and evaluation have played a crucial role in shaping the quality and rigour of this thesis.

I am deeply appreciative of the collaboration with Dr.Demosthenes Koutsogeorgis and Dr. Nikolaos Kalfagiannis from Nottingham Trent University whose insights and contributions enriched the scope of my work.

Special thanks to the mathematical support from Dr. Mark Wilkinson for his invaluable input and expertise, which greatly enhanced and paved a new mathematical approach to this research.

I wish to express my profound gratitude to Nottingham Trent University for their generous funding of this research. I am truly thankful for the trust they placed in me by awarding me this scholarship.

To my dedicated lab mates, Tom and Mixon, your constant support and friendship have been instrumental in navigating the challenges of research. Your presence in the lab has made this journey more motivating.

Kartikeya Walia, my fellow PhD candidate and friend, has been an invaluable asset, not only for his technical assistance with MATLAB, 3D printing, and design aspects but also for his unwavering support, motivation, and time to help me, even amid his own workload.

I owe an immeasurable debt of gratitude to Appa, Amma and my brother, who have been the steadfast backbone of my life. Their unwavering support and belief in me have been my greatest motivation. I am deeply indebted to my beloved grandmother and grandfather, as they were the ones who initially planted the seed of pursuing a doctorate in me.

Finally, I offer my sincerest thanks to the Almighty God for guiding me through the journey of my PhD, bestowing upon me the strength, wisdom, and inspiration needed to complete this academic endeavour.

Contents

List of Figures

Chapter 1

Introduction

Nature is filled with an array of mesmerising patterns that arise from various mechanical and morphological instabilities, and some of these naturally occurring patterns are shown in Figure 1.1. These instabilities give rise to intricate structures and designs observed in natural phenomena, such as the branching patterns of trees, the intricate formations of seashells, the ripples in sand dunes, and the intricate network of veins in leaves [23–28]. Mechanical instabilities, driven by internal and external forces, play a fundamental role in shaping these patterns.

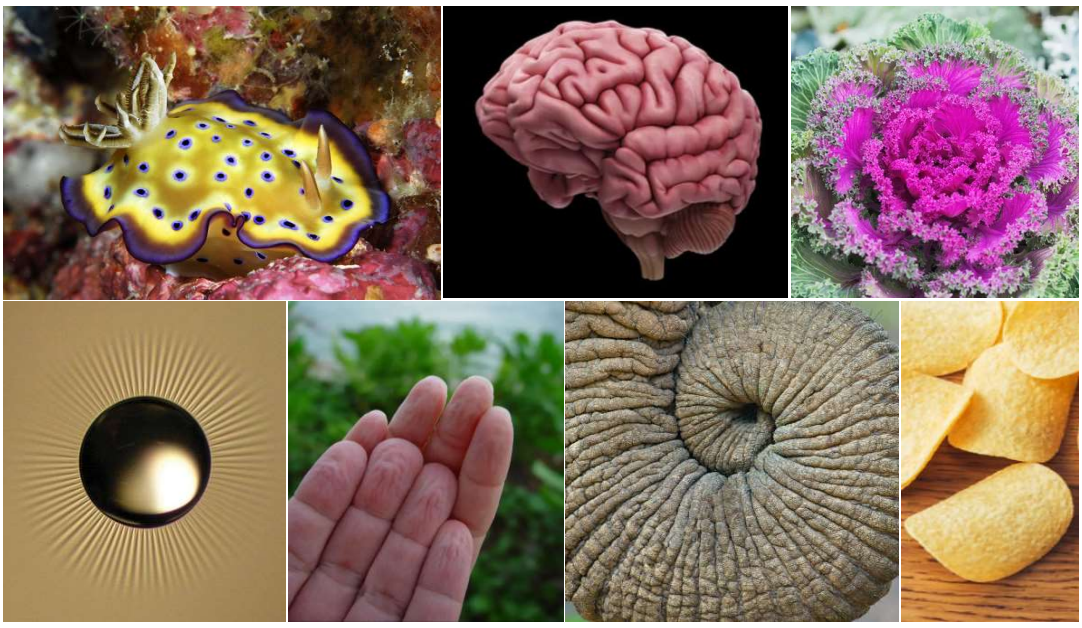

Figure 1.1: Examples of patterns due to mechanical instabilities like wrinkling, buckling, folding etc, seen around us in nature. From top left to right: Sea slug [1]; Folds and creases in the human brain [2]; ornamental cabbage [1]. From bottom left to right: A polystyrene film of diameter $D = 22.8$ mm floating on the surface of water wrinkled by water drops of radius $a = 0.5$ mm and mass $m = 0.2$ mg [3]; Fingers of a human hand showing the wrinkling when exposed to water for a long time; wrinkles on the trunk of an elephant [4]; and curved crisps.

In the natural world, soft materials are very common and important. They play a crucial role in helping living organisms adapt to the constantly changing and complex environments found

in nature. Many animals are primarily composed of soft tissues and do not have rigid or stiff skeletons. This includes a wide range of creatures such as jellyfish, inchworms, and octopuses etc [29–31]. Soft materials, such as elastomers and polymers, are very susceptible to mechanical instabilities and deformations when subjected to external factors or stimuli like mechanical forces, temperature changes, compression, electrical voltage or chemical interactions [16, 32–34]. When the amount of force applied to a material reaches a certain critical point, the smooth and stable condition of the material becomes unstable. At this point, the material undergoes changes in its structure or shape to reduce its overall energy, resulting in the formation of patterns of instability like wrinkles, creases, folds and ridges [16, 35–40].

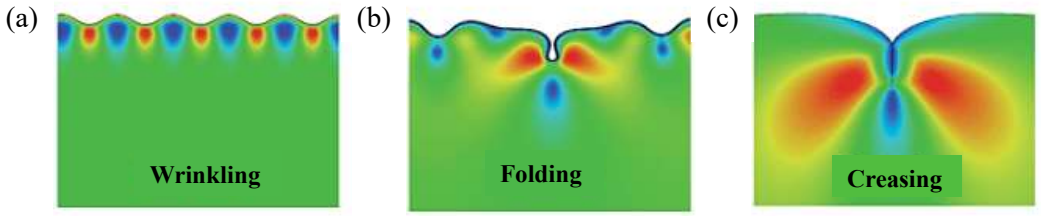

Figure 1.2: Schematic illustration of mechanical instabilities like (a) wrinkling, (b) folding and (c) creasing. Adapted from [5]

.

Wrinkling refers to the occurrence of periodic or irregular surface ripples on a previously flat surface [24, 36] as shown in Figure 1.2 (a). Given that wrinkles naturally develop on a film when stress exceeds a specific threshold, this makes it an appealing choice for applications that favour the cost-effective production of large-area surface patterns More detailed descriptions of wrinkling and different works on wrinkling patterns are discussed in the following section.

In contrast, creasing typically happens on the surface of soft materials without rigid exteriors. It occurs when a smooth surface transforms into a self-contacting shape with a sharp ridge or furrows [41–43] as illustrated in Figure 1.2 (c). Unlike wrinkles, which are often more subtle, creases represent a higher degree of deformation and are typically localized in nature [42, 44]. Creases are also a common characteristic of various origami creations, where precise folding techniques are employed to achieve desired shapes.

Folding, describes the formation of localised, deep surface valleys as a result of buckling. Folds are often visible during the development of surface wrinkles in a rigid layer attached to a soft substrate or floating on a liquid [45–47] as given in Figure 1.2 (b). They often manifest on a larger scale compared to wrinkles and can be smoother and less sharp than creases. Folds typically occur in flexible materials like cloth or paper when they are manipulated or bent.

Understanding the mechanisms behind these mechanical and morphological instabilities in nature is not only scientifically intriguing but also holds significant practical implications. For example, researchers and engineers draw inspiration from these patterns to design and optimise materials, structures, and technologies in various fields, including architecture, materials science, flexible electronics, biomimetics, and even art [47–49]. By studying the patterns that emerge from mechanical and morphological instabilities in nature, gain a deeper appreciation for the intricate beauty and complexity of the world around us while unlocking new possibilities for innovation and problem-solving.

1.1 What are wrinkles

When a bilayer structure consisting of a stiff, thin film on a compliant, thick substrate is subjected to compression beyond a critical load, it initiates the formation of wrinkles as a stress-relief mechanism. These wrinkles manifest periodically within a confined region. The wavelength of these wrinkles is determined by a balance between the substrate's deformation, which favours shorter wavelengths, and the bending of the film, which prefers longer wavelengths [45, 50–52].

Wrinkling can be induced through at least three different external stimuli:- thermally, mechanically or by swelling/osmotic stresses [53]. Wrinkles in bilayer films due to temperature changes occur in two primary scenarios: firstly, when a thin, stiff layer sits atop a thick, flexible substrate, resulting in wrinkles during cooling as thermal stress exceeds a critical compressive threshold; secondly, when a heated thin bilayer film with a metal layer over a glassy polymer experiences temperature-induced stress. These stresses may arise from differences in thermal expansion coefficients or from processes like atomic peening during film deposition [16, 33, 49, 54]. Swelling, often triggered by substances like solvents, provides an alternative method to generate wrinkle patterns in bilayer thin films or thick gels with varying stiffness properties [55–57]. This process involves meticulous control of factors such as the speed and quality of solvent diffusion, the extent of crosslinking in the film, etc. As the polymer film swells, it undergoes a significant change in volume. However, since the film is firmly attached to a rigid substrate, only the top layer can freely expand. This creates uneven osmotic pressure within the film, leading to biaxial compressive stress on the film's surface [53]. Mechanically induced wrinkles are generated by applying controlled physical forces to a material, distinguishing them from wrinkles caused by external factors like temperature or swelling. Researchers have created these wrinkles through methods like stretching or compressing the material, allowing them to control the magnitude and direction of strain independently. This fine control enables the real-time formation of intricate wrinkle patterns, including organised structures like two-dimensional zigzag herringbone

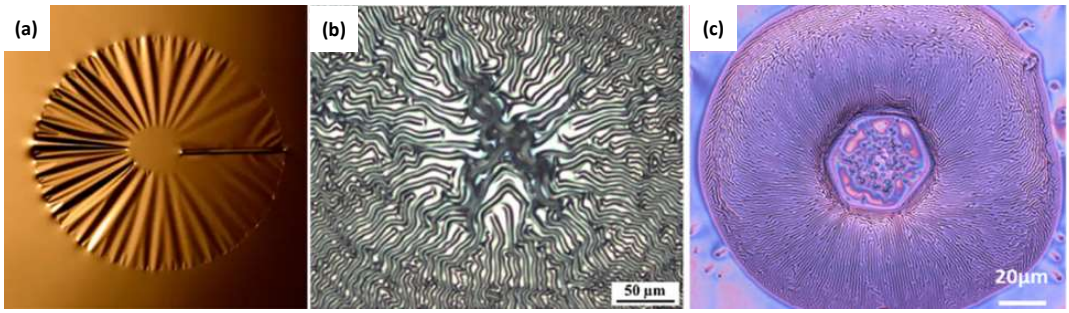

Figure 1.3: Wrinkle patterns on planar substrates. (a) A thin polymer film with an annular shape that is floating on water [6], (b) image showing the surface morphology of molybdenum (Mo) thin films sputter-deposited on uncrosslinked gel substrates with thickness of h = 135 nm, (c) Microscopic images depicting the emergence of gold (Au) wrinkles on PDMS circular structures [7].

patterns [58]. Some of the wrinkle patterns observed in different flat substrates are shown in Figure 1.3. Mechanically induced wrinkles find applications in diverse fields, such as thin-film measurements, surface wettability manipulation, liquid crystal displays, adhesion technologies, cell alignment, and flexible electronics [31, 59, 60].

Increasing evidence suggests that mechanical forces are influential in shaping the forms of living organisms. Controlled wrinkling, a process where patterns naturally emerge, has been demonstrated to generate complex patterns on both flat and curved surfaces. Although extensive research has focused on understanding wrinkling on flat surfaces in recent decades, the majority of natural wrinkling occurs on curved biological surfaces. Unfortunately, the investigation into deliberately creating patterns on these curved surfaces remains relatively underdeveloped. The study of wrinkling is not only of scientific interest but also has practical implications. Understanding the factors influencing wrinkling behaviour is crucial in fields such as flexible electronics, where thin films are extensively used. By controlling these wrinkling processes, researchers and engineers can design and optimise flexible electronic devices, stretchable sensors, and other applications where surface morphology plays a significant role.

1.2 Curvature induced wrinkling

Curvature is a mathematical measure that quantifies how much a curve or surface deviates from being straight or flat [61, 62]. The curvature (κ) of the curve at a point P is defined as the magnitude of the derivative of the unit tangent vector $\mathbf{T}$ with respect to arc length s, where $\kappa = \mid d\mathbf{T}/ds \mid$ where $d\mathbf{T}/ds$ represents its rate of change with respect to arc length [62]. The

curvature at a point P on the surface is more complex and can be defined in terms of the principal curvatures κ_1 and κ_2 and the Gaussian curvature κ is the product of the principal curvatures κ_1 and κ_2. The principal curvature κ_1 and κ_2 is the maxima and minima values of curvature at a point on a surface and is the inverse of the radius of curvatures R_1 and R_2.

Most research in the past has mostly focused on making and using wrinkled patterns on flat (planar) surfaces. But, there hasn't been much research looking into how these patterns form on curved surfaces and how these patterns are affected by curvature. This gap in research is a chance for a detailed study that looks at how these patterns form on curved surfaces and how these patterns can be controlled. Surface curvature is a critical factor in determining the patterns of wrinkles that form and how they transition in certain materials and structures, specifically in core-shell configurations and curved film/substrate systems.

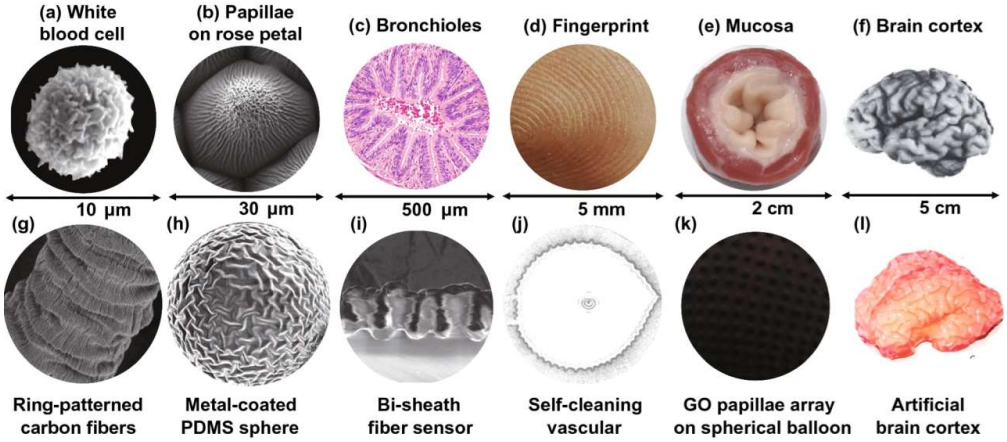

Figure 1.4: Wrinkle formations on curved surfaces occur naturally in a variety of sizes, spanning from a to f in natural settings and from g to l in controlled laboratory environments, encompassing various length scales. Adapted from [8].

Recent research indicates that in a curved bilayer system, several key factors play a significant role in the evolution of wrinkling patterns [63, 64] in daily life as shown in Figure 1.4. These factors include curvature, modular ratio, and overstress, which have been studied extensively in recent works [65–69]. In a recent study, the main focus was on examining how the wrinkling patterns change over time on torus-shaped structures with uneven curvature using finite element simulations. These earlier investigations were instrumental in enhancing the comprehension of how curvature impacts the development of wrinkling patterns. When the modular ratio and overstress values are fixed, the magnitude and direction (sign) of curvature become crucial. This not only determined the specific conditions under which surface wrinkling begins (critical conditions for wrinkling onset) but also the triggered transitions in the wrinkling patterns themselves.

This means that in a curved system, the characteristics of curvature can lead to a wider variety of wrinkling patterns compared to a flat (planar) system, especially when subjected to simple loading conditions. For instance, consider a film-substrate system as an example, a flat film-substrate system typically exhibits sinusoidal wrinkling patterns when subjected to uniaxial compression [57, 70]. Whereas, when a thin elastic shell adheres to a substrate with a different shape, such as a spherical shell on a flat surface, mechanical incompatibilities arise due to the mismatch in curvatures [71, 72]. This, too, can lead to the development of wrinkles and folds in the shell as it attempts to conform to the shape of the substrate.

Nevertheless, the phenomenon of wrinkling pattern transformations caused by curvature in three-dimensional curved systems has only been theoretically explored quite recently. These studies primarily focused on spherical and cylindrical core-shell systems [65]. In the case of a spherical core-shell structure subjected to compressive stresses, an initial hexagonal pattern emerges and can subsequently transform into bistable and labyrinth phases under loading [73, 74]. However, in the case of a cylindrical core-shell system subjected to axial compression, the initial axisymmetric sinusoidal wrinkling mode can transform into a diamond-like pattern. This transformation depends on the specific values of the modular ratio and curvature in the system [75]. Essentially, the curvature in such systems has the power to alter the nature of wrinkling patterns, resulting in more diverse outcomes compared to flat systems.

In the realm of biological systems, the study of curvature-induced buckling and morphological changes provides crucial insights into the mechanisms governing growth, development, and adaptation. For instance, the intricate patterns of wrinkles on the skin of certain animals like elephants, camouflage [76] and the undulating shapes of plant leaves are a direct result of the interplay between curvature and underlying mechanical forces [1]. When different parts of these structures have varying rates of expansion or contraction, changes in moisture content within the material, etc create stress within the material, leading to the formation of wrinkles and folds. This phenomenon has been extensively studied and understood in the context of natural systems, where growth processes and environmental factors contribute to these mechanical instabilities.

The intriguing question raised is whether these inherent incompatibilities in length or curvature can be intentionally harnessed to design and control complex wrinkled surfaces. In other words, can we manipulate these mechanical instabilities to create specific patterns of wrinkles and folds for various applications? This concept has significant implications across multiple fields, including materials science, engineering, and design. Developing standardised methods for quantitatively characterising wrinkling patterns, including metrics for measuring wrinkle wavelength, amplitude, and orientation, can help compare results across different studies and improve our understanding of the underlying physics. This research focuses on studying how the signs of

curvature of thin films affect the wrinkle characteristics.

1.3 Applications of wrinkling

Wrinkling patterns have a wide range of applications in different fields. The characteristics of wrinkles, such as their size, period, and height distribution, are of paramount importance in various applications, particularly in optical gratings. Precise control over these wrinkle attributes enables tailored light manipulation and improved optical performance. For instance, investigations are done to significantly enhance light in-coupling and retro-reflection, leading to better energy harvesting in solar cells and reduced glare in optical systems by optimising wrinkle size and arrangement [77, 78].

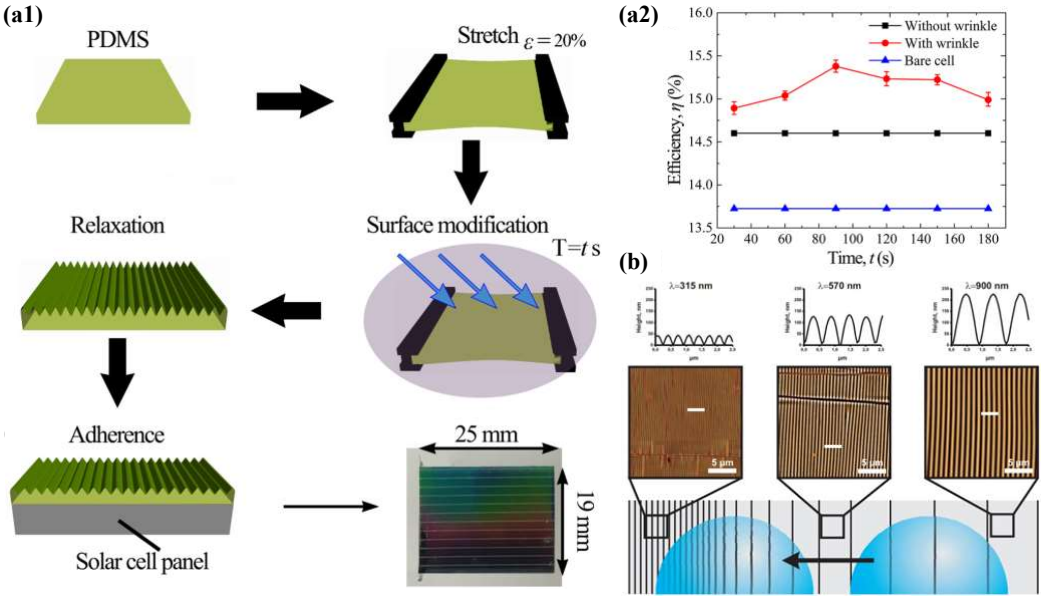

Figure 1.5: Applications of wrinkling patterns. (a1) steps involved in synthesising PDMS-based solar cell anti-reflective layer featuring structured wrinkles, along with the encapsulation of the solar cell, (a2) plot showing the conversion efficiency versus plasma treatment time and (b) illustration depicting the autonomous motion of a droplet on a hierarchical wrinkled surface featuring a gradient structure [9, 10].

Similarly, controlling the amplitude and wavelength of wrinkles can optimise light trapping and photon absorption, enhancing solar cell efficiency as shown in Figure 1.5 (a1) and (a2). It was investigated that the formation of wrinkles and deep folds on polymer surfaces under mechanical stress serves as a means to direct and trap light within the photo-active regions of photovoltaic devices. Utilising such textured surfaces has led to significant enhancements in light

absorption efficiencies, notably in the near-infrared spectrum, where light absorption is typically limited [79]. The study demonstrates a substantial boost in the external quantum efficiency of polymer photovoltaics, surpassing a 600% increase in the near-infrared range. This expansion in the useful range of solar energy conversion extends beyond 200 nm, showcasing the potential for significantly improved photovoltaic performance in this critical spectral region.

Wrinkles were utilised to induce the autonomous motion of droplets which had applications in microfluidics [10, 80, 81]. When a water droplet is placed on a surface with gradient wrinkling, a noticeable difference in contact angle can be observed between the two sides of the droplet along the gradient direction. This discrepancy in surface tension leads to the movement of the droplet on the gradient wrinkling surface, specifically from regions with larger wavelengths and amplitudes to those with smaller scales, as depicted in Figure 1.5 (b) [9]. The self-driven motion of the droplet on the gradient wrinkled surface presents novel possibilities for microfluidic devices. Besides these applications mentioned in this section, there are more applications in the field of wrinkles which include flexible electronics, reverse patterning, bio-sensors, controlled wettability etc, [56, 81–84].

1.4 Thesis organisation

This thesis has seven chapters including this introduction chapter and a chapter including the summary and the conclusion. Briefly, these chapters will cover the following topics

Chapter 2: Methodology

It is evident from the discussion in Chapter 1 that it is important to study the wrinkling characteristics of curved films. Chapter 2 discusses the different techniques and methods used in this research for the fabrication of the desired thin curved films for further analysis. This included designing and manufacturing the required curved substrates, followed by the development of the polymer thin films. Since this was an iterative process, multiple variations of this design process have also been mentioned. To ensure the reliability of the film fabrication methods, optical coherence tomography was utilised.

Chapter 3: Imaging of wrinkling patterns

A detailed description of the imaging technique developed for tracing the wrinkled topography is discussed in this chapter. This chapter also includes a detailed explanation of the optical theory

followed for determining wrinkle characteristics like amplitude and wavelength. Image analysis was done using the MATLAB programming environment. A detailed discussion of the algorithms used, including the interpolation methodologies is also presented. This is followed by the validation procedure implemented to ensure the reliability of the developed imaging technique.

Chapter 4: Effect of curvature on wrinkling patterns

The developed imaging methodology was used to study the wrinkling pattern of several curved thin films with different Gaussian curvatures. Chapter 4 experimentally verifies the mathematical predictions made in the literature regarding the path and direction of wrinkle formation on thin films. Furthermore, this chapter elucidates the effect of curvature on wrinkle characteristics like wavelength and amplitude with curvature. This chapter reinforces the hypothesis and predictions made regarding the relations between the wrinkle characteristics and the curvature the inherent curvature of thin films.

Chapter 5: Wrinkling patterns on photonic wafer

In contrast to the film curvature leading to wrinkle formation in Chapter 4, Chapter 5 explores the phenomenon of wrinkle formation due to the strain mismatch between silicon and its oxide layer. This effect becomes apparent as a consequence of variations in the cooling process within these layers following laser annealing. The methodology for the preparation of the silicon wafer sample is also discussed in detail. An advanced imaging technology, called atomic forced microscopy (AFM) was employed to observe the nanoscale patterns formed which is followed by further processing and analysis.

Chapter 6: Swelling kinetics of hydrogel

This study extends its scope to explore swelling-induced patterns on three-dimensional polymer samples, including spherical and cuboidal shapes. Furthermore, a discussion is included that relates the swelling of these specimens to the pH of the solution. The study also examines the evolution of swelling patterns over time on off-the-shelf spherical polymer beads, which are used as a reference for synthesising spherical beads and films, confirming the similarity of the patterns observed in the samples. This chapter also highlights the potential of using different polymers for the exploration of pattern formation on curved substrates.

Chapter 7: Summary and conclusion

This chapter summarises the developed methodologies for curved and hemispherical thin films, photonic wafers and three-dimensional polymer samples. The main findings and results highlighting the underpinned relationships between the curvature and the characteristic features of the patterns and wrinkles are discussed. Additionally, the limitations and the future possibilities of the methodologies developed are critically mentioned. To sum up the research work a conclusion including the main contributions to the knowledge and literature in the domain of soft-polymers is also included.

1.5 Research aim and objectives

This section enlists the main aims and objectives of this research study.

- To develop a reliable method for the synthesis of curved elastic thin films.
- To quantify the effect of curvature on the wrinkling patterns formed on the curved thin films.
- To develop a robust imaging methodology for mapping the wrinkle characteristic features like wavelength and amplitude.
- To study the patterns formed on photonic wafers and analyse the dependence of the pattern features on the thickness of the wafer substrate's oxide layers.
- To study swelling and swelling-induced pattern formation on three-dimensional polymer cubes and spherical beads.

Chapter 2

Methodology

As discussed in Chapter 1, there is a clear gap in the literature regarding the understanding of the wrinkling characteristics and their relations to the curvature of the elastic thin films. To understand and determine these characteristic features, it was imminent to fabricate the curved thin films for further experimentation and analysis. This chapter includes the various fabrication techniques and processes adopted and tested for reliable and reproducible manufacturing of these elastomeric films. Throughout the research study, several processes were undertaken during the fabrication which included a mould design, 3D printing, thermoforming, polydimethylsiloxane (PDMS) preparation, and thickness measurement using optical coherence tomography(OCT).

An elastomer called Polydimethylsiloxane (PDMS) was used for the fabrication of the thin films. It was desirable to fabricate a hemispherical and saddle-shaped film to study both positive and negative Gaussian curvature surfaces. To achieve a robust methodology for film fabrication several iterations were done. The first step was to manufacture a substrate which was done using two different 3D Printing technologies as explained in 2.1. The PDMS coating methods included drop-casting, with the inverted orientation being optimal for hemispherical substrates and the inclined orientation achieving the desired uniform film thickness for saddle-shaped substrates. To ensure proper curing of the PDMS material at lower thicknesses, a preferable material for the substrate fabrication was identified as High Impact Polystyrene (HIPS). To overcome the limitation of 3D printing HIPS with high accuracy, a precise 3D-printed mould was used to vacuum thermo-form an HIPS sheet and achieve the final mould for a reliable and reproducible methodology.

2.1 Mould design, 3D printing, and thermoforming

This work focuses on utilising an anticlastic shape, a surface that is curved in two opposite directions, as shown in figure 2.1. The presence of both a positive and a negative principle curvature allows the possibility of studying novel effects of curvature on the formation of wrinkles. The effect of positive Gaussian curvature (shells) on wrinkling patterns has already been studied in the literature [13, 14]. A saddle-shaped mould that has negative Gaussian curvature (orthogonal

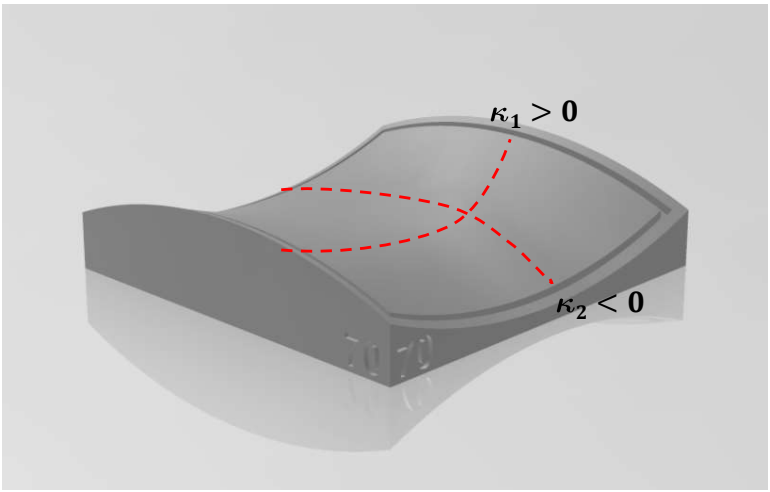

Figure 2.1: Computer-aided design (CAD) of an anticlastic (saddle-shaped) mould showing the positive and negative curvature in the shape, respectively κ_1 and κ_2.

positive κ_1 and negative κ_2 principal curvatures), as given in figure 2.1, is key to this study.

Autodesk Fusion 360 was used to develop a 3D computer-aided design of the mould. Fig. 2.2 illustrates the design process utilised for designing a saddle shape ($\kappa_1 = 1/R_1$ and $\kappa_2 = -1/R_2$, where R_1 and R_2 are the two required radius of curvatures). Fig. 2.2 (a) shows a rectangle with the required dimensions (50 mm x 50 mm) of the saddle shape projection. This was followed by the creation of two perpendicular planes passing through any two adjacent sides of the rectangle (Fig. 2.2 (b)). On one of the planes (Fig. 2.2 (c)), two circles with a radius value equal to $R_1 = 70mm$ were created with the opposite vertices of the edge as centres (Fig. 2.2 (d)), respectively. It should be noted that the two circles intersect at two points in space, both above and below the projected plane. For creating a positive curvature the intersection point below the projected plane was chosen as a centre and another circle with radius = R_1 was created and all the extra construction lines were removed as shown in (Fig. 2.2 (e)). A similar process was followed for the second perpendicular plane with a radius equal to R_2 (Fig. 2.2 (f and g)). For a negative curvature, the centre of the circle lies above the perpendicular plane (Fig. 2.2 (h)). Both positive and negative curvature arcs (Fig. 2.2 (i)) were then projected to the respective parallel planes passing through the opposite edges of the rectangle (Fig. 2.2 (j)). With all four curved edges a surface was formed (Fig. 2.2 (k)). The projection of the curved surface was created at a distance equal to the desired width of the mould (15 mm at the wider end) (Fig. 2.2 (l)). This was then extruded up to a value greater than the desired width (25 mm) (Fig. 2.2 (m)). The formed solid cuboid was then divided using a 'Split' command with the formed saddle surface as the tool (Fig. 2.2 (n)). The top half was removed (Fig. 2.2 (o) and the remaining bottom half

was the desired saddle-shaped mould (Fig. 2.2 (p)). Fusion 360 is a parametric software, which means it allows for easy modification of the parameters. This helped simplify the design process of the saddle-shaped moulds with various curvatures without the need for re-designing.

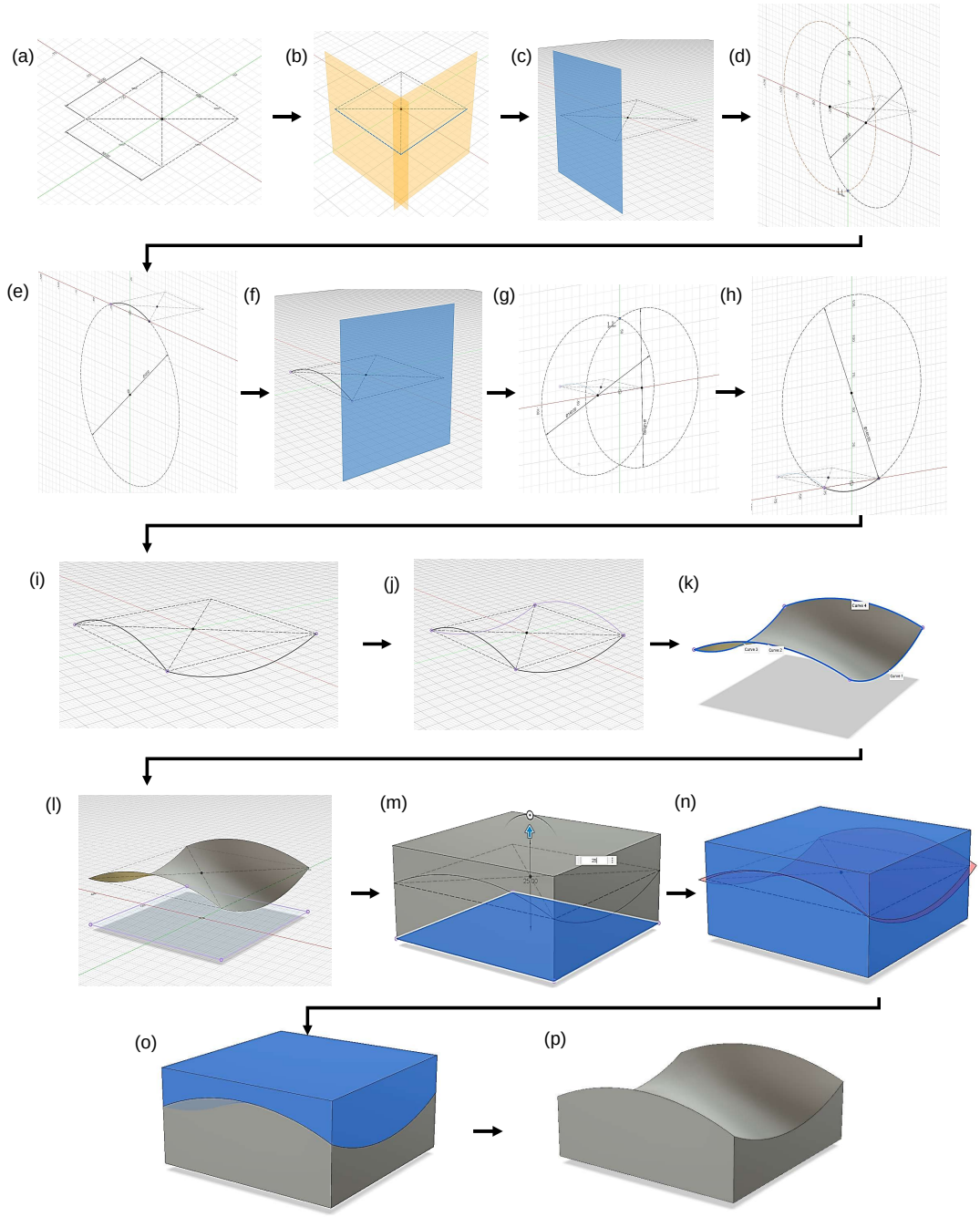

Figure 2.2: The figure shows different steps involved in designing the saddle-shaped surface using Autodesk Fusion 360.

Once the design was ready, the moulds were fabricated using 3D printing. 3D printing or Additive Manufacturing is a digital fabrication methodology to create physical objects by gradual addition of material layer-by-layer [85]. In this technology, the object is manufactured by layer deposition of materials like ceramic, metals, polymer and resins according to the design requirements [86].

As an initial trial experiment, the saddle-shaped mould was 3D printed using the material called polylactic acid (PLA) using the Fused Deposition Modelling (FDM) technique. Moulds formed using PLA via the FDM technique have a poor vertical resolution and create undesirable stair-like artefacts (i.e., printed parts have a higher layer thickness and visibly evident steps on the curved surfaces) which affect the further fabrication of the thin film samples. Another limitation with the mould formed using PLA was its low heat deflection temperature (HDT of 52 °C, the temperature at which the polymer becomes pliable/deformable). This is essential for subsequent procedures involving the coating of moulds with the desired polymer material (PDMS), considering the curing temperatures of around 80°C.

Alternatively, a photo-polymer high-temperature resin was used in this research to compensate for these limitations of the PLA material. Additional benefits come from the underlying printing process for this type of material, i.e., a more accurate 3D printing technique called stereo-lithography (SLA). Using SLA, a dimensional accuracy of ±140 microns in the X-Y plane (horizontal) of the digital model, over 80 per cent of surface points, was achieved when printed on a 100-micron (vertical resolution) print setting. Formlabs Form 2 3D Printer was used to manufacture the prototypes using the Formlabs High-Temperature v2 photo-polymer engineering resin. This photo-polymer resin has a high heat deflection temperature (HDT of 238°C @ 0.45 MPa) and offers better thermal stability for the required curing temperatures of approximately 80°C. The SLA technique has two further stages of post-processing, which makes the 3D printed part realise its optimum material properties. For High Temp v2 resin, a 6-minute isopropyl alcohol (IPA) wash process [87] is required for the removal of any uncured excess resin, followed by a 120-minute UV curing in a heated chamber at 80 °C [88].

Moulds with a high HDT also allowed for further experimentation with thin fabrication methods, for instance using vacuum thermo-forming as discussed in section 2.2.

This was followed by the drop-casting of the PDMS solution to form a thin film. Due to the dual curvature of the surface, the inverted curing method resulted in a pool of excess PDMS material, and in turn variable thickness of the film, in the sections with negative curvature.

With the photo-polymer resin, a few trials were done regarding the casting of PDMS to get a uniform deposition. For this, multiple iterations of the substrate designs were made, which included a stackable version for the saddle-shaped surface and a mirrored part (highlighted in

figure 2.2 (o)) with a spacer frame sandwiched between the two (FIG). In this design, two small holes were included on the top surface, so the PDMS could be poured through one hole to fill the mould. The objective of this was to obtain a uniform thickness of the film with no surface defects. This design ensured a uniformity of thickness but was difficult to handle, and was not immune to leakage of excessive material. Additionally, a constraint of this method was the minimum printable thickness of the spacer (1 mm) without losing its structural integrity, which is significantly greater than the desired thickness of the thin films intended for this work. Another limitation of this design was the improper curing of the PDMS, due to the surrounding mould, as the PDMS material requires a decent amount of air circulation to cure. This methodology resulted in partially cured, thicker films with irregular edges.

Figure 2.3: CAD models of the saddle-shaped moulds with a negative curvature of $\kappa_2 = 70$ mm but different positive curvatures ranging from $\kappa_1 = 40$ mm to 130 mm.

A simple saddle shape mould with excessive dimensions was identified to be a preferable solution. A circumferential 2.5mm border was provided to fabricate a bigger film and later trimmed to the desirable dimensions with straighter edges in the thin film.

Multiple substrates were then created using a base dimension of 55 mm x 55 mm, a fixed negative curvature of 70 mm, and a positive curvature ranging from 40 mm to 130 mm, as shown in Fig. 2.3. Two batches of 5 moulds each were 3D printed, with a total printing duration of 12 hours. With fewer components to handle, the process became more straightforward and more focus was then imparted on achieving proper curing and a uniform thickness of the film. To achieve a uniform thickness various coating and curing orientations were tested which are

explained in section 2.2 in detail.

Another difficulty that remained was the improper curing of the PDMS thin films. After a few PDMS casting experiments on the photo-polymer resin moulds, it was observed that the resin used to print the mould was acting as a chemical inhibitor, which curbed the cross-linking of the PDMS polymer [89]. In order to overcome this problem, suggestions in the literature involve long-duration post-curing recipes [89] and coating the topmost surface of the substrate with a material like epoxy resin or a product called Inhibit-X [90]. However, implementing these solutions would have extended the preparation time and could have altered the curvature properties of the films, potentially introducing irregularities due to human error associated with applying additional coatings.

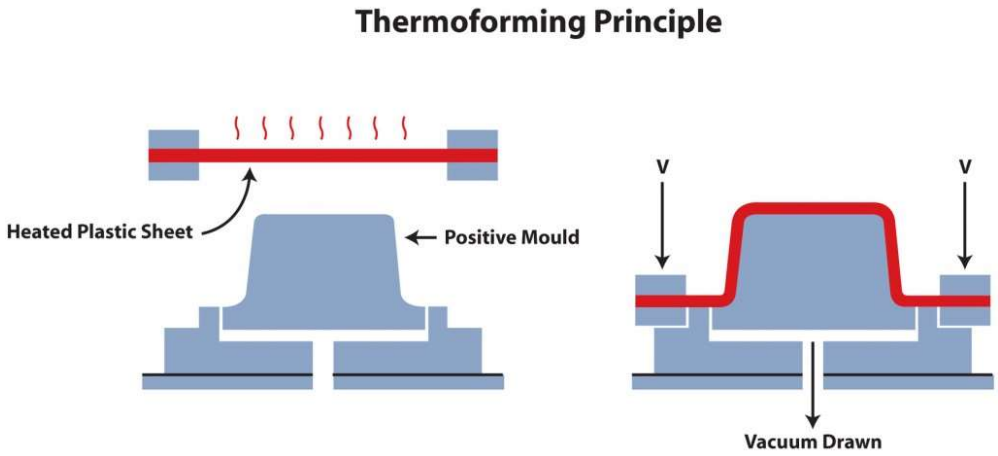

Figure 2.4: Schematic diagram on how thermoforming works. Adapted from [11].

The solution was to use a material that does not inhibit the PDMS curing and also has the required temperature properties. Therefore, High Impact Poly-Styrene (HIPS) was selected as the appropriate material. Since, HIPS is not a photo-polymer resin and cannot be 3D printed using SLA, although it is possible with FDM, which was undesirable, an alternative approach was employed. This approach involved thermo-forming a HIPS thin sheet of thickness 1.5 mm over the high-temperature 3D printed moulds.

Thermoforming is a technique in which a thermoplastic sheet is pre-heated to its heat deflection temperature [91]. The sheet of plastic is heated until it becomes soft and flexible. Then, it is carefully stretched over a mould with the desired shape. As the plastic conforms to the mould, a vacuum is used to create suction, which helps the plastic take on the exact shape of the mould as shown in the schematic in figure 2.4. Post this, the plastic is allowed to cool down, keeping the moulded shape, and the mould is removed. This was also a suitable solution as the thermo-forming temperature of polystyrene is 150-190°C (also its HDT value) and the moulds

manufactured using the high-temperature photo-polymer resin are thermally stable up to this temperature. This also offered benefits like a lack of adhesion between the PDMS and the mould, a reduction in the time for manufacturing multiple moulds (from an average of two or hours in 3D printing to only one minute using thermo-forming), and uniform and identical curvatures. Once the polystyrene moulds were fabricated the next step involved the preparation of the curved thin-films which is explained in the section 2.2.

2.2 PDMS thin film preparation

Polydimethylsiloxane, commonly known as PDMS, is a silicon elastomer that has a wide range of uses in the field of research, the polymeric industry, etc [92–95]. It is mainly known for its thermal and chemical stability, bio-compatibility, flexibility, hyperplastic characteristics, ease of use, and low cost [94,96]. PDMS is formed by mixing together two components which are the base and the crosslinker. The base initiates and facilitates the polymerisation of siloxane monomers to form PDMS chains, while the crosslinker introduces crosslinks between these chains to create a solid elastomeric material. During the curing process, heat is applied to the base and crosslinker which causes a silyl hybrid group to form as a result of contact between an allyl or vinyl group and the silicone. As they combine, the PDMS base and curing agent harden, creating a network structure of chemical links between the polymer chains. This process is known as cross-linking [94, 97]. Regarding the mechanical properties of PDMS, the elastic modulus of PDMS has been variously reported as between E= 1.32 and 2.97 MPa, and its tensile strength is between 0.57 and 3.17 MPa. These properties vary depending on the ratio of the curing agent and the elastomer base and also on the curing temperature. Throughout this work, a 10:1 ratio of 184 Sylgard elastomer base(DOW) and the 184 Silicone elastomer curing agent which was the standard protocol was used as per the manufacturer specification. Once the base and the curing agent were poured out in the required ratio, they were mixed thoroughly and were left for degassing in a vacuum chamber for 30 minutes, which removed the air bubbles formed in the mixture.

The Young's modulus of fully cured PDMS was measured through a tensile test. A PDMS specimen (110 mm × 10 mm × 5.7 mm) was prepared with a 1:10 base-to-crosslinker ratio and was tested in a universal tensile tester (MultiTest 2.5- dV, Mecmesin, UK). Each test was set to a 10% extension from the initial specimen length. Figure 6 shows the resulting stress–strain curves with a 10:1 base-to-crosslinker ratio. Young's modulus was estimated by the slope of a linear least-squares fitting to the extension data (red dotted line). The estimated Young's modulus was 2.2 MPa within the range of literature values and the Poisson's ratio was assumed to be 0.5 which implies the material does not significantly change in volume when subjected to a uniaxial

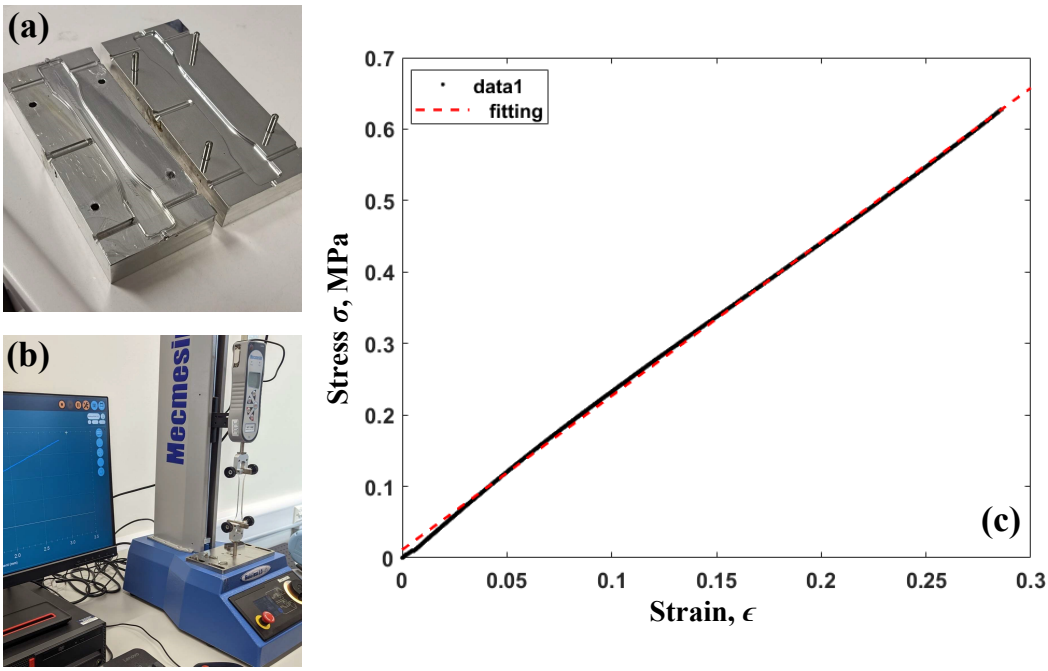

Figure 2.5: Tensile test of PDMS (a) PDMS specimen cast on the dog-bone specimen mould for the tensile test.(b) Image showing the specimen on the tensile testing machine. (c) The stress-strain graph for the 10:1 ratio of PDMS specimen with Young's modulus of $E = 2.2 \pm 0.12$ MPa.

load in one direction [98, 99].

The PDMS solution prepared was then used for the fabrication of the thin films for further experimentation. The desired curvatures to be analysed involved both hemispherical and saddle-shaped substrates. The hemispherical substrates with various Gaussian curvatures were procured off-the-shelf and the saddle-shaped substrates were manufactured in-house as explained in section 2.1.

To coat these substrates, the preferred technique was drop casting, particularly suitable for creating thin-film shells on curved substrates, as noted in [100]. When dealing with hemispherical substrates, gravity-assisted drop casting was effective even in the inverted orientation. However, it failed to yield consistent results with uniform thickness when applied to saddle-shaped substrates. This discrepancy can be attributed to the negative Gaussian curvature of the saddle-shaped form, contrasting with the positive curvature of the hemispherical mould. In the case of the hemispherical substrate, gravity-assisted flow exhibited a consistent downward longitudinal flow-velocity field along both principal curvatures, resulting in a uniform shell thickness post-curing. Conversely, as depicted in the figure, the same downward longitudinal flow-velocity field led to excessive material deposition, as shown in the figure, for the saddle-shaped substrate. To address this observed thickness irregularity in the film, an alternative inclined orientation was

employed. This was done by alternatively positioning the mould at different inclinations (45 °, alternatively, along all edges of the mould) for curing instead of an inverted position, after the drop-casting of the PDMS material. This ensured a proper flow of the material under gravity in all directions and also allowed for the excess material to outflow from the mould. However, it's important to note that this approach introduced a degree of human influence due to the gradual reduction in material flow during the curing process.

The number of coatings on the mould depends on the thickness required for the experiment. One coating of PDMS resulted in an approximate thickness of 30-40 µm, therefore to achieve the desired thickness multiple (three) coatings were done. Then the mould was left undisturbed and covered in order to avoid any unwanted particles or dust from getting stuck into the poured PDMS solution. Once the required thickness was attained the moulds are kept in the oven at 80°C for 4 hours in order to cure the PDMS. After curing, the films were carefully peeled off of the moulds and taken to an optical coherence tomography (OCT) to have their thickness measured as described in section 2.3. To ensure ease of removal of the fabricated delicate thin films from the moulds, the moulds were pre-processed (before the PDMS coatings) with a thin coating of a PVA (Polyvinyl alcohol). This reinforced the PDMS material and prevented any damage during the peeling process post-curing. After the OCT measurements and before the wrinkling stages (discussed in Chapter 3, the films were dispersed in water in different Petri dishes to allow the PVA layer to partially dissolve which made it easy to remove from the PDMS. The PVA layer was then removed carefully with a paintbrush and the PDMS films were cleaned thoroughly with deionized water to make them fully transparent before performing any experiments.

2.3 Measurement of film thickness using OCT

The thickness of the PDMS films is an important parameter in this work. There are different techniques to measure the thickness of the film such as ellipsometry, optical profilometry, scanning probe microscopy, interferometry etc. But in this research optical coherence tomography (OCT) was used to measure the thickness of the thin film because of its high axial resolution. The high depth and transversal resolution of OCT, and also the fact that its transverse and depth resolutions are independent, the high probing depth in scattering media, the contact-free and non-invasive operation, and the ability to develop various function-dependent image contrasting methods are its specific advantages.

OCT is analogous to the ultrasound B scan, the main difference is that instead of sound, OCT uses light. The first step in OCT imaging is measuring the axial distance within the sample or the material. Light originating from the source is divided into two separate paths using a beam

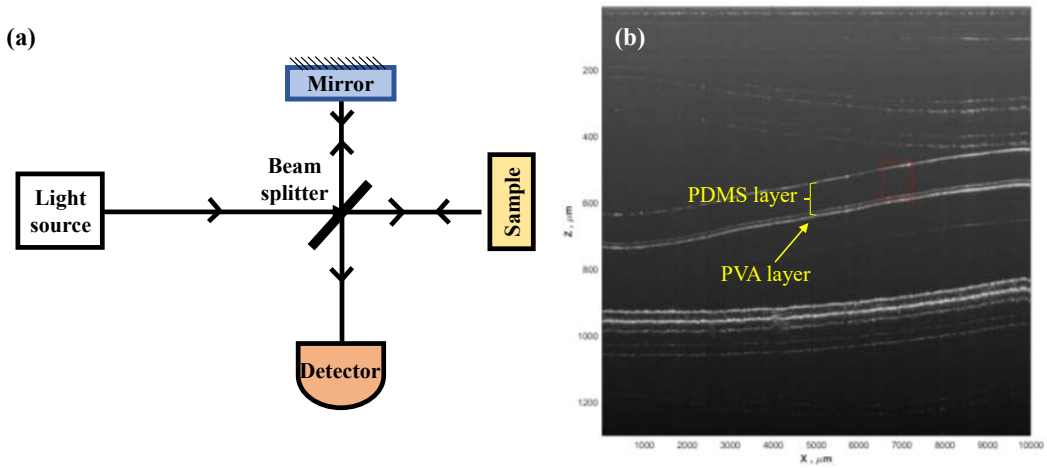

Figure 2.6: Schematic of OCT. (a) shows the schematic diagram of the FD-OCT. This OCT which is used in the thesis employs a stationary reference mirror coupled with a spectral detector. (b) shows the scanned OCT image of PDMS films with a PVA layer.

splitter, often referred to as a dichroic mirror [101, 102]. One of these light paths is directed towards the sample, while the other is directed towards a reference mirror. After interacting with the sample and reference mirror, the reflected light from both paths is recombined at the beam splitter and subsequently directed towards the detector. These two light beams can produce constructive interference due to the low-coherence characteristic of the light, ensuring that they have travelled equal distances [103]. There are two types of OCT, Time-domain (TD-OCT) and Fourier-domain (FD-OCT), in which in this research FD-OCT is used. In Fourier-Domain Optical Coherence Tomography (FD-OCT), the reference mirror remains stationary, and a spectral detector is utilised, as illustrated in figure 2.6 (a). To determine depth information, the spectrum of the reflected signals is analysed through Fourier analysis, giving rise to the term Fourier-domain OCT [101, 104, 105]. FD-OCT, with its fixed reference mirror, offers faster imaging capabilities and is the predominant OCT method [105], which is also the type employed in this thesis

In OCT imaging samples are depth profiles are scanned point by point along a scan line, then patched together in order to generate a two dimensional cross-sectional image of the sample as given in figure 2.6 (b). In this project an ultra-high-resolution FD-OCT (centre wavelength of 810 nm and a depth resolution of 1.8 μm in air) [104], developed by the Imaging & Sensing for Archaeology, Art History & Conservation (ISAAC) group at Nottingham Trent University was used to measure the thickness of the PDMS films. From an OCT image, the optical thickness of the sample can be determined, which is the product of the real thickness and the group refractive

index. The group refractive index n of a material is defined as the ratio of the vacuum velocity of light to the group velocity in the medium. Therefore, to measure the real thickness of the PDMS films, the optical thickness of the PDMS film was divided by n of the PDMS, which was measured to be n = 1.42 [102, 106].

Chapter 3

Imaging of wrinkling patterns

3.1 Introduction

A detailed explanation of wrinkles and their formation, and the main questions which are given through this work were discussed in Chapter 1. The key features to be measured for the analysis of the wrinkles are their amplitude and their wavelength and how these metrics vary with position and film curvature. This chapter discusses the imaging technique employed for the analysis of the wrinkles formed on the curved thin films described in Chapter 2. It includes the experimental setup that was designed, the theoretical components of the imaging used, and the relevant algorithms developed to map the surface height profile of a floating film and to characterise the wrinkles. As mentioned in Chapter 1, there are different theoretical predictions and models for wrinkling on curved films [63, 107, 108]. But, a significant challenge to this subject is the imaging and analysis of these patterns, formed in an experimental environment. Therefore, in this chapter, the aim is to explain the developed imaging technique and the processing algorithm which was used in this research study.

There are several studies in the literature concerning the analysis of wrinkling patterns [50, 108–114]. An important example is focused on the patterns formed on the bi-layer planar systems where a polymer is coated either on a glass substrate or on another polymer substrate [115–117]. These studies include the application of a temperature gradient [118, 119]or a mechanical force [58, 120, 121], to two layers having different inherent mechanical properties. The removal of these forces triggers the formation of wrinkling patterns. This occurs when the developed stresses that are different in the two layers try to accommodate each other, leading to out-of-plane deformations. These studies typically use optical microscopy techniques to study the patterns, since the wrinkles are mainly in the nanometre to the micrometre range.

Similarly, there are studies which use the atomic force microscopy (AFM) to measure wrinkle characteristics formed on hydrogel films. For example, Glatz et al. [122] used AFM profilometry to analyse wrinkling patterns formed when soft PDMS was cast into a mould consisting of hard PDMS.

A common element in the imaging technique employed by these examples in literature is the

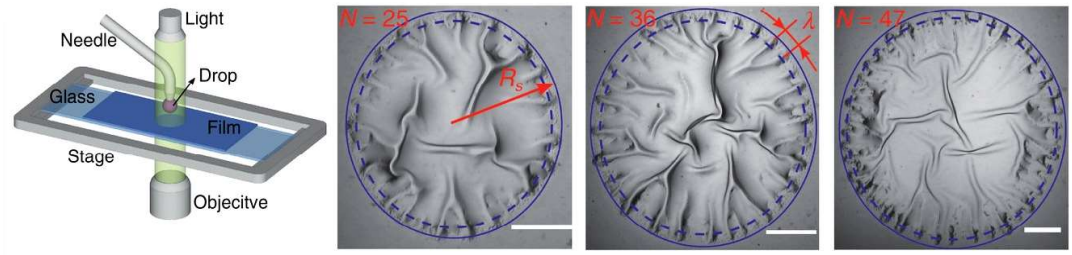

Figure 3.1: Figure showing the wrinkles observed on a thin film made of polymer PEDOT: poly(4-styrene trifluoromethyl (bissulfonylimide)) by using inverted microscopy adapted from [12].

stationary substrate which allows for easy setup for imaging methods. On the contrary, imaging methods become complicated with floating or suspended samples in liquid media or substrate.

Paulsen et al. [123] worked with wrinkling of a polystyrene film of thickness 113 nm, where the film was floating on water. It was poked from beneath by a rod with a spherical tip. This led to surface deformation and a constraint to the flotation of the thin film, which enabled easy observation using an overhead camera. However, they were only able to report the wrinkle wavelength observed from the shadowgraph pattern of dark and bright lines, caused by the lensing around wrinkles, rather than any absolute height or amplitude information. Alternatively, Albarran et al. [13] used polymer shells of different shapes, which were floated on water. In this case, the patterns formed were studied by projecting a vertical laser sheet across the shell [13]. Height profiles along one direction of the deformed shells were created by obtaining calibrated side-view digital photographs of the scattered laser light. Also, Albarran et al. used the shadowgraph technique for imaging the wrinkles with the help of a collimated light source, which was projected through the shell onto a translucent sheet.

However, these studies present certain limitations in the existing literature, as they require additional setup and specialised equipment for imaging technologies. Furthermore, they are constrained in terms of the type and quantity of wrinkle data they can capture. Shadowgraphs, for instance, can only provide brightness data due to lensing effects, while laser sheet imaging is limited to height profile data pertaining to specific cross-sections or the mid-line of floating strips. Consequently, these methodologies fall short in reliably determining wrinkle characteristics since a substantial amount of essential data remains unaccounted for.

To address this challenge, an effective methodology should offer three-dimensional data encompassing the entire height profile of the entire film sample, all while maintaining a non-invasive approach. This is especially crucial when dealing with delicate handling requirements inherent to thin films. The imaging method outlined here fulfils this imperative need for studying wrinkling

patterns on floating films and provides reliable 3-dimensional data without any need for special scientific equipment.

3.2 Experimental setup

For capturing the wrinkling pattern formed on the curved films, and as an early prototype trial, a gelatin solution was prepared and was cast on a 70mm x 70mm saddle-shaped mould. The gelatin solution was prepared by dissolving 20 g of Gelatin Fluka No. 48723 (CAS Nº:9000-70-8) powder into 100ml of distilled water and stirring constantly for 30 minutes at 60° C. After 2-3 hours, once the film was dried it was peeled off from the mould and dispersed in a water bath, as described in Chapter 2. Although the wrinkles formed on the film could be seen by the naked eye, the challenge remained to capture a full surface profile of the wrinkled configuration for

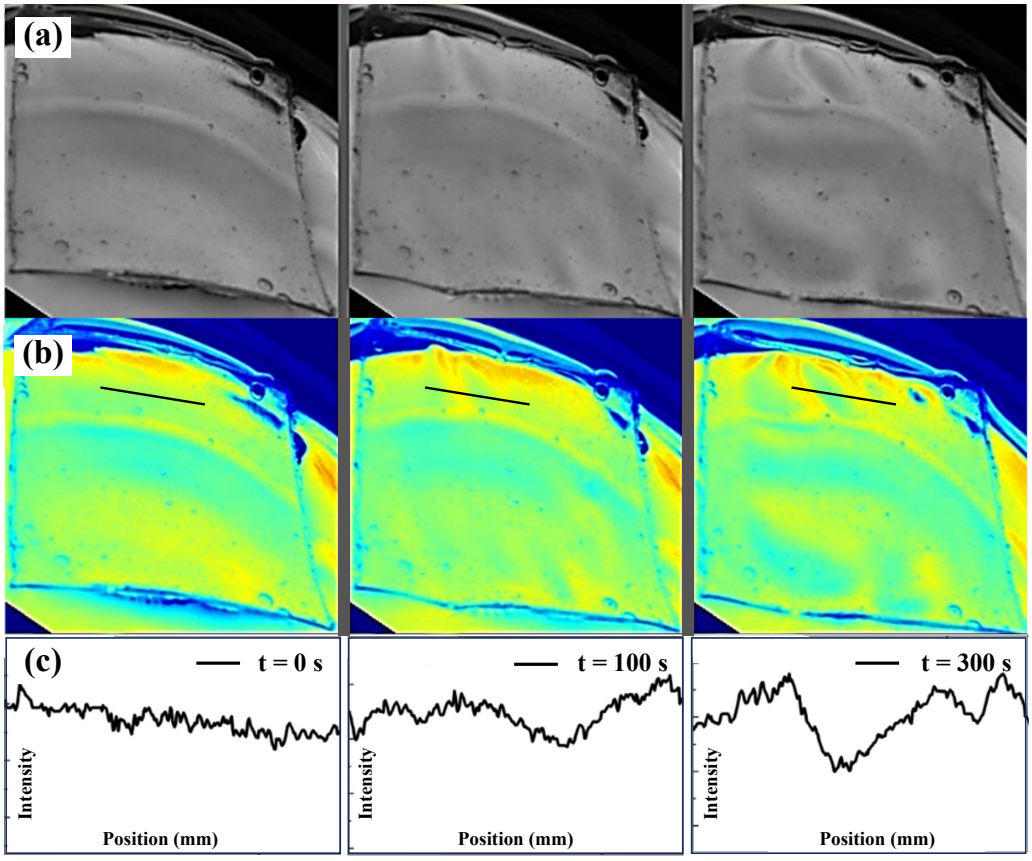

Figure 3.2: Wrinkling analysis of gelatin film using ImageJ. (a) shows time sequence images of wrinkles forming over a gelatin film approximately 100 μm thick. (b) Pseudo-colour images of the corresponding images and black like showing a section on the gelatin film (c) intensity plot of the corresponding section (marked in (b)).

further analysis, i.e., determining the wrinkle features. As an initial attempt the images of the wrinkled film on the water bath were captured at an angle, using a DSLR camera. The images were analysed using ImageJ software [124] to extract the intensities of pixels along a line profile of the image, as shown in Figure 3.2. Variation in the intensity profile of the film cross-section can be observed over a span of 200 sec and the wrinkle can also be visually confirmed from the pseudo colour plot. These initial experiments allowed for the exploration of gelatin-based thin film fabrication and identified potential limitations in the methodology.

Gelatin films had limitations, such as capturing air bubbles during preparation. Also, the thickness of the film cannot be easily controlled, due to the low viscosity of the gelatin solution before setting. The fabricated films, after a single cast of gelatin, were very delicate and brittle. To attain a desirable thickness coating multiple gelatin layers was a potential solution but due to the low melting point of gelatin [125], no supplementary layers could be coated. Since, the process of dissolving gelatin powder in water requires the input of heat, making it an endothermic process, the heat from the second batch of gelatin solution was sufficient for liquefying [125, 126] of the previously cured layer. As a result, layering is not feasible in this situation. The gelatin thin films were elastic in nature when dispersed in water. However, the peeling of the films from the mould was a critical step, which unfortunately resulted in frequent tearing of the film. As a result, polydimethylsiloxane (PDMS) was later used as a more suitable alternative to develop as discussed in section 2.2. In either case, the challenge of imaging and characterising the wrinkling pattern still remained. Analysis of images of wrinkled gelatin films taken at an angle did not prove to be a robust methodology for determining the wavelength and amplitude due to several factors. Firstly, the difficulty of standardisation for example in lighting and positioning in taking and analysing the images can lead to widely varying results. Secondly, the interpretation of the images is subjective, which can introduce inconsistencies and lack of reliability. Finally, the results obtained may not be reproducible due to the inherent variability of the gelatin film and experimental conditions.

In the effort to develop a suitable technique for imaging of wrinkles, a novel optics-based method was explored. Different dot grid patterns were printed and placed below the water bath (which was in a transparent Petri dish). This led to an observation of a unique distortion pattern of the dots, as seen from above. The dots are magnified and diverged near the crest, and converged near the troughs of a wrinkle, due to refraction. Some images taken with different dot patterns are shown in Figure 3.3. Experiments with dot patterns with different dot sizes, spacing colour, etc., were undertaken so that the wrinkling pattern could be captured in a better manner, compared to previous methods.

The experiment was conducted over multiple iterations. A triangular dot grid pattern with a

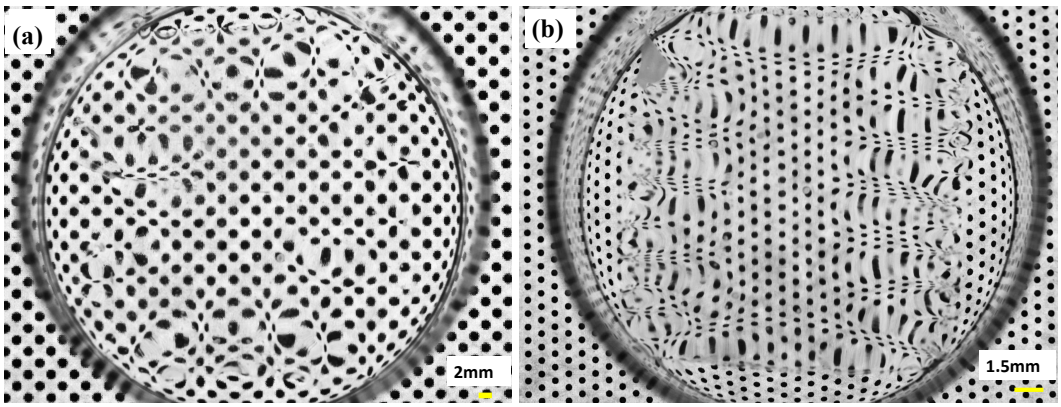

Figure 3.3: Images of different dot patterns, seen through a wrinkled film floating on a water bath. From the images, it is evident that dots are magnified near the crest, and that the positions of the dots near the troughs are converged.

dot diameter and grid spacing (white space between the dots) of 2.5 mm as shown in Figure 3.3 (a) was used for the first trial. However, some wrinkles were smaller than the dot size, making them difficult to observe. In response, the dot size and spacing were reduced to 1.5 mm in the second iteration, as shown in Figure 3.3 (b).

Using the 1.5mm dot pattern, an experimental setup for imaging the wrinkling pattern was established. The printed dot pattern was sandwiched between an LED white light panel on the bottom and an acrylic Petri dish on the top. This helped in illuminating the dot pattern from the bottom of the Petri dish. The transparent acrylic rectangular Petri dish was filled with deionised water up to a depth of 5mm, as shown in Fig. 3.4. The experimental setup also included a Nikon DSLR Camera (D5100) which was fixed at a height of 42 cm on a retort stand above the Petri dish, with the help of Thor-labs optical stainless steel posts.

With this experimental setup, digital images of the dot pattern before and after floating the PDMS film were captured carefully without disturbing the dot pattern, Petri-dish, camera etc. The images with the PDMS film show magnified and converged dot patterns due to the formation of wrinkles. Using MATLAB, both the initial and distorted images of the dot pattern were processed by thresholding followed by identifying the connected regions and their respective centroids. With the help of the centroid coordinates, the displacement vectors of the centroids were calculated. Tracking the dot centroids and evaluating their displacement vectors was useful for the development of a discreet vector field specific to a wrinkled film which was further used for computing a continuous displacement field for further analysis and determining the height profiles. Processed images of the initial and distorted dot patterns, with the dot centroids, are

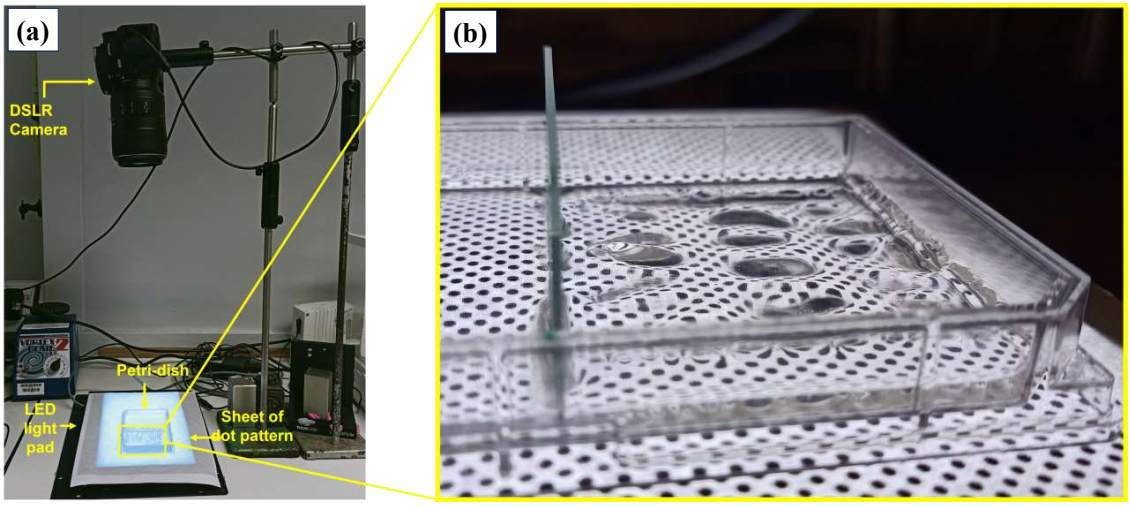

Figure 3.4: Images of the experimental setup. (a) Image showing the experimental setup with the sheet of dot pattern sandwiched between the LED light pad and the water bath in the Petri dish and a DSLR camera mounted vertically above for imaging (b) a close-up view of the Petri dish, with a wrinkled film in it.

given in Figure 3.5. The MATLAB algorithm used for this method is explained in more detail in Section 3.3.2.

Finally, modifications were made to the experimental set-up to improve the quality and reliability of the method, which was then to be consistently used for capturing the wrinkling pattern. To eliminate the possible movement of the dot patterns while dispersing the PDMS film onto the water bath during the experiment, the printed sheet of dots and the underlying LED light pad were replaced with a fixed screen. This involved a tablet (Microsoft Surface Pro 7), which projected the dot pattern from beneath the water bath. This also enabled automation and provided for the possibility of changing the dot pattern without disturbing the floating thin film.

Although decreasing the dot diameter and grid spacing improves the resolution of the wrinkles, there is still a limitation to the achievable dot proximity. With an increase in resolution, another rising concern was the identification of the refracted dots and ensuring proper matching of the displaced dot pattern with the original one due to the close proximity. To address this issue, an option with a coloured dot pattern was explored for the third iteration, as shown in fig 3.3c. However, this increased the complexity of the analysis, owing to the increase in variables to be processed and matched, namely, hue and saturation in addition to the luminescence for reliable tracking or identification of the magnified and converged dot patterns and prompting

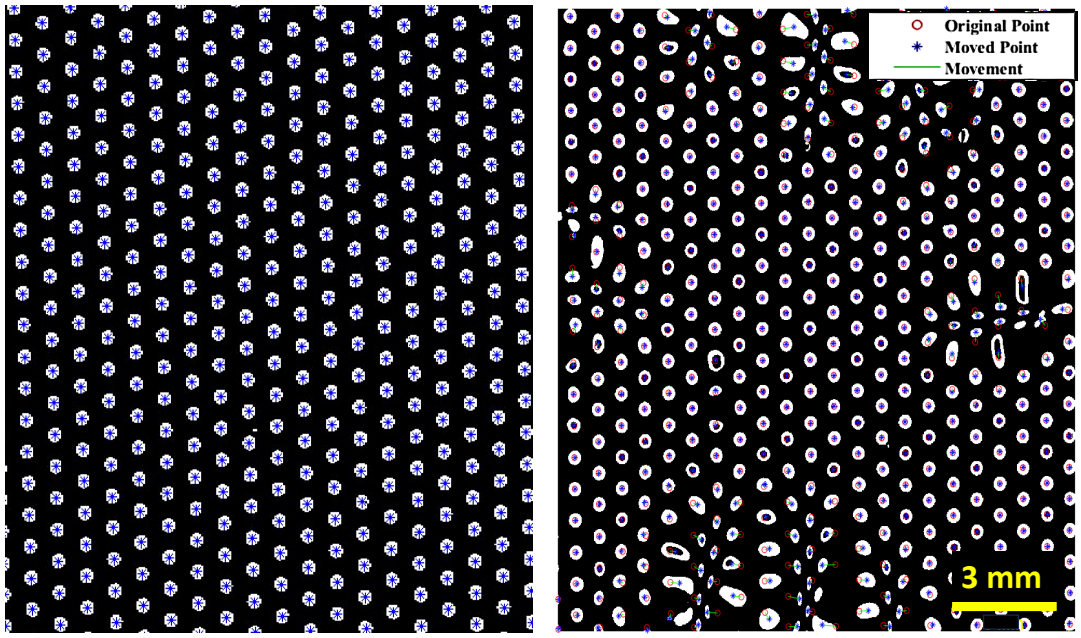

Figure 3.5: Figures showing the centroids of the dots in processed and threshold images, before and after the addition of wrinkled film. The dots are magnified and diverged at the crests and the dots were converged at the troughs of the wrinkles.

the development of a novel random-dot methodology to avoid resolution problems and create a simple analysis approach, as will be discussed later in this section.

Using MATLAB, random close-packing dot patterns were generated by iteratively placing dots in a two-dimensional space while ensuring a minimum separation distance [127, 128]. A minimum separation distance was defined as variable χ. In each iteration, a potential dot location was generated with random x and y coordinates. The code then calculates the distances between this new generated dot and all previously generated dots. If the minimum distance between the new dot and the existing ones exceeded the specified χ value (separation distance $\chi = 0.015$), the dot was added to the arrangement. This iterative process was continued for a 10000 iterations to generate each of the 30 different dot patterns, resulting in a collection of $\sim$ 3000 dots, in an area of 600 cm^2 (dot density of 5 dots/cm^2), which were strategically spaced apart to maintain the minimum separation constraint but without any regular order. Finally, the code visually represented this close-packed arrangement, creating intricate and visually appealing dot patterns.

Capturing different dot patterns for the same wrinkle pattern improved the quality of the displacement data. Instead of a single dot pattern, a batch of 30 random dot (with a dot density of 5 dots/cm^2) patterns was generated using MATLAB, which were projected consecutively onto

the tablet screen. Both the initial (without the thin film) and the final (with the thin film) images of the dots were captured, which resulted in 30 pairs of data sets. These images were processed in the same way, explained in section 3.3.2, and their displacements were combined and visualised together. The discrete data set of displacements was then interpolated to get a continuous plot of displacement data, using methods that will be developed and explained in 3.3.2.

3.3 Determining the wrinkle parameters

This section explores the approach adopted for calculating the wrinkle characteristics, like the amplitude and the wavelength, using a theoretical framework derived from optics.

3.3.1 Optical theory

The experimental setup used in this work can be considered and related to an optical inverse problem. Consider a water bath initially of constant height h_0, onto which a wrinkled film is floated. Beneath the water bath, there are dots that are positioned randomly. Let the distance from any point on the surface of the wrinkled film to the bottom of the Petri dish be $h(x)$, as given in Figure 3.6. A ray of the light incident on the film surface making an angle of incidence φ_i with the normal at the point of incidence changes its direction of propagation and the refracted ray makes an angle of refraction φ_r with the same normal. The change in direction can be denoted by the angle $\theta = \varphi_i - \varphi_r$. The line perpendicular to the incident ray at the point of incidence also subtends an angle of φ_i with the tangent at the point of incidence due to the property of similar triangles.

From Figure. 3.6,

$$\tan\ \varphi_i = \frac{\mathrm{d}h}{\mathrm{d}x}, \tag{3.1}$$

$$\tan\ \theta = \frac{\delta}{h(x)}, \tag{3.2}$$

where $\theta = \varphi_i - \varphi_r$ and δ is the lateral displacement in the apparent position of the dot. From Snell's law and considering the experimental setup, $n_1 \sin\varphi_i = n_2 \sin\varphi_r$. In this case, n_1 is the refractive index of air, which is 1, and $n_2 = n$ is the refractive index of water, which is taken to be 1.33. Therefore,

$$\varphi_r = \sin^{-1}\left(\frac{\sin\varphi_i}{n}\right). \tag{3.3}$$

Now, from Figure 3.6 and from Equation 3.2, $h(x)$ can be written as:

$$h(x) = \frac{\delta}{\tan\theta} = \frac{\delta}{\tan(\varphi_i - \varphi_r)}, \tag{3.4}$$

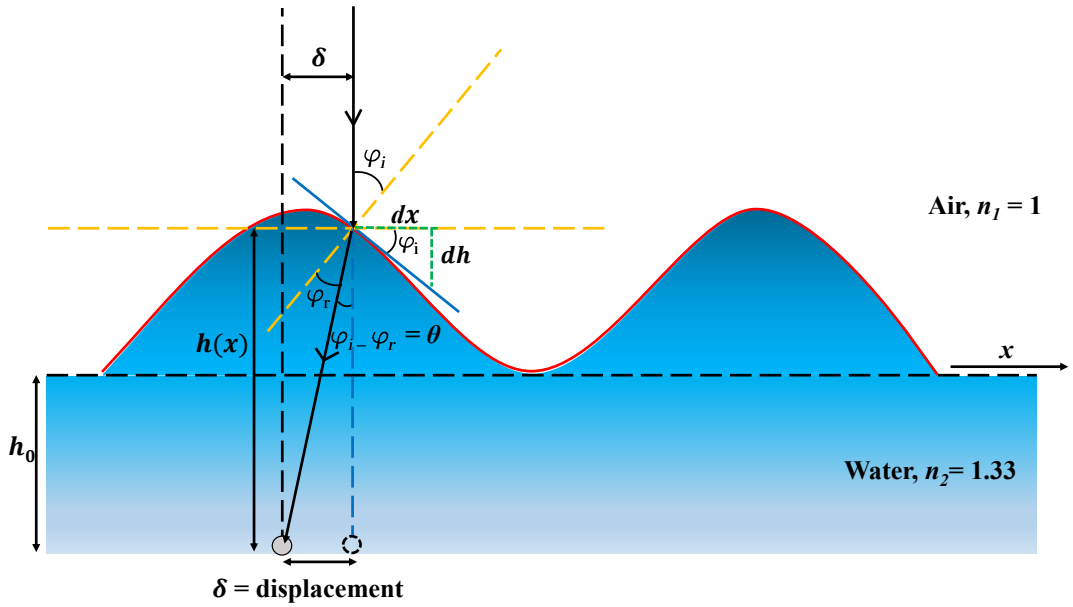

Figure 3.6: Ray trace diagram showing how light rays are refracted through the water layer with an uneven upper surface and how the apparent position of a dot is displaced, as its image passes through a wrinkled surface.

and now by substituting for φ_r in equation 3.4, we get,

$$h(x) = \frac{\delta}{\tan\left(\varphi_i - \sin^{-1}\left(\frac{\sin\varphi_i}{n}\right)\right)}. \tag{3.5}$$

By considering the small angle approximation, $\sin\varphi_i \approx \varphi_i$, and $\tan\varphi_i \approx \varphi_i$, Snell's law can be re-written as $\varphi_i \approx n\varphi_r$. This gives,

$$h(x) = \frac{\delta}{\varphi_i - \frac{\varphi_i}{n}} = \frac{n\delta}{\varphi_i(n-1)}. \tag{3.6}$$

The values of h/δ from Equation 3.5 and 3.6 were compared and plotted against a range of φ_i, values as shown in Figure 3.7 (a). It can be noted that the two curves shown by a green line (without the small angle approximation) and a black dashed line (with the small angle approximation applied) overlap for a wide range of angles. The relative error of h/δ was also plotted as shown in Figure 3.7 (b). Assuming a $\pm 1\%$ cutoff for relative error, it can be seen that the relative error remains below this value until $\varphi_i = 0.20$, which verifies the wide range of validity of the small angle approximation. For a threshold of $\pm 1\%$ the relative error remains particularly small beyond which the relative error increases following the power-law relationship ($\sim \varphi_i^2$). On rearranging Equation 3.6,

$$\varphi_i(x) = \frac{\delta}{h(x)}\ \frac{n}{n-1}. \tag{3.7}$$

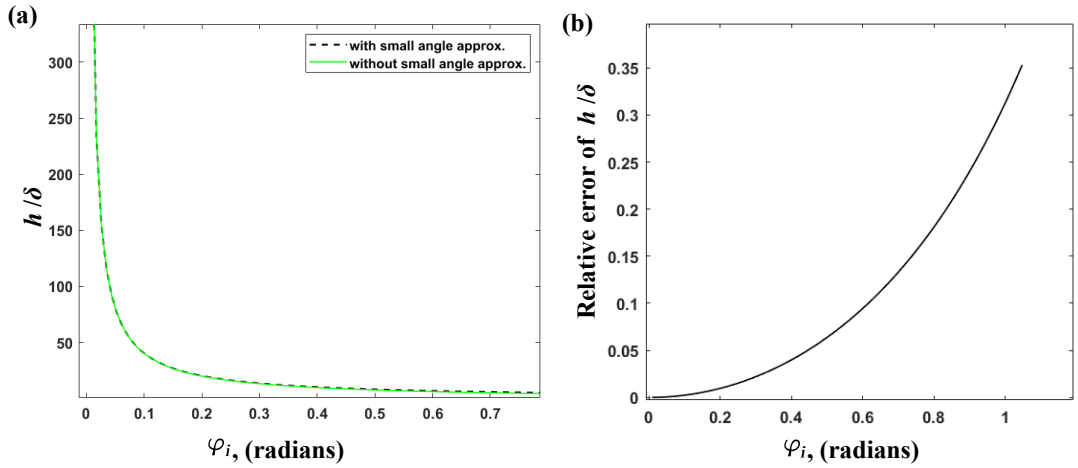

Figure 3.7: Verification of small angle approximation. The plots show (a) an overlap of the exact and small-angle approximations for h/δ and (b) the relative error in the approximation. From this, the approximation is seen to be better than 1% accurate for $\varphi_i \leq 0.20$, or 5% accurate for $\varphi_i \leq 0.44$.

Using the small angle approximation in Equation 3.1, $\frac{\mathrm{d}h}{\mathrm{d}x} = \tan\ \varphi_i \approx \varphi_i$. Substituting this into Equation 3.7 and rearranging,

$$\delta = \frac{n-1}{n}\ h(x)\ \frac{\mathrm{d}h}{\mathrm{d}x} = \ \frac{1}{2}\ \frac{n-1}{n}\ \frac{\mathrm{d}}{\mathrm{d}x}(h^2). \tag{3.8}$$

Since the derivation above follows identically in any direction, it can be generalised into a two-dimensional surface where δ_x and δ_y denote the lateral displacement in the x and y directions respectively. This gives a vector form of:

$$\vec{\delta} = \frac{n-1}{n}\ \frac{1}{2}\nabla(h^2), \tag{3.9}$$

where $\vec{\delta} = \begin{pmatrix}\delta_x & \delta_y\end{pmatrix}$. By taking divergence on both sides of equation 3.9,

$$\nabla \cdot \vec{\delta} = \frac{n-1}{n}\ \frac{1}{2}\nabla \cdot \nabla(h^2) = \nabla^2\left(\frac{n-1}{2n}\ h^2\right) \tag{3.10}$$

or more simply,

$$\nabla \cdot \vec{\delta} = \nabla^2\eta, \tag{3.11}$$

where $\eta = \frac{n-1}{2n}\ h^2$. From the experiments, the displacement data $\vec{\delta}$ is acquired at a collection of points corresponding to the positions of the projected dots. The height of the water level, h_0, can be measured, and the refractive index of water is also known. The only remaining unknown factor is the height profile of the film which is a continuous scalar field across the cross-sectional shape of the floating film. Using MATLAB, the Poisson equation given in Equation 3.11 was

solved numerically and wrinkle patterns were determined. A detailed description of how the images were processed and analysed is given in section 3.3.2. including the numerical scheme to invert and solve Equation 3.11.

3.3.2 Image processing

This section describes the various steps which were used for the image processing of the dot displacement patterns using MATLAB. Initial and final images of each dot pattern was captured before and after placing the PDMS film on the water bath, respectively. This was repeated for the whole batch of 30 random dot patterns, as described in section 3.2, resulting in 30 pairs of images, namely, with and without the wrinkled film. The analysis was performed in a loop, and the steps for one pair are explained below.

A pair of images (with and without the wrinkled film, and corresponding to the same dot pattern) was imported into MATLAB using `imread` and converted into grayscale using `rgb2gray`. Once an image is read into MATLAB, it is stored in terms of pixel intensities, in the form of matrices. The next step in the process was to select the region of interest from both images. This allowed the representation of the grayscale-cropped images in the form of a 2D matrix of pixel intensities. To maintain consistency within the whole batch of 30 pair of images, the image matrices were cropped to a specific aspect ratio which was determined manually. Examples of initial and cropped images are given in Figure 3.8 (a) and (b) respectively. It's worth noting that the selection of the region of interest was only performed once for each batch of images, rather than for every individual image within the batch. Moreover, the region of interest and the aspect ratio for both images in a pair were kept same to ensure consistency and accuracy for each comparison.

The function `im2bw` was utilised to transform the grayscale image into a binary image. The function required a level value as an input attribute, which is scaled to obtain a threshold value of pixel intensity between 0 and 255. This method was then used to convert all pixels in the input image with intensities greater than the threshold to the value 1 (white), while all other pixels were replaced with the value 0 (black). Therefore, a level value of 0.5 corresponds to an intensity value of 127, halfway between the minimum and maximum value of the pixel intensity range. The obtained image matrix was then inverted using the function `not`. Examples of the inverted, binary images are shown in Figure 3.8 (c).

The next phase was to find the centroids of the dots in the binary images. For this the function `regionprops` was used, which returns measurements for a set of properties for each 8-connected component (object) in the given binary image. The command `regionprops` provides

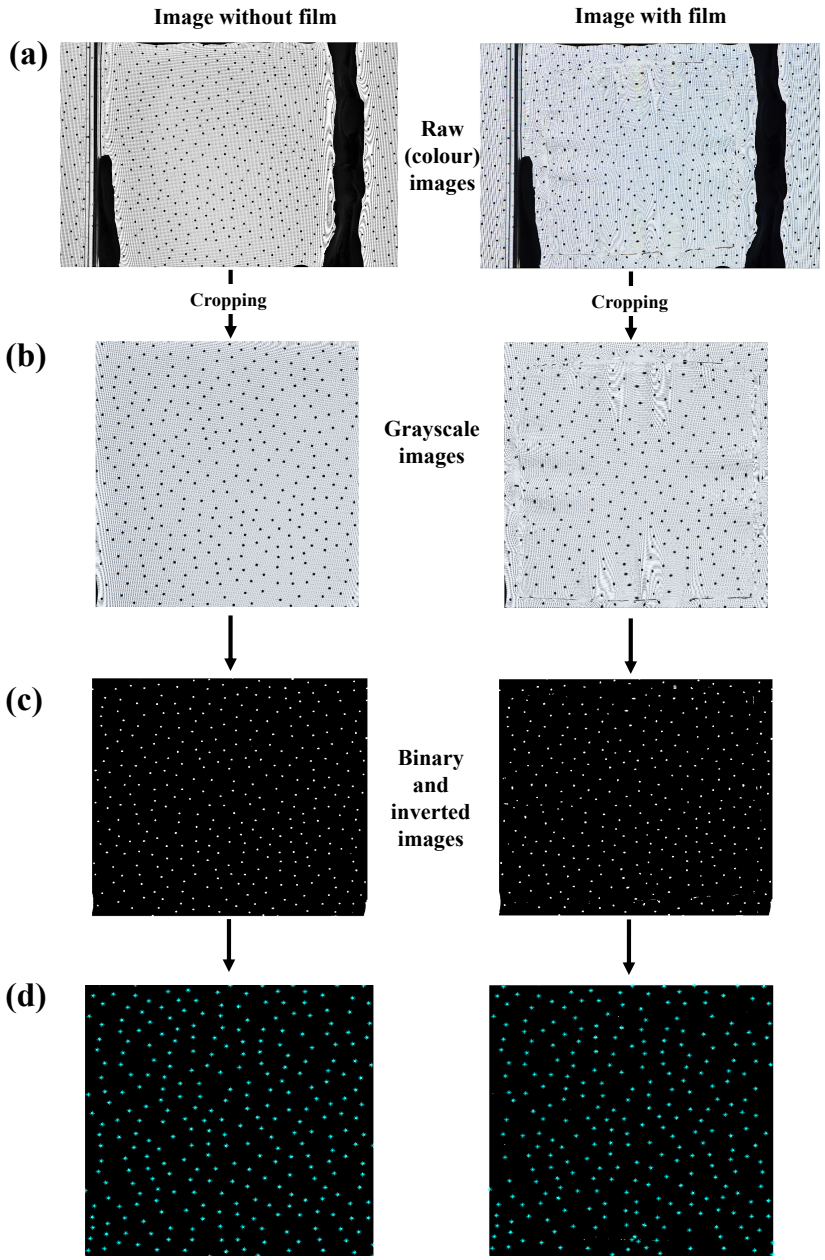

Figure 3.8: Different phases of image processing, showing (a) the coloured images of the dot patterns, (b) the cropped images of a dot pattern in grayscale, (c) the binary and inverted images of the cropped dot patterns and (d) the centroids (blue stars) of the dots of the corresponding pair of images with and without the film, respectively. Cropped images here cover 5×5 cm.

the ability to compute the region (cluster) properties from a binary image, for instance- area, centroid, major and minor axis length, orientation, perimeter etc. A table of object areas and the corresponding pixel coordinates of their centroids was extracted. Objects with areas less

than 50 pixels were deemed to represent noise in the data and were excluded. Figure 3.8 (d) shows the centroid locations of the image pair.

These image pairs of different random-dot patterns were then similarly processed individually and the obtained displacement values were combined into a single matrix for further analysis. The distance between each centroid in the initial image was calculated with respect to every centroid in the final image (image with the film). Any values greater than a given search radius were then eliminated, and a set of possible centroid pairings for every centroid was obtained. Of these, the pairings with the minimum distance were identified as the new positions of the displaced centroids. However, it is essential to acknowledge a potential limitation of this method, which is the possibility of incorrect matching of a few dot pairs, particularly in cases with noise or other sources of uncertainty. One powerful approach to mitigate this limitation and enhance the precision of dot location is the incorporation of multiple images. This strategy significantly reduces the error associated with dot localisation by allowing the dots to be more spread ou in any particular image, while still allowing the collection of large amounts of data. The key to the effectiveness of this approach lies in the diversity of the random dot patterns used and the analysis of data.

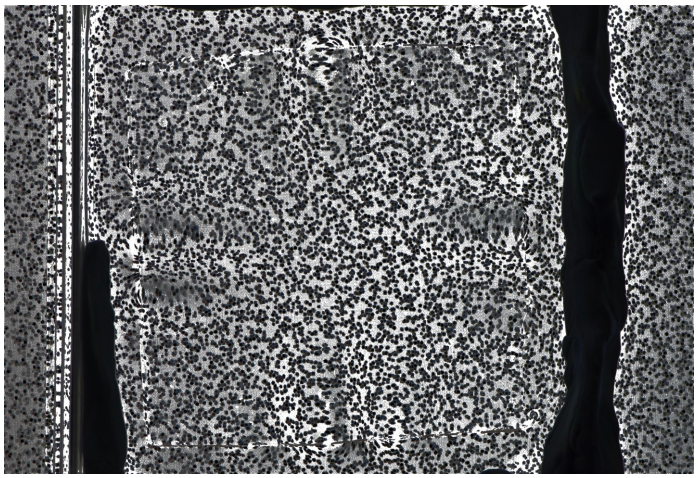

Figure 3.9: Stacked image of 30 different dot patterns showing the dot displacements.

The uncertainty in the final position of a centroid is made trivial by imaging multiple random dot pattern variations for both the initial stage (without the wrinkled thin film) and the final stage (refracted from the submerged thin film). Typically, every imaged film projection contained approximately 300 dots with a total of approximately 9000 dots pairs across the 30 different patterns being projected for scenarios with and without the wrinkled film. Figure 3.9 shows a stacked image of 30 random dot patterns with a wrinkled film on top of it. The closed packing of dots ensure a good resolution for resolving wrinkles of wavelengths as small as 1mm. This is

discussed in detail in the section 3.4. All the individual image pairs, featuring different random-dot patterns, were then individually processed. The benefit of this multi-image approach is that it takes advantage of the unique spatial distribution of dots in each pattern. Any errors or inaccuracies in dot localisation that may have arisen from a specific random dot pattern are likely to be different in another pattern and will eventually average out reducing the overall error. As a result, the combination of data obtained from multiple random dot patterns into a single matrix for further analysis not only improves precision but also enhances robustness.

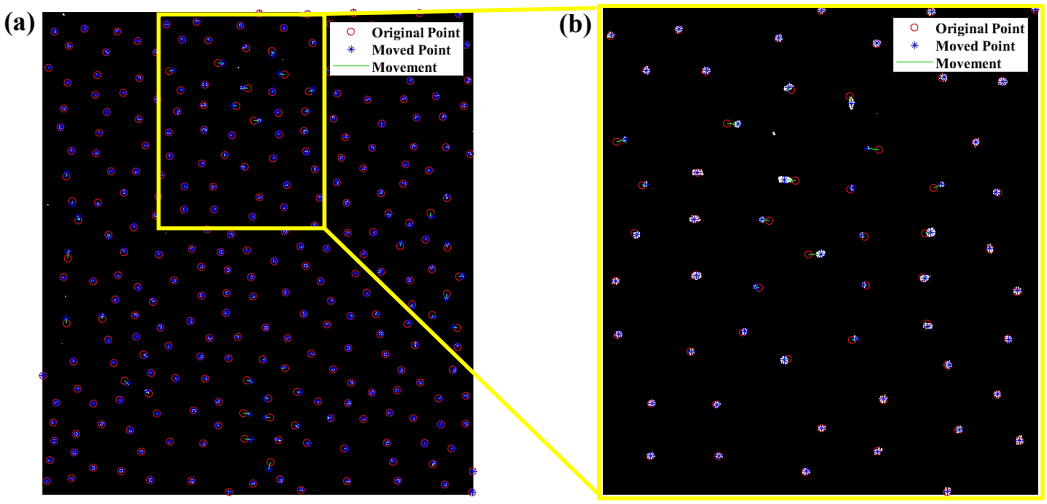

Figure 3.10: (a) Image showing the displacements of the centroids of the dots, as imaged through the floating film, as compared to their corresponding centroid positions in the initial image. Red circles show the original positions, blue asterisks shows the new position of the centroids and green lines show the displacement of the centroids. (b) is a magnified section of the image of (a).

As a next step, the function `scatteredInterpolant` was used to interpolate the scattered, discrete data points corresponding to the dot locations and displacement and generate a continuous function representing the displacement data $\vec{\delta}(\vec{x})$. Within MATLAB there are three options for this interpolation, namely, nearest, linear, or natural, depending on which type of continuity in interpolation is needed. In this work, the natural method was used since it interpolates the data points with a continuity of C^1. When it comes to interpolation methods, continuity is an important consideration because the interpolated surface or derivative of the displacement vector generated after interpolation is used in 3.11 to solve the Poisson equation. One way to achieve this is by ensuring that the interpolated function has at least C^1 continuity, which means that the interpolated function is not only continuous but also has a continuous first derivative indicating no abrupt changes in the slope of the function. The interpolation was done independently in both the x and y directions, and example plots for both x and y displacements are given in

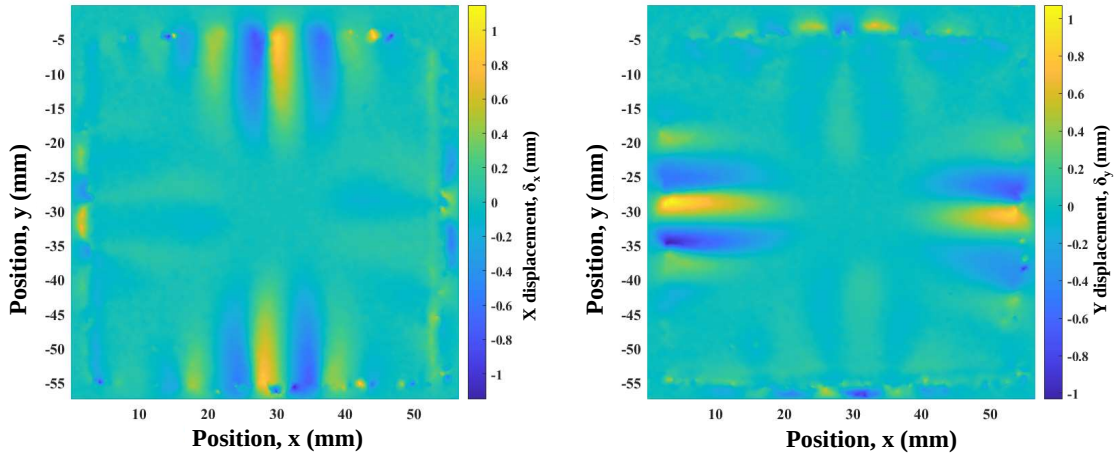

Figure 3.11: Components of the displacement vector $\vec{\delta} = \begin{pmatrix} \delta_x & \delta_y \end{pmatrix}$, in the x and y directions, interpolated from a series of centroids of the 30 pairs of images in the batch and their associated displacements.

Figure 3.12.

Once continuous data of displacement was generated, according to the theory explained in section 3.3.1, the next step was to solve the differential equation given in equation 3.14. MATLAB was used to this implicit equation numerically. For this, the function `solvepde` was used and the heights were generated. The function `solvepde` solves a partial differential equation of the form,

$$m\frac{\partial^2 u}{\partial t^2} + d\frac{\partial u}{\partial t} - \nabla(c\nabla u) + au = f \tag{3.12}$$

defined by a `PDEModel`. The `solvepde` function is used to solve the Poisson equation with specified boundary conditions and coefficients m, d, c and a. The function takes the PDE model as an input and returns the computed solution as a result. The `solvepde` function uses a finite element method to discretise the PDE model and solve it numerically. This method divides the computational domain into small subregions called elements and approximates the solution within each element using a set of basis functions. The basis functions are chosen to satisfy the boundary conditions of the PDE and are used to construct an approximation of the solution over the entire domain. Here, the resulting solution can be used to evaluate a vector of height values, $h(x, y)$ at the mesh nodes of the computed solution as discussed in detail below.

The PDEModel is a set of variables which contains the problem coefficients along with a geometry and the mesh. Several inputs are required to generate a `PDEModel`. Comparing Equa-

tion 3.11 with the PDE of the form defined in Equation 3.12, the following coefficients are obtained: $m = 0, d = 0, c = -1, a = 0, f = F$. Here, F is equivalent to $\nabla \cdot \vec{\delta}$. Therefore, a numerical divergence of the continuous interpolated displacement data, presented in 3.12 was calculated, using the function `divergence`.

In addition, a boundary condition is applied using the function `applyBoundaryCondition`. The input arguments for this function include the empty PDE `model` variable, the type of the region (`Edge` for a 2D geometry) bounded by the decomposed constructive solid 2-D geometry (function `decsg`, a Dirichlet condition defined as 'u' and a supplementary initial 'u_0' as $\eta = \frac{n-1}{2n}h^2$). This approach involves simplifying a complex geometry into simpler, regular subdomains and constructing the geometry of each subdomain using simple geometric primitive shapes, known as tria (triangular) or quad (square) elements.

Furthermore, a mesh is generated, using the defined triangular elements, for the model for the defined geometry and the mesh density is controlled by the value of '`Hmax`'. A value of 0.01 denotes the maximum edge length of the triangular elements in the mesh. Hmax is related to the mesh size, so it is always important to consider the geometry's complexity and the desired accuracy of the solution. Smaller values of Hmax result in finer meshes, which can lead to more accurate solutions but may require more computational resources. After a few iterations and comparing the solutions it generated after solving the PDE, a value of 0.01 was finalised. The PDE was then solved using the function `solvepde` and the solution of the PDE is plotted as shown in Figure 3.12.

The nodal solutions generated from `solvepde` are the values for η on the mesh vertices. The corresponding height values were found as $h(x) = \sqrt{\frac{2n}{n-1}\eta}$. These were then plotted and an example solution is shown in Figure 3.13 (a). For further analysis of wrinkling parameters, the surface was divided into 50 concentric quadrilateral from the edge of the film to its centre. For ease of analysis, each concentric quadrilateral was further segmented into separate edges. The edges were grouped into four separate quadrants, divided by the diagonal lines across the film, and the analysis of the wrinkles was done quadrant-wise.

In order to determine the wrinkling parameters, the minima and maxima of the height profile along each of the segmented edges were determined by using the functions `islocalmin` and `isloacalmax`. These functions detect the local minima and maxima in each segment in a quadrant and return it as an array of ones and zeroes depending on whether there were minima or maxima. As a filter to this, the prominence for finding the minima and maxima was set to 0.2. The prominence value of a local minimum (or maxima) measures how much the valley (or peak) stands out with respect to its depth/height and location relative to other valleys/peaks. The maxima and minima of each section in each quadrant were determined and plotted as shown in

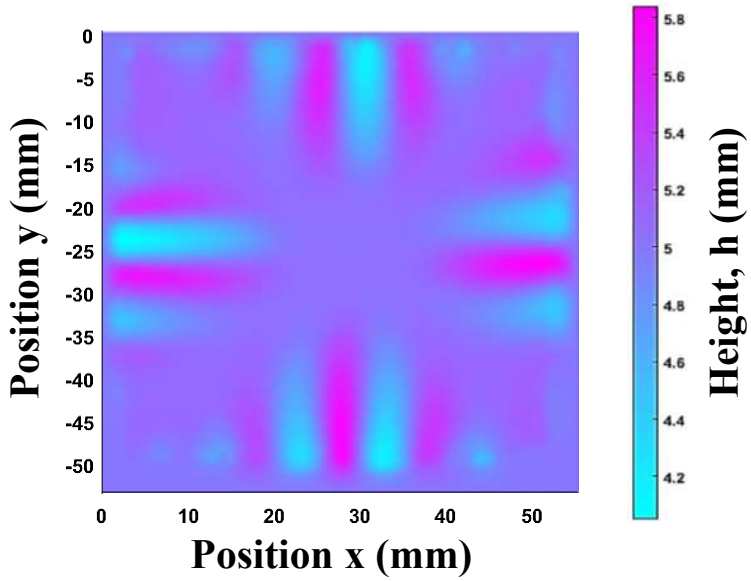

Figure 3.12: Figure showing the pdeplot, which is the solution of PDE which was solved using the function `solvepde`.

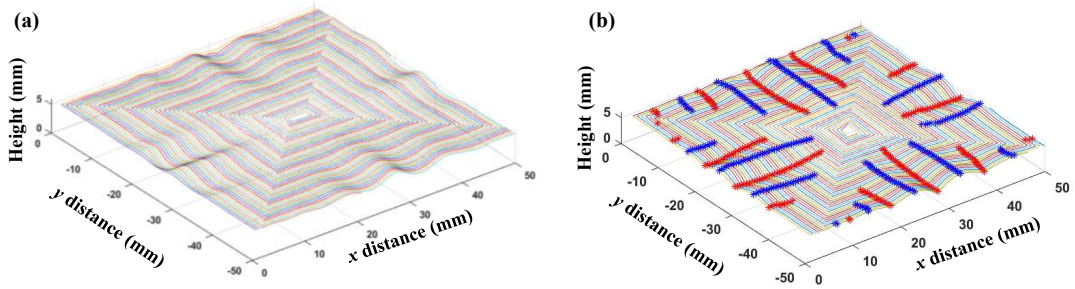

Figure 3.13: 3D plot of wrinkled surface. (a) showing the quadrilateral sections on a wrinkled surface and (b) depicts the maxima and minima points in each section of the concentric quadrilaterals. The prominence was set 0.2 in determining these extrema.

Figure 3.13 (b).

The wavelength of each segment was calculated by evaluating the distance between two consecutive crests (local minima) and troughs (local maxima) of the wrinkles which was then averaged to find one wavelength value for the segment. Next, the amplitude was calculated by averaging the height values of the obtained local maxima and local minima in every individual segment of every quadrant of the wrinkled film.

Although this approach seemed to produce reliable results, the method had an inherent limitation. Dividing the wrinkled surface into concentric quadrilaterals and analysing the formed quadrants inculcates a bias in the direction of observation of extreme points. This was also

observed from the fact that sections under observation do not necessarily always align with the

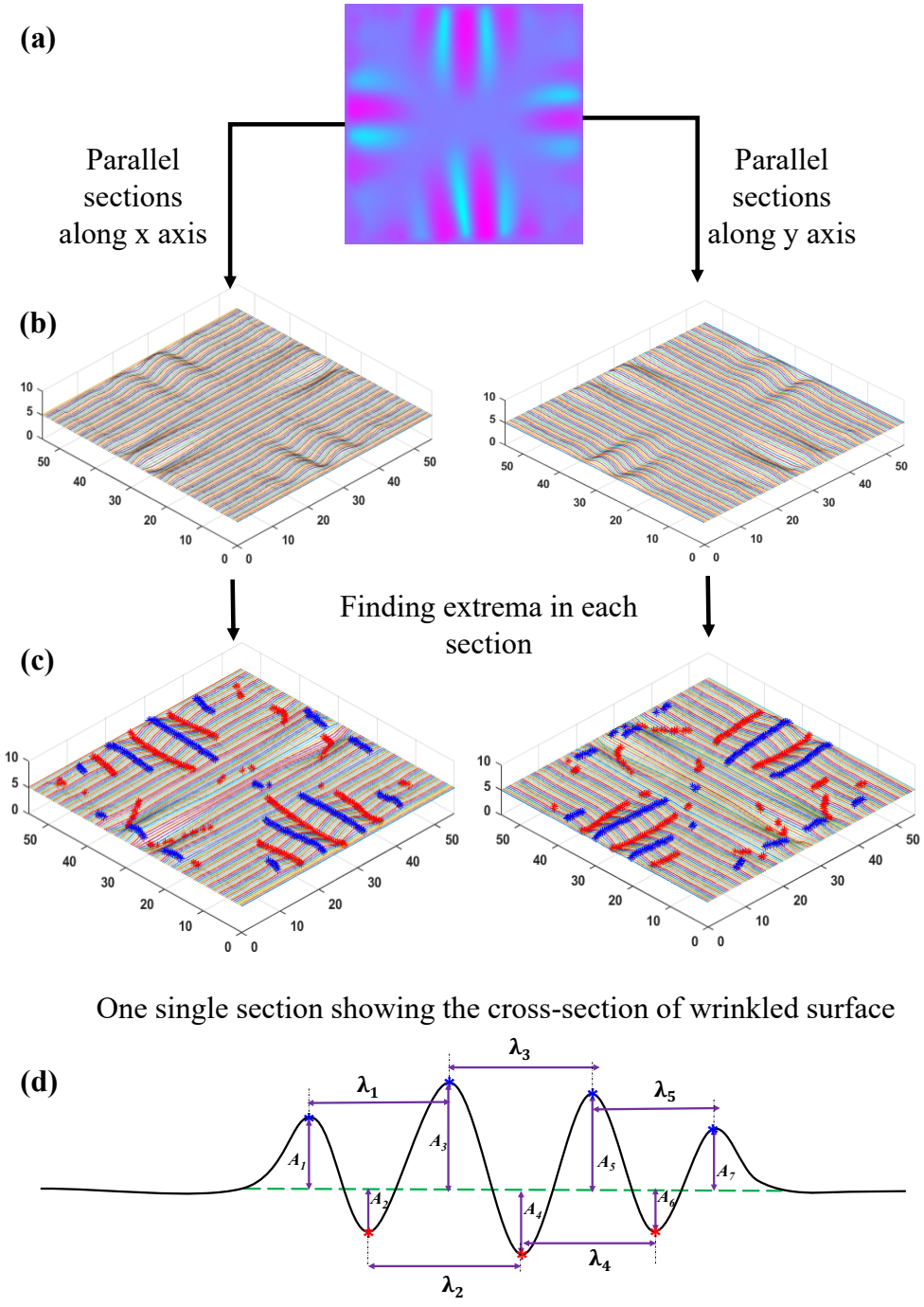

Figure 3.14: Illustration of different steps involved in determining the wrinkle characteristics. (a) plot of the solution of PDE, (b) shows the parallel sections in x and y directions, (c) depicts the maxima and minima in each parallel section in x and y directions and (d) schematic of a cross-section of a wrinkled surface.

direction perpendicular to the wrinkle direction and could lead to a disregard of potential data (extrema) resulting in incorrect outcome values. Another limitation of this method was the process of averaging individual observed values without any pre-processing or filtering which has detrimental effects on the obtained values of wavelength. This was due to the possibility of the presence of some far-spaced local minima (crests) or local maxima (troughs) on one or more segments of the film. The algorithm lacks the ability to distinguish these from consecutive extrema. This led to false observations of wavelength values and resulted in skewing of the obtained wavelength values.

In order to resolve this issue, instead of dividing the obtained 3D surface into quadrilateral sections, the wrinkled surface was divided into parallel sections both along the x and y direction of the film as shown in Figure 3.14 (b). A detailed illustration of the steps involved in determining the wrinkle characteristics is given in Figure 3.14. For determining the wrinkle characteristics, a new method was developed due to the limitations of the previous method as explained earlier. One of the biggest constraints was the calculation of wavelength. The functions `islocalmin` and `isloacalmax` were used for evaluating the local maxima and minima, respectively as shown in Figure 3.14 (c). The same step was repeated for the sections along the y-axis (3.14 (c)) with a prominence value of 0.2. Figure 3.14 (d) shows a cross-section of a wrinkled film with extrema which is marked as red and blue points.

For amplitude, a root-mean-square (RMS) value of the height or depth of all the individual local extrema points was determined and used as the representative amplitude value for the film. Evaluating the wavelength included adopting a method of Z-Scores, also known as standardisation in statistics and is commonly used to assess how far a data point is from the mean of a dataset in terms of standard deviations. It is a way to measure how "typical" or "atypical" a data point is within a given dataset, also known as an inlier or outlier in statistics, respectively. The Z-Score for every measurement is calculated by,

$$Z = |\frac{x - \bar{x}}{\sigma}|, \tag{3.13}$$

where Z represents the Z score, x is the individual measurement, $\bar{x}$ is the mean of the data and σ is the standard deviation of the data. A threshold Z value of 1 was chosen which meant that the data points were considered as outliers if they were more than one standard deviation away from the mean in either direction (above or below).

This was used to filter out any pseudo-wavelength measurements before finding the representative wavelength value for the film using the RMS method similar to the amplitudes. In summary, the method involving imaging of multiple random dot pairs, followed by centroid displacements, numerically inverting PDE to obtain height profiles and finally using parallel profile

sections to resolve the wrinkled surface into individual waves provided a robust technique to calculate the characteristic representative amplitude and wavelength value of each wrinkled thin film sample.

Since the final characteristic values depend greatly on the computed height profiles, it was crucial to validate the described methodology which is explained in the next section.

3.4 Validation of the image processing method

In section 3.3.2 a detailed discussion of the image processing methodology was provided. This included how the images were processed in order to determine the wavelength and the amplitude of the wrinkled film, and how these properties varied across the film. it is imperative to test the reliability of the methodology developed. To validate the method, the imaging technique explained in this chapter was performed on a transparent wrinkled sheet made of Polyethylene Terephthalate (PET). The difference between the PDMS film and this sheet was that the PET sheet was rigidly moulded into a fixed wrinkle pattern, whereas the PDMS film spontaneously wrinkles when dispersed in the water bath. The same set of 30 random dot patterns used for the PDMS films were projected using the tablet and the dot patterns were captured using the digital camera. The other image processing methods discussed in section 3.3.2 were then followed exactly. An image of the solution for the PDE for the PET sheet is shown in Figure 3.15.

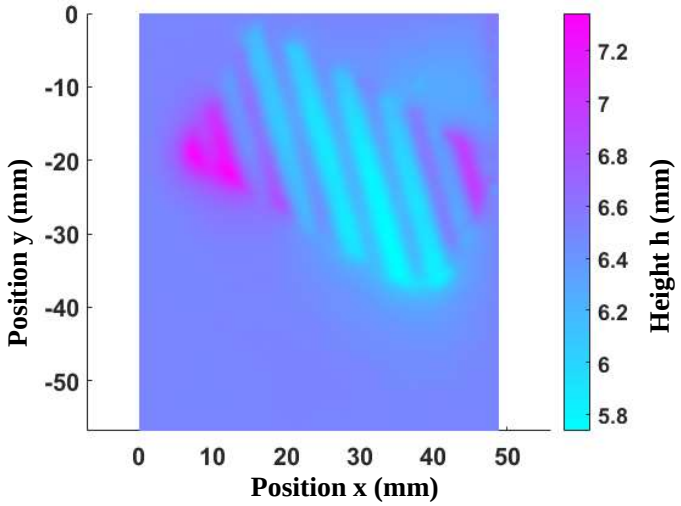

Figure 3.15: Plot of the solution of the PDE for the PET sheet using the imaging methodology explained in section 3.3.2. This is a validation of the developed image methodology.

To compare these parameters with an independent measurement of the heights and the wavelength of the PET sheet, an optical coherence tomography (OCT) technique was used as ex-

plained in section 2.3. The same PET sheet used for the analysis above was used for the OCT measurement. Figure 3.16 shows the OCT image of a section of the PET film from which the amplitude and the wavelength of the wrinkled PET sheet were determined. The OCT data was analysed using the ImageJ software. An amplitude value of 0.6 mm and a wavelength of 4 mm were determined from the developed imaging methodology and these values matched with the values from OCT imaging.

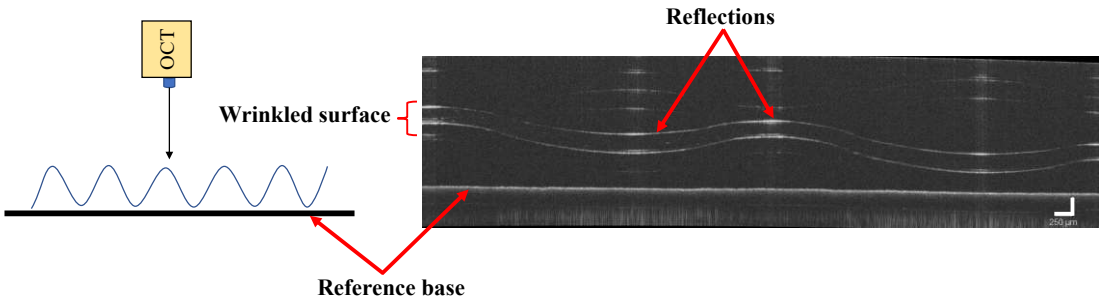

Figure 3.16: Illustration of measurement of amplitude and wavelength of a wrinkled Polyethylene Terephthalate (PET) sheet. (a) schematic showing position and direction of the PCT while measurement and (b) shows the resultant OCT image showing the reference base, reflected wrinkled surface.

Similarly, to validate the developed methodology for image processing and to evaluate how the number of points affects the accuracy of the calculated height (amplitude) values, another approach was implemented. A sinusoidally varying height profile was used to generate synthetic input data, which was then analysed so that the reconstructed surface could be compared with the known height profile values. A well-defined test function $h = h_0 + A\sin(kx)\sin(ky)$ was used to generate the desired sinusoidal surface on a regular grid of dimensions 2 units $\times$ 2 units and a grid spacing of 0.01 units. Here, $h_0 = 5mm$ represents the assumed water bath depth analogous to the experimental setup. Initially, the test function was defined for an amplitude value of $A = 0.002$ and the wavenumber, $k = 4\pi$ ($\lambda = 0.5$).

The derivative of the function was calculated using the command `gradient` in MATLAB. The gradient calculated was equal to the $\nabla \cdot h = \begin{pmatrix} \tan\varphi_{xi} \\ \tan\varphi_{yi} \end{pmatrix}$ which is the two dimensional form of Equation 3.1. By rearranging Equation 3.5 and solving the $\vec{\delta}$, the expected displacements were calculated using the equation $\vec{\delta} = h\tan\left(\vec{\varphi}_i - \sin^{-1}\left(\frac{\sin\vec{\varphi}_i}{n}\right)\right)$.

To visualise the effects of the number of points, projected by the tablet on the PDMS films, on the method of interpolation used in this research, it was required to analyse the methodology

for a number of points ranging from 10 to 40000. For the initial validation test, 500 random points were selected and the displacement corresponding to these points was calculated using the MATLAB algorithm. These are shown in Figure 3.17 (a) along with their displacement vectors in Figure 3.17 (b).

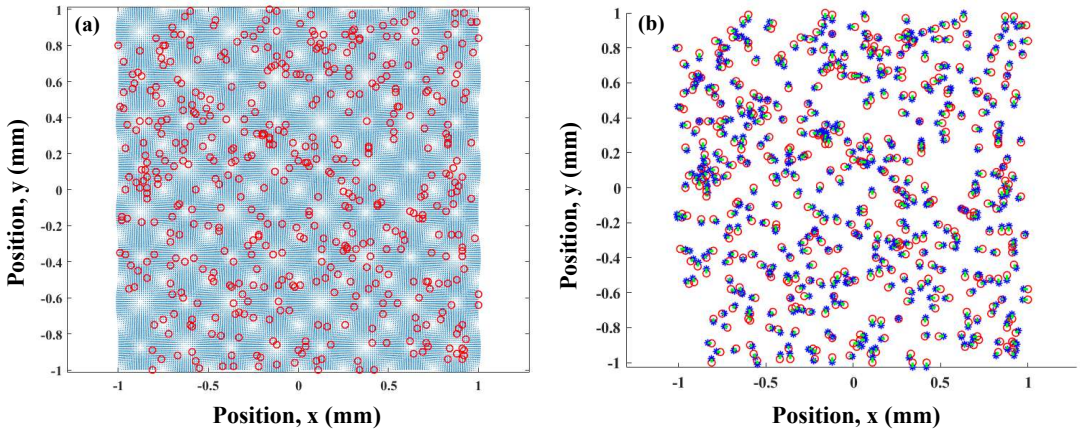

Figure 3.17: (a) 500 randomly selected points shown by red circles. (b) Calculated displacement vectors of the 500 points, where the blue points are the new positions and green lines are their movements.

Once the synthetic displacement vectors were calculated for the 500 random points, the same algorithm was employed for the further analysis of the experimental data by solving the partial differential equation. Furthermore, a 3-dimensional surface plot was reconstructed by numerically inverting the PDE. For 500 points the pdeplot, in Figure 3.18 (d)), showed a significant relative error in the height values when compared to the exact solution in Figure 3.18 (a)). Figure 3.18 (b), (c) and (e) also shows the surface plots (height profiles) obtained by numerically inverting the PDE for 10000, 1000 and 100 points, respectively. 100 points performed poorly with a relative error of 2.23×10^{-4} whereas, 10000 points provided an optimum relative error $< 5 \times 10^{-6}$. The relative error was computed by evaluating the absolute difference between the measured and calculated heights with respect to the measured height and is given by $(|h - h'/h|)$.

Figure 3.19 shows the plots of the computed inverted PDE solutions for random points varying from 10 to 40000. In order to determine the minimum number of points required to generate the sinusoidal function, the concept of Nyquist sampling frequency was applied. The Nyquist sampling condition is a fundamental principle in signal processing and digital communication. It states that the sampling rate, or sampling frequency, must be at least twice the maximum frequency present in the continuous signal being sampled. In the case of a sine wave, this

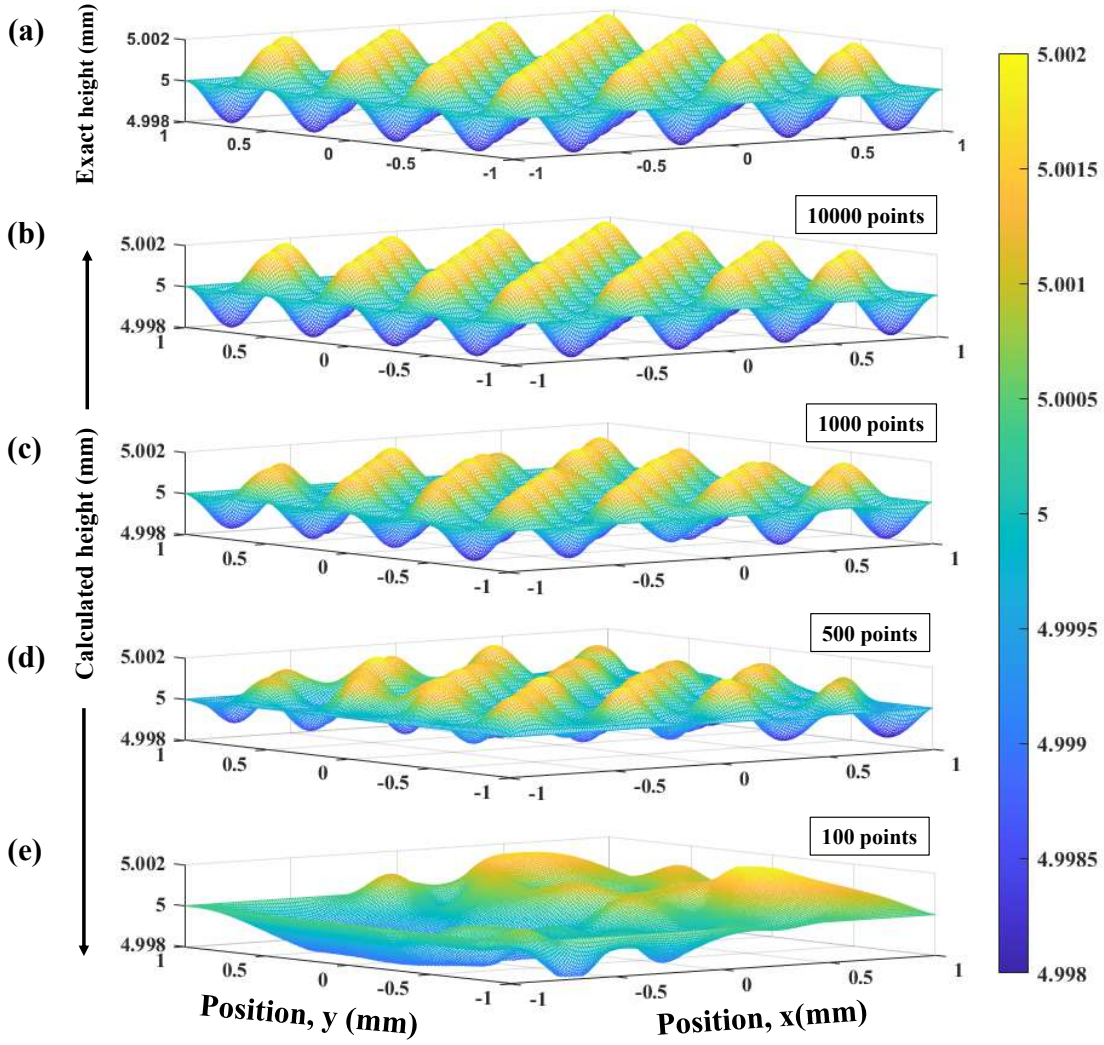

Figure 3.18: (a) 3D plot of the exact input function for a surface height and (b) the interpolation plot after solving the partial differential equation for heights.

means at least two samples are needed per wavelength of the sine wave to accurately represent it. Sampling with just one sample per wavelength would not provide enough information to faithfully reconstruct the original signal. Here, 'samples' are analogous to the 'random points in the experiment'.

According to the Nyquist theorem, a minimum sampling distance of $\lambda/2$ is required in each direction to approximate the solution to the sinusoidal function. If N is considered to be the number of random points to cover an area a, then a/N represents the area covered by each point. The average spacing of points in any direction can then be approximated by $\sqrt{a/N}$ which is also

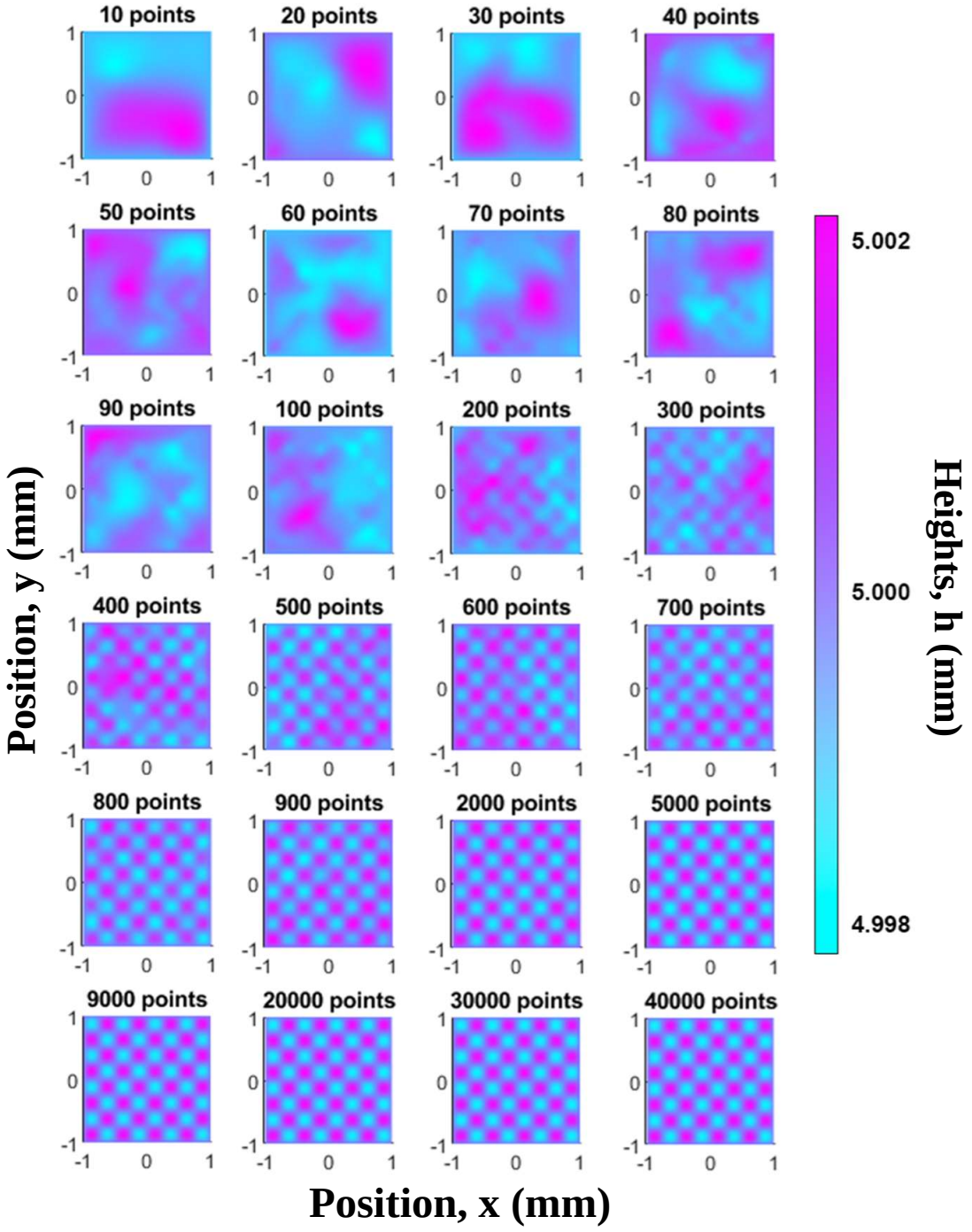

Figure 3.19: Figure showing different pdeplot plotted after solving the partial differential equation for height which was solved for varying number of random points.

then the effective sampling distance. At the Nyquist condition, then,

$$\sqrt{a/N} = \lambda/2. \tag{3.14}$$

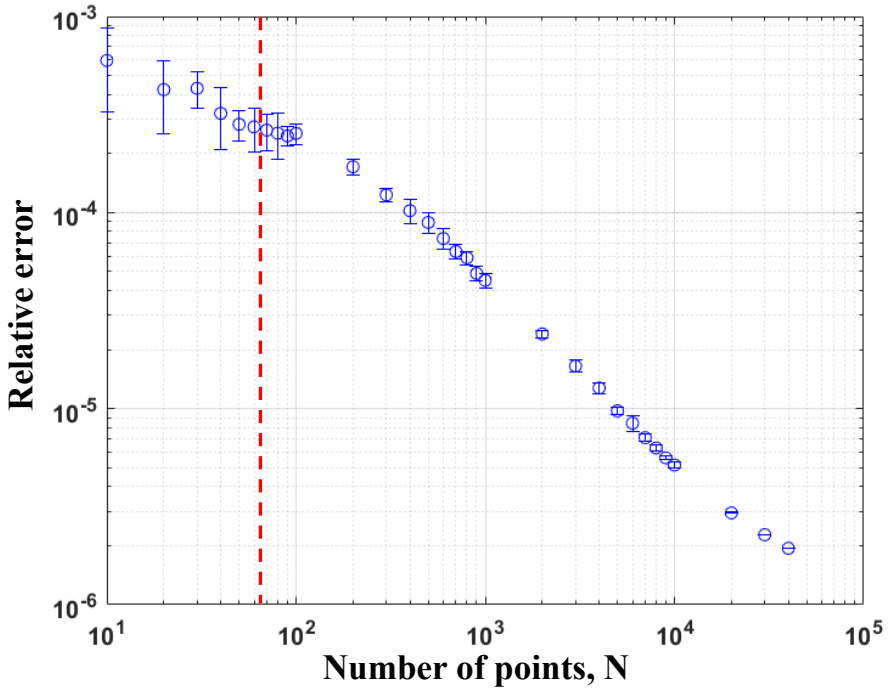

Figure 3.20: Convergence of height error values. The heights obtained from the image processing are compared with the heights of the exact function. The relative difference is plotted against the number of random points chosen for the interpolation, in order to get the displacement vectors. The red dashed line shows the Nyquist condition of $N = 64$ for $\lambda = 0.5$.

In the initial validation experiments, for $a = 4$ and $\lambda = 0.5$, $N = 64$ is the minimum number of points required. Although, as already observed from Figure 3.18 and 3.19, the number of random points $N = 10000$ (i.e., $N \gg 64$) points provided a superior result. Figure 3.20 explores this situation in more detail for $\lambda = 0.5$, and shows a decrease in the relative error with increasing number of points N. Convergence to the exact height values validates the interpolation and the developed numerical PDE inversion methodology.

The Nyquist frequency concept can also be extended to determine an effective resolution or the maximum wavenumber (minimum wavelength) that can be reliably sampled using the developed methodology. To evaluate a quantitative limit for the applicability of the methodology, Equation 3.14 can be rewritten as:

$$\frac{N\lambda^2}{a} = 4. \tag{3.15}$$

In other words, the expression $\frac{N\lambda^2}{a}$ represents the dot density and has a constraint that it must be greater than 4 to satisfy the Nyquist condition. This allows the computation of determining λ_{min} that can be reliably resolved for a defined number of random points N. This is illustrated

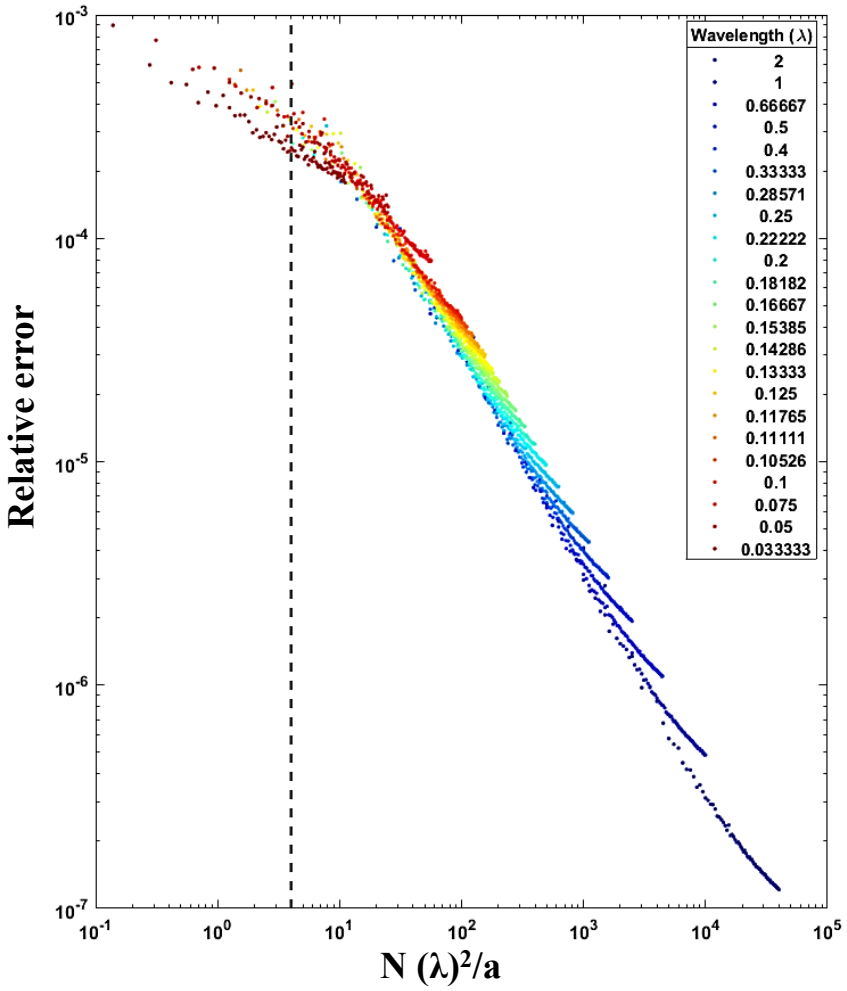

Figure 3.21: Convergence plot between the relative error of heights and the dot density, for a range of wavelengths varying from 0.022 to 2.0, showing the Nyquist condition ($\frac{N\lambda^2}{a} = 4$) marked with a dashed line.

in Figure 3.21. In the methodology employed for the experiments, $N = 10000$ was used and with the surface area of the film, $a = 2500$ mm^2, $\lambda_{min} = 1$ mm will be the minimum resolvable wavelength for the experiments. The method is computationally limited to a λ_{min} of 0.5 mm for the maximum of 40000 points. It should be noted that the maximum number of random points ($N = 40000$) was determined by the grid spacing defined in the MATLAB algorithm used for both the experimental and validation. Furthermore, extending the application of the developed image processing method beyond the specified limits of wavelength resolution would necessitate working with data of increased mesh densities, resulting in a significant increase in computational requirements.

3.5 Conclusions

In this chapter a simple and effective technique for imaging wrinkled films on a water bath was introduced. This method was used for determining the characteristics of wrinkled films, namely their amplitude and wavelength. The methodology described in this chapter was used to perform experiments and image thin film with both positive and negative curvatures. Different trials and modifications made to achieve this technique were also explained in this section.

This chapter also explained the developed imaging and processing methodology for the wrinkled thin films using the displacements of the random projected dots. The displacements of the dots were used to solve the partial differential equation which was derived using the optical theory and by using MATLAB the PDE was solved to determine the height profiles of a wrinkled surface. This was critical to evaluate the representative wrinkle characteristics, namely, the amplitude and wavelength. Two validation methods have also been included to verify the computed surface profiles with the known exact solutions. The limitations and constraints of the methodology were also determined. The developed methodology can be employed to analyse curved wrinkled films reliably with an accuracy of $< 1\%$(0.74%) error for surface slopes of $< 10°$. Also, the methodology was found to be capable of reliably resolving wrinkle wavelengths as small as $\lambda_{min} = 1$mm with $N = 10000$ random dots. The method is limited to a minimum $\lambda = 0.5$mm for $N = 40000$.

In chapter 4 the study focuses on elucidating the wrinkle characteristic results for various curvatures which were determined using the imaging methodology described in this chapter. The relations between the Gaussian curvatures and the variation of wrinkle characteristics have been discussed in detail. Several dimensionless groups have been determined and the effect of the specific thickness is also discussed.

Chapter 4

Effect of curvature on wrinkling patterns

4.1 Introduction

Mechanical instabilities seen on dried fruits, leaves, and flowers due to differential growth have been widely explored and studied over the past few years [129–136]. Also, the instabilities of thin films or sheets leading to surface patterns are extensively investigated because of their various applications, and similar patterns have been observed in biological systems during their growth [137, 138]. These surface patterns may arise due to a mismatch in the temperature, lengths, curvatures, stress, etc. of two adhering layers [16,46,47,53,110,114,119,139–141]. When the misfit stresses or strains generated by such processes stresses are above a particular point the system becomes unstable and, depending on the system, this instability results in phenomena like spontaneous wrinkling, folds, creases, herringbone patterns, labyrinth-like structures, etc. [20, 45, 142]. These sorts of patterns can happen either on flat or curved interfaces [143, 144]. Most of the experimental research on wrinkling patterns has been focused on planar or flat systems, some applications of which are highlighted in Chapter 1. Here, in this chapter, I will show the corresponding results for the case of thin shells with positive and negative curvature, using the imaging method given in Chapter 3.

When a thin film or a sheet has its own natural curvature, which is not equal to zero, the system must satisfy geometrical constraints which are somewhat equivalent to lateral confinement. Albarran et al. [13] have explained the resulting wrinkling patterns observed in shells of different shapes, sizes and thicknesses cut out from hemispheres. The shells used in their work had an effective lateral confinement arising from their own geometrical frustrations, and therefore did not require any external forces in order to bend and wrinkle. Instead, when these shells were floated on a liquid surface, a variety of patterns appeared, all showing wrinkles of constant wavelength, and different instabilities like domain boundaries and folds. Also along with the experimental work, simulations for the shells in different shapes were also predicted in this paper, as shown in

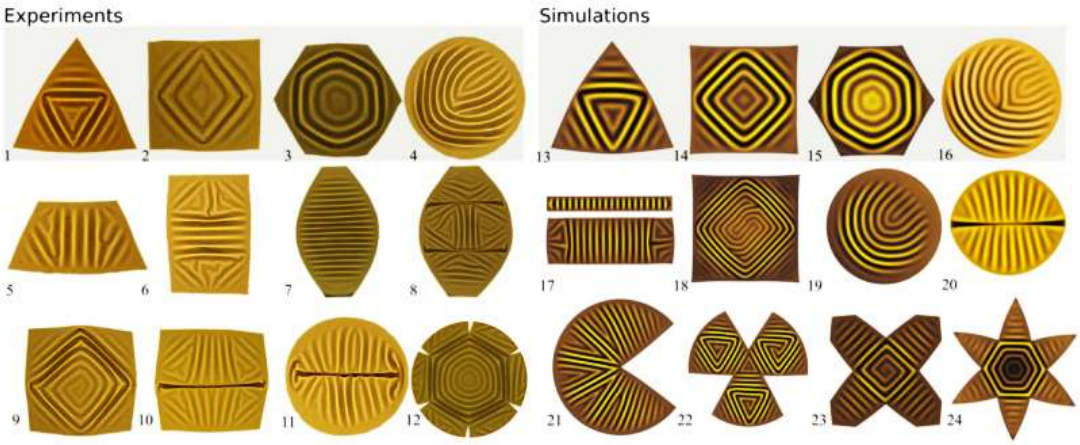

Figure 4.1: Patterns formed in floating shells with various geometries, obtained from experiments (left) and simulations (right). Experimental shells were imaged using shadowgraphy, while simulation images show surface displacement with a similar colour scheme. The identified patterns encompass various formations including single (7, 17) and multiple (e.g., 1-3) domains of straight wrinkles (7, 17, 21), curved wrinkles (4, 16, 19), folds (8, 10, 11, 20), flattened boundaries (19), and dislocations (4, 16), among other configurations. Image adapted from Albarran et al. [13].

Figure 4.1.

In their work on wrinkling, Aharoni et al. [145] had showed that the wrinkling patterns formed in thin curved elastic films have direct analogies with the behaviour of smectic-liquid crystals and other patterned systems, for a vast parameter regime. A key assumption in this theory was the scale separation between the wavelength of the wrinkles and the other length scales in the system, which include the control parameters like the thickness and radius of curvature of the film, as well as the emergent length scales like the amplitude. This work also explains the appearance of wrinkle domains formed in thin curved films in analogy with liquid crystals. As shown in Figure 4.1 a floating thin film can break into different domains, which are separated by interfaces or domain walls across which the direction of the wrinkles changes. In their work, it was also shown that the maximum amplitude across the wrinkles in a domain is proportional to the size of that domain.

Tobasco et al. [14, 15], in their recent work, derived a set of rules that predict the nature of curvature-driven wrinkling, with the help of a stress-like Lagrange multiplier. As discussed in Chapter 1, Gaussian curvature $\kappa = \kappa_1 \times \kappa_2$ where κ_1 and κ_2 corresponding to the maximum and minimum values of the curvature in different directions as shown in Figure 2.1. For shells with negative Gaussian curvature (both positive and negative principal curvatures), for instance, a

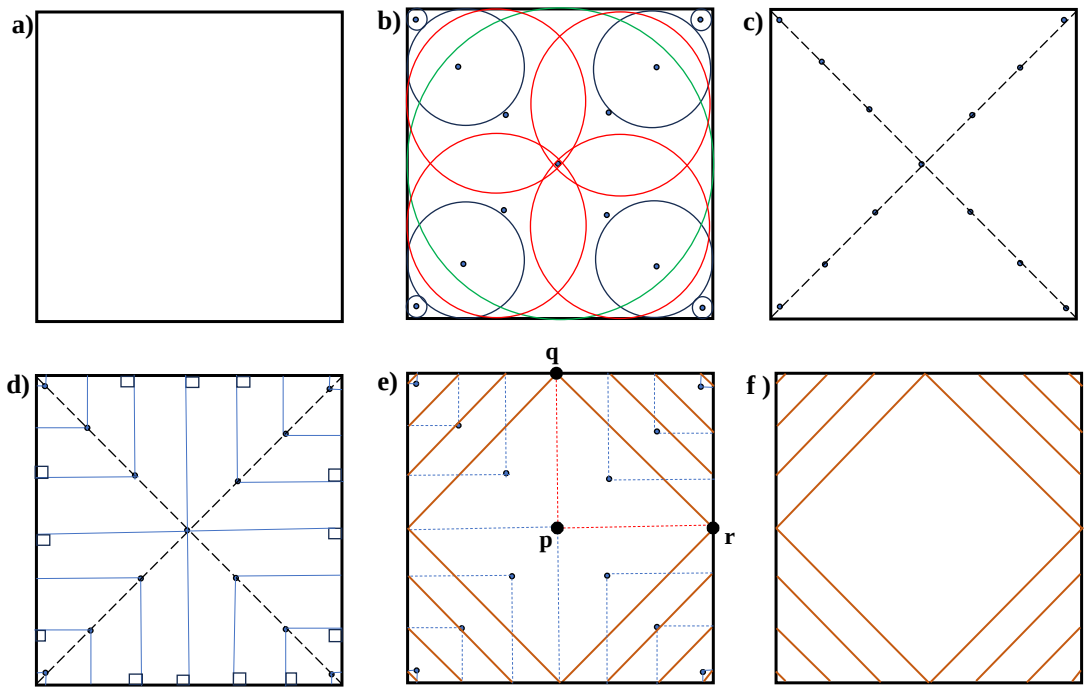

Figure 4.2: The paths chosen by (a) a film with a square geometry, to form wrinkles. According to the theory of Tobasco et al. [14, 15], a medial axis of a geometry is formed by connecting the points that are equidistant from at least two boundary edges. (b) This is same as the points defined by a circumscribed circle tangent at at least two points on the periphery. (c) In other words, the centre of these circles describes the medial axis. (d) Wrinkles in shells with negative Gaussian curvature are expected to arrange themselves in the quickest exit path that is also perpendicular to the boundary and coincides with the medial axis. (e) The ends (q and r) of two coinciding wrinkle lines (pq and pr), are joined to form an isosceles triangle with the new line segment (qr) forming the domain boundary for the oppositely curved shell. (f) All the wrinkle direction lines (stable lines) are shown for the reciprocally related curved shell with positive Gaussian curvature.

saddle shape, the wrinkles are formed along the direction perpendicular to the closest periphery of the geometry. This path inherently allows for the quickest exit from the cut-out shape. These perpendicular paths coincide with the medial axis of the film as illustrated in Figure 4.2. The medial axis of a shape represents the "centre line" or "skeleton" of that shape. The medial axis consists of the points where you can draw a line that is equidistant from at least two sides of the shape's boundary, for example the centre line of a narrow wedge shape. Another concept that is important to introduce here is the concept of stable lines. These are paths or lines parallel to the direction of the wrinkles, and represent the lines along which the wrinkles are most stable

and well-defined. Both concepts are explored through a graphical example in Figure 4.2

Tobascco et al. [14] showed a reciprocal correlation between the wrinkling domains of oppositely curved shells. This reciprocal relationship could have interesting implications for understanding and predicting the behaviour of wrinkled films. This is derived from the concept of reciprocal figures as originally presented by Maxwell [14, 146]. This new class of reciprocal rules suggests that there might be a fundamental connection between the deformation mechanisms of oppositely curved shells.

Figure 4.2(d) shows the wrinkling domains, medial axis (black dashed lines) and wrinkling direction lines (blue solid lines) of a negative Gaussian curvature shell. It should be noted that these wrinkle lines coincide at the medial axis forming a pair (for instance line segments 'pq' and 'pr') as shown in Figure 4.2. The ends of these paired wrinkle lines (pq and pr) can be joined to form an isosceles triangle and the newly formed line segment,'qr' (brown solid line) denotes the boundary of the domain for the oppositely curved shell (reciprocal figure denoting the positive Gaussian curvature shell domain). These are shown in Figure 4.2(f).

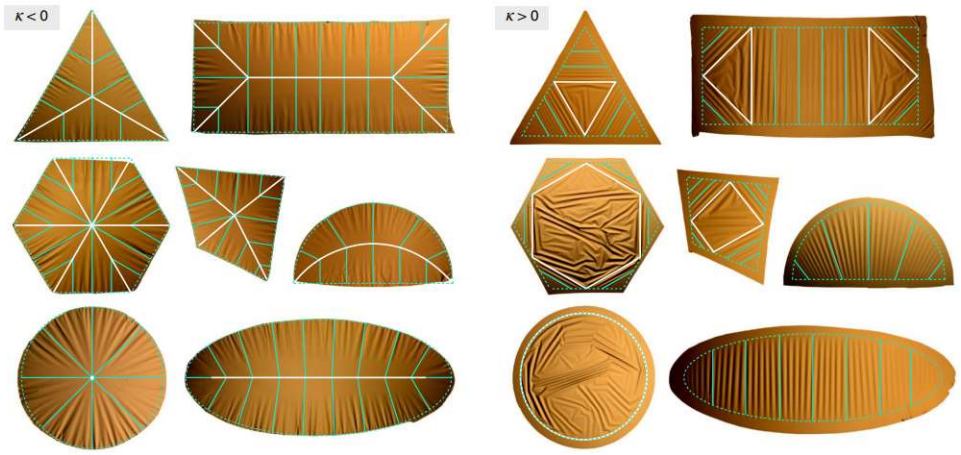

Figure 4.3: For cutouts of different shapes of different Gaussian curvature κ, the solid cyan line represents the direction of wrinkles, within the regions of ordered wrinkles, while regions without these lines indicate the regions of disordered wrinkles. The medial axis shown as a set of white lines delimits the film into domains. For saddle-shaped shells, wrinkles decay toward the medial axis, and for spherical shells, wrinkles decay toward the boundary. The dotted cyan curves illustrate the ideal shapes used in the predictions and flattened regions are excluded. Image is adapted from [14].

Finally, according to the rules derived by Tobasco, in shells with positive curvatures, there are domains in which wrinkles are formed in an orderly fashion and the location of these domains

is also consistent. However, for some shapes, including circular or hexagonal-shaped thin shells, domains of disordered wrinkles are also observed, whose location is defined but where the other wrinkle characteristics like the orientations are random, these disordered regions had previously been noticed [13, 145], but not explained. Secondly, these domains are divided up, based on the medial axis or the skeleton of the geometry of the shell. The white lines given in Figure 4.3 represent the medial axis of different shape cutouts of thin curved films. Another rule that was predicted was that in ordered domains the arrangement of wrinkles depends solely on whether the surface is positively or negatively curved (i.e. the sign of the Gaussian curvature) and not on the magnitude of the curvature. The goal of this chapter is to validate these and the related predictions in shells with varying Gaussian curvature and principal curvatures.

4.2 Parameters and dimensional analysis

Dimensional analysis is a method to study the relationship between physical quantities depending on their units and physical dimensions. It is a method to reduce the number of variables and simplify a physical problem by bringing dimensional homogeneity. It is useful in checking mathematical equations, interpreting experimental data, modelling, developing the significance of a particular phenomenon, etc. [147]. One famous theorem used in dimensional analysis is the Buckingham Π-theorem which states that in a physical problem if there are m variables that have n independent dimensions, then one can generate $(m-n)$ dimensionless groups connecting the variables used in the problem [147–149].

Besides the extent or length of the film W, there are five parameters that are thought to affect the wrinkling pattern of a floating film [13]. The first parameter is the stretching modulus Y, which shows how much the material is resistant to elastic deformation when an external force is applied. It characterises the energetic cost of changing the surface area of the film and is given by the equation, $Y = Et$, where E is the Young's modulus of the material and t is the thickness of the thin film [14]. Secondly, the Gaussian curvature, $\kappa = K_1K_2$, is expected to uniquely characterise the effects of the shell curvature, based on the Gauss Theorem Egregium [150, 151]. Next, the bending modulus B, given by $B = Et^3/[12(1-\nu^2)]$, characterises the relative difficulty of local bending (changing the principal curvature, while keeping the Gaussian curvature constant) or flexing of the film, where ν is the Poison ratio. For $\nu = 1/2$ which is a reasonable assumption for a polymer like PDMS [98, 99], $B = Et^3/9$. Another mechanical parameter is the gravitational stiffness K_g, which in this case is the specific weight of the fluid on which the film is placed, given by $K_g = \rho g$ where ρ is the fluid density and g is the magnitude of the acceleration due to gravity. Finally, the last relevant parameter is the surface tension γ_{lv},

Parameters	**Symbol**	**Dimensions**	**Experimental range**
Film width	W	L	5×10^{-2} m
Bending stiffness	B	F L	$(1.2 - 5.2) \times 10^{-7}$ N m
Gravitational stiffness	K_g	F L^{-3}	9.8×10^{3} Nm^{-3}
Stretching modulus	Y	F L^{-1}	$(1.76 - 2.83) \times 10^{2}$ Nm^{-1}
Surface tension	γ_{lv}	F L^{-1}	7.2×10^{-2} Nm^{-1}
Gaussian curvature	$\lvert\kappa\rvert$	L^{-2}	$(0.5 - 4) \times 10^{2}$ m^{-2}

Table 4.1: Dimensions and experimental range for the parameters affecting the wrinkling pattern of a floating film. Here, F and L denote force and length dimensions respectively. Force (F) has dimensions [MLT^{-2}] where M is mass and T is time.

which characterises the additional forces acting on the edges of the thin film from its surrounding water bath [14].

In the experiments performed in this work, the width W of the film is 50 $\pm$ 1 mm and its thickness, t ranges from 80 μm to 129 μm. The Young's modulus, E, of the PDMS film is 2.2 MPa which was measured using the tensile test as given in section 2.2, and the Poisson's ratio is assumed to be $\nu = 0.5$ [98, 99]. The surface tension γ_{lv} of water is taken to be 0.072 Nm^{-1} [14,152]. By substituting the range of thickness of the thin films and the Young's modulus of the PDMS into the equation of bending modulus, the bending modulus is found to be in the range of 10^{-6} Nm.

Considering the total energy (U) of the system, there can be contributions parameters mentioned above, which are the bending energy (U_B), stretching energy (U_S), gravitational energy (U_g) and the surface energy (U_γ). By applying the Buckingham Π-theorem to this system, which involves six variables and two dimensions, we obtain four dimensionless groups as a result. One group is taken to be the angular size of the cutout of the thin film, $W\sqrt{\kappa}$. The other three dimensionless groups [15] are:

$$\Pi_1 = \frac{B}{YW^4\kappa} \qquad \Pi_2 = \frac{K_g}{\kappa\, Y} \qquad \Pi_3 = \frac{\gamma_{lv}}{Y}\frac{1}{W^2\kappa}. \tag{4.1}$$

These three groups can be defined as the ratios of the typical energy scales in the wrinkling problem. The first group Π_1 is approximately the ratio of the bending energy and the stretching energy, Π_2 is the ratio is gravitational and stretching energy and the last group Π_3 is the ratio of energy due to surface tension and the stretching energy. These dimensionless groups can also be considered as the ratios of three independent length scales of deformation. The first parameter

is the curvature κ, the second is a length scale of the form $\Lambda = (B/K_g)^{1/4}$ which is generated by balancing the bending energy and its gravitational energy. The third length scale is $\Gamma = \sqrt{t}/\kappa^{1/4}$, which shows the scale at which the bending energy becomes comparable to the stretching energy in order to flatten the curved film. It is an important length scale according to the elastic theory of shells and is also used in determining the critical condition for buckling, the wavelength of anisotropic blisters, etc. [153, 154].

By substituting the experimental values to the parameters mentioned above, one finds that $\gamma_{lv}\kappa^{-1} \ll YW^2$ which proves the experiments are happening in the limit of a weak tension. Similarly, $BK_g\kappa^{-2} \ll Y^2W^4$ which shows that the problem has a small bending stiffness. Since the surface tension γ_{lv} is very small compared to the other parameters the third dimensionless group has been assumed to be negligible [14]. Also since Y^2W^4 is much greater than the product of the bending modulus and the gravitational stiffness, the contribution from stretching energy is also neglected in this experiment. So here, it's the bending energy and the gravitational energy that drives the wrinkling phenomenon.

4.2.1 Theoretical predictions

To understand the underlying concept of deformations for the case of wrinkle formation on thin films, it is imperative to understand a core concept of continuum mechanics called the 'Euler elastica' [155, 156]. The initial idea of the Euler elastica was developed to understand the deformation of thin solids, like wooden beams and sheets, and their response to external forces and geometric constraints [156]. An assumption behind the Euler elastica, in simple terms, is that thin materials prefer bending over stretching [155, 157]. This preference arises because thin materials require less energy to bend compared to stretching. cite.

Mathematical functions that represent solutions to Euler's elastica arise from two key principles that blend mechanics and geometry. Firstly, the bending dominance over stretching is observed because, for a rod (or sheet) with thickness t, the ratio of bending stiffness to stretching modulus scales as $\sim t^2$. Secondly, Euler's elastica introduces the notion of 'isometric deformations'. This concept implies that materials can be confined within certain shapes without subjecting their central axis to stretching. This approach guides the path towards equilibrium states with minimal energy.

The research aims to prove the validation of Euler's elastica and the preference for bending deformation over stretching. Furthermore, it is essential to draw conclusions about the geometric characteristics, namely, the wavelength and the amplitude of wrinkling in a curved thin film under isotropic deformation, and observe the effects of curvature on these two parameters.

Within the context of this research, two fundamental questions require explicit clarification. Firstly, to discern whether the wavelength maintains consistency in the films with various curvatures, regardless of whether the Gaussian curvature is positive or negative. The second key question in this research revolves around investigating how variations in curvature affect wrinkle amplitude. Specifically, it aims to ascertain whether alterations in curvature result in noticeable changes in wrinkle amplitude, and if they do, how? According to Albarran et al. [13], the amplitude of wrinkles depends on the excess area needed to accommodate a curved film on a flat surface and is therefore proportional to the product of curvature and the width of the film, as given in Figure 4.4.

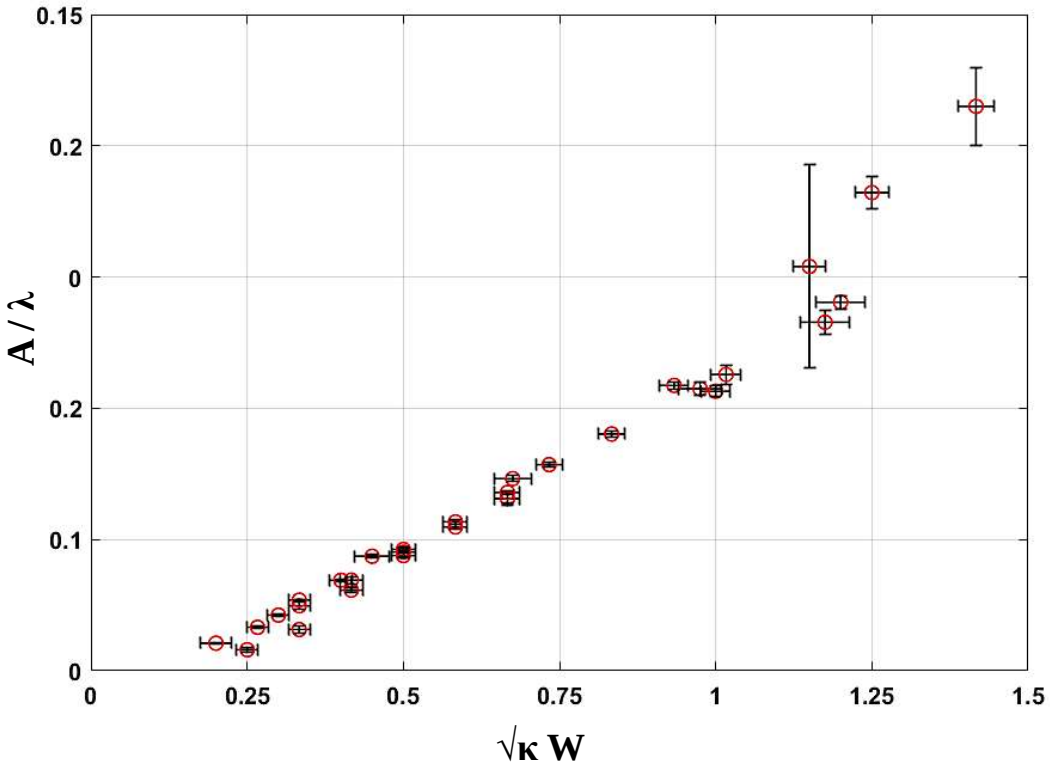

Figure 4.4: The plot shows how the maximum amplitude of the wrinkles A, formed on shells having positive Gaussian curvature κ varies with the curvature and the width W of the film. This explains that the A/λ is related to the excess surface area of the film. Here λ is the wrinkle wavelength. Adapted from [13].

A more subtle question which is addressed in this project is how the amplitude develops with distance from the edge of the film. As a further approach, this project focuses on the following question: does only the parameter Gaussian curvature κ, matter or affect wrinkling patterns, or do the principal curvatures K_1 and K_2 also affect the wrinkles? Another question that is answered through this project is whether the direction of wrinkles is important, or in other

words, does the direction of wrinkles are affected by the principal curvature κ_1 and κ_2 or just the Gaussian curvature κ?

4.3 Results

To answer the above-mentioned questions thin PDMS films were prepared using the method explained in section 2.2 for saddle-shaped substrates and hemispherical shells. These surfaces have negative and positive Gaussian curvature, respectively. The imaging methodology discussed in Chapter 3 was followed and the wrinkled topology of the surface of the floating experiment shells for both the signs of curvature was generated using the MATLAB software, with some example results given in Figure 4.5.

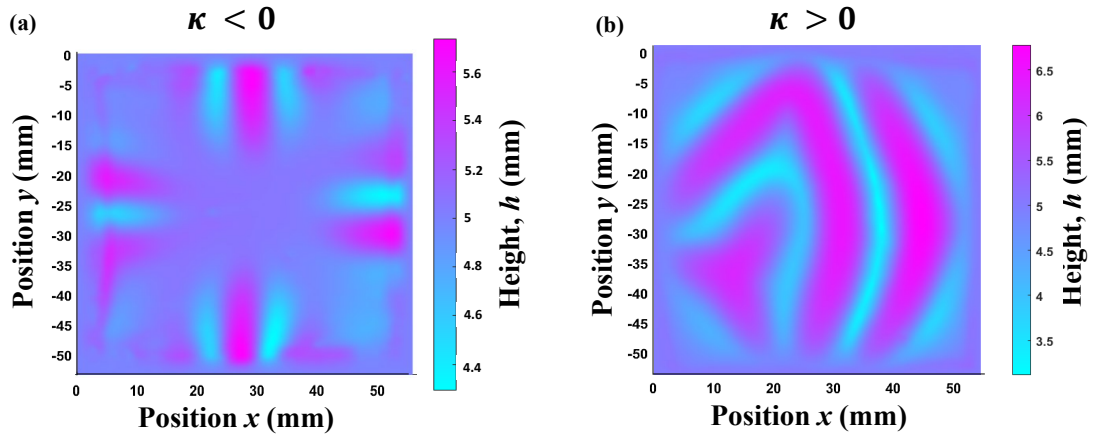

Figure 4.5: Processed images of the height profiles of floating PDMS films following the methods given in Chapter 3. Panel (a) shows the height values using a colour plot for the wrinkled film with the radius of curvatures $R_1 = 120$ mm and $R_2 = -70$ mm and (b) shows the plot of a film with the principal radii $R_1 = 120$ mm and $R_2 = 120$ mm. The height values were computed as explained in section 3.3.2.

Figure 4.5 shows the difference in the wrinkling pattern formed on a PDMS film having a positive ($\kappa > 0$) and negative Gaussian curvature ($\kappa < 0$). The desirable characteristics to be computed were the amplitude and wavelength of the observed wrinkles. The wavelength of a wrinkle refers to the distance between two consecutive crests or troughs of the wrinkle pattern. It is a measure of the spatial periodicity of the wrinkle. The amplitude of a wrinkle refers to the maximum deviation or displacement of the wrinkle pattern from its baseline or reference level. It represents the magnitude or height of the variation in the wrinkle profile. Once the 3D surface

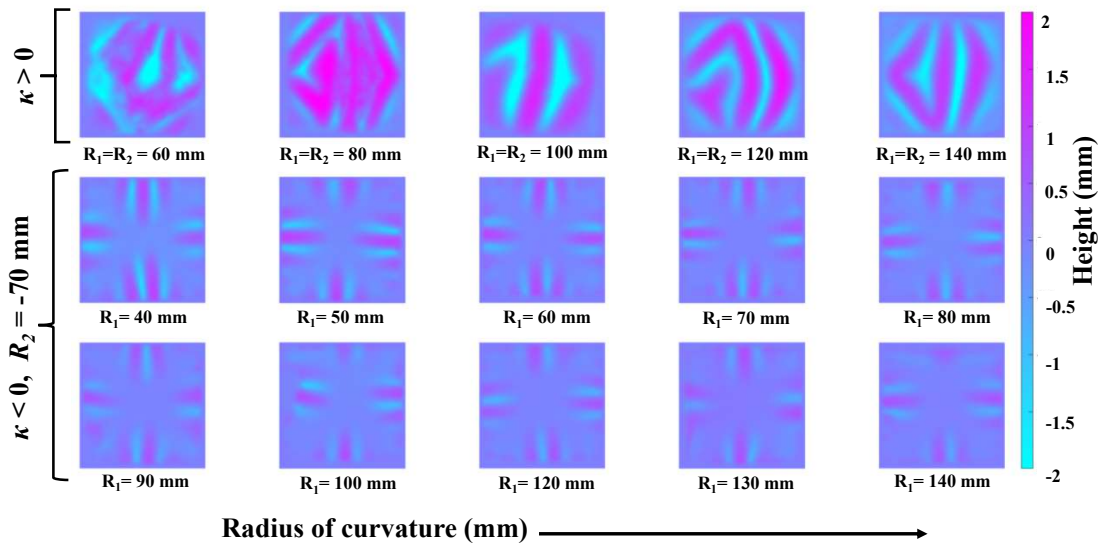

Figure 4.6: Topographical representation of wrinkles in both positive and negative curvature. The top row shows the heights of the wrinkling pattern formed on hemispherical shells ($\kappa > 0$) whose radius of curvature varies from $R_1 = R_2 = R = 60$ mm to 140, mm with a step size of 20 mm. The second and third rows highlight the wrinkle height of saddle-shaped ($\kappa < 0$) films for different radii of curvature with $R_2 = -70$ mm and R_1 varying from 40 mm to 140 mm, with a step size of 10 mm.

of the wrinkled film was extracted, the local minima and maxima of the wrinkled surface were determined from the computed height values using the method described in section 3.3.2. A prominence value of 0.2 was used as a tolerance for evaluating local extrema. To ascertain the wavelength characteristic of the wrinkle, in every individual section peak to peak distances (from one local minima to the adjacent local minima or one local maxima to adjacent local maxima) were calculated and stored in a matrix. The root-mean-square (RMS) value of these observations accounted for the wavelength value of the particular wrinkled thin film. For the amplitude of the wrinkled film, a similar approach was adopted, as explained in section 3.3.2, first the height values for all the local extremas was calculated and the RMS value of the vertical distances of these local extrema points was taken as the amplitude of the wrinkle. The processed images of height profiles for the curved with both positive and negative curvatures are illustrated in Figure 4.6.

In this part, the concept of the stable lines mentioned in the theory work by Ian Tobasco [14] is compared with the experimental data. As introduced before, the method of stable lines helps determine certain properties of the wrinkles and their geometric behaviour. These lines divide

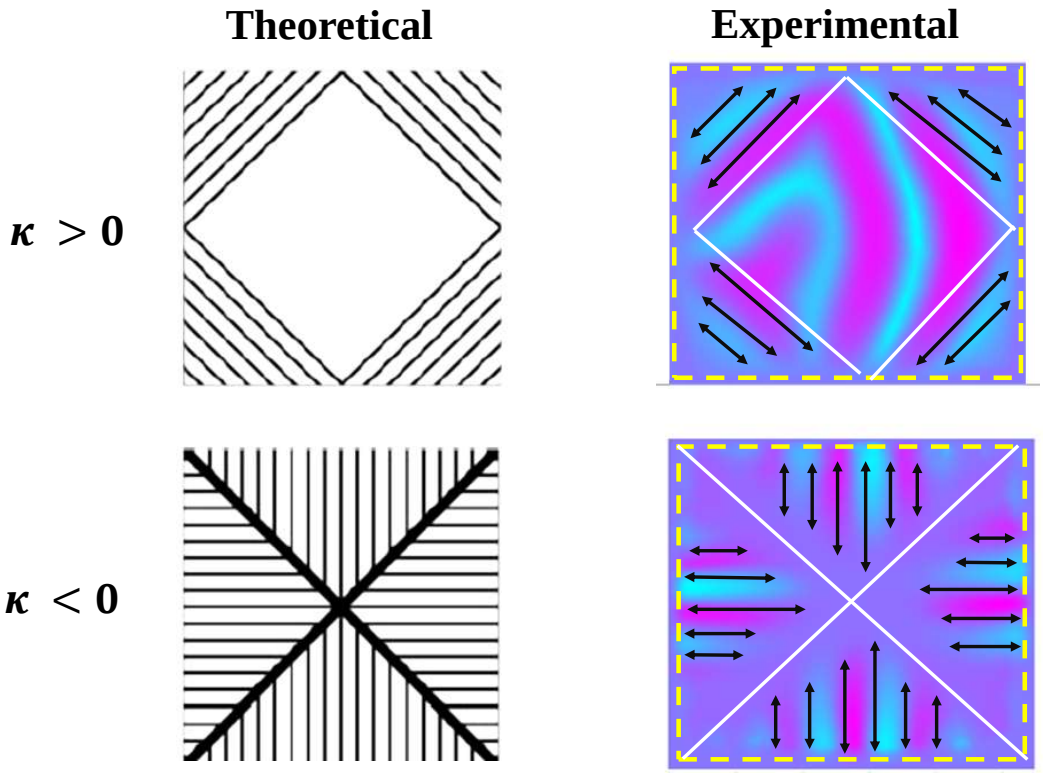

Figure 4.7: The theoretical illustration shows the stable lines present in positively curved shells and negatively curved films according to Tobasco [15]. Stable lines correspond to the ordered regions of the shell, while any disordered behaviour should occur in areas where these lines are absent (depicted as blank spaces). In the experimental illustrations regions covered by black arrows are predicted to be ordered. Any disorder is predicted to occur in regions absent these lines. For saddle shells, wrinkles decay towards the medial axis in white. For spherical shells, wrinkles decay towards the boundary. Dotted yellow curves show ideal shapes used in the predictions.

the wrinkled film into different regions, namely, the ordered and disordered domains. In the ordered region the wrinkles should be well-organised and follow the stable lines [15].

Tobasco et al. considered the energy minimisation process that led to the formation of patterns on the thin film by utilising the tension field theory, which involves an expansion about a tension-free state, to describe the process of wrinkling [14]. In this work, the emergence of wrinkle patterns on thin shells was explained using the concept of locking stress as an order parameter to predict the type and layout of these patterns [14, 15].

By studying these stable lines on a wrinkled film it helps to gain an insight into the charac-

teristics, topography and geometry of the wrinkles. Figure 4.7 shows these stable lines for both positive and negative Gaussian curvature wrinkled films and compares the theoretical model with the experimental observations. The stable lines have been traced on the imaged wrinkled patterns for easier visualisation and comparison. The stable lines formed on the experimental film match with the theoretical predictions as shown in Figure 4.7. The reciprocal correlation between wrinkle domains in both positive and negative Gaussian curvature mentioned in the introduction of this chapter is also thus verified.

4.3.1 Characteristic 1: Wavelength

To answer the question of whether the wavelength of the wrinkles of the film varies for different curvatures, the PDMS films were prepared on saddle-shaped and hemispherical substrates with different curvatures. The wavelengths of each film were determined using the imaging methodology mentioned in section 3.3.2 and the thickness of the film was determined using optical coherence tomography (OCT) as explained in section 2.3. By balancing the substrate stiffness K_g and the bending stiffness B, the predicted wavelength of the wrinkles [24, 123, 158] can be written as:

$$\lambda = 2\ \pi\ \left(\frac{Et^3}{9\ K_g}\right)^{1/4} = 2\ \pi \left(\frac{B}{K_g}\right)^{1/4} = 2\ \pi\Lambda, \tag{4.2}$$

where all symbols are defined as in the introduction to section 4.2 of Chapter 4.

According to Equation 4.2, the ratio of the wavelength λ to the thickness t is independent of the Gaussian curvature κ. Furthermore, experimental evidence demonstrates that the aforementioned ratio remains unaffected by both positive $\kappa > 0$ and negative $\kappa < 0$ curvatures, as illustrated in Figure 4.8.

Considering the dimensionless group derived from the substrate stiffness, which is $\Pi_2 = K_g/\kappa\, Y$, where $Y = Et$ [14], the dimensionless parameter of a specific thickness τ can be written as:

$$\tau = Et\kappa/K_g = 1/\Pi_2. \tag{4.3}$$

Equation 4.3 can be written in terms of a ratio of lengths scales Λ and Γ where, $\Lambda = (B/K_g)^{1/4}$ and $\Gamma = \sqrt{t}/\kappa^{1/4}$, as $\tau = Et\ \kappa/K_g = (\Lambda/\Gamma)^4$. Figure 4.9 shows the results for the normalised wrinkle wavelength over the range of specific thickness (τ) and the length scale Γ used in the work. The plot has both the experimental data and theoretical prediction for both positive and negative Gaussian curvature, which show great agreement with each other. The black dotted line in Figure 4.7 is the theoretical value for the elastica model for both the normalised wrinkle wavelength which is $\lambda/\Gamma = 2\pi(\tau/9)^{1/4}$ and $\lambda/\Lambda = 2\pi$. This confirms that the wrinkle wavelength,

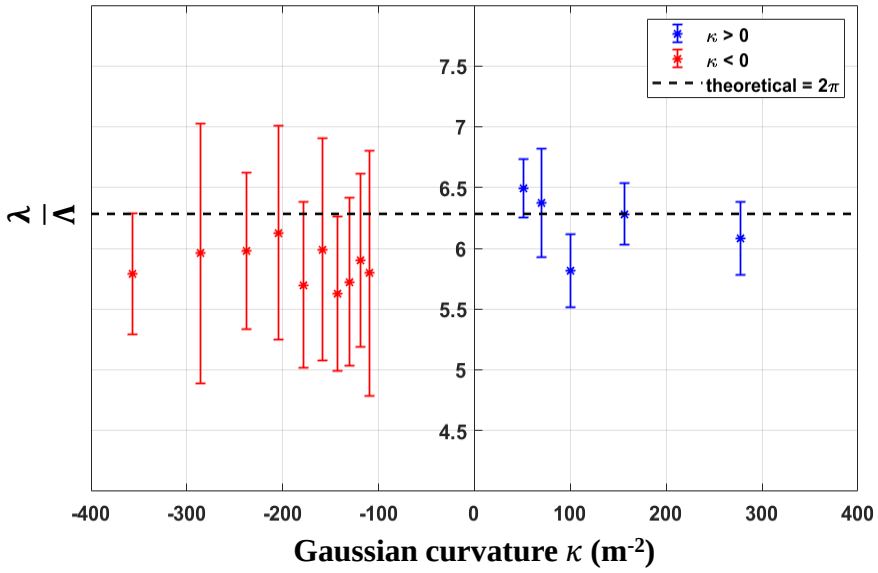

Figure 4.8: Measurement of wavelength and thickness. The plot shows how the ratio of wavelength λ and the natural length scale Λ varies with the Gaussian curvature. The red data points correspond to the film with $\kappa < 0$ and the blue data points correspond to the film with $\kappa > 0$. The black dashed line is the theoretical value of $\lambda/\Lambda = 2\pi$. The error bars represent a standard deviation in λ/Λ calculated by error propagation.

λ, only depends on $\Lambda = (B/Kg)^{1/4}$ and not on the sign and magnitude of the other significant length scales, such as the curvature κ, Γ or τ.

4.3.2 Characteristic 2: Amplitude

This section addresses the research question regarding the dependence of wrinkle amplitude on curvature. The primary objective is to investigate how the amplitude of the wrinkles is influenced by factors such as the film curvature and width. This phenomenon can be explained by considering the analogy of a curved cap kept on a flat surface. This excess surface area comes from the stretching or bending of the material to accommodate the new shape, and it represents a form of stored energy within the material. This surface area is more than the projected flat surface. For a 2D case, this is analogous to the excess arc length of an arc in contrast to the length of the chord in a segment of a circle both subtending an angle θ. Here the height of the segment is comparable to the amplitude of the thin film.

To calculate the amplitude of the wrinkles, using the imaging methodology 3.3.2, first, the absolute difference between the heights of the wrinkled film and the height of the water level was evaluated. Following this, the local maxima of the film (prominence: 0.2) were determined

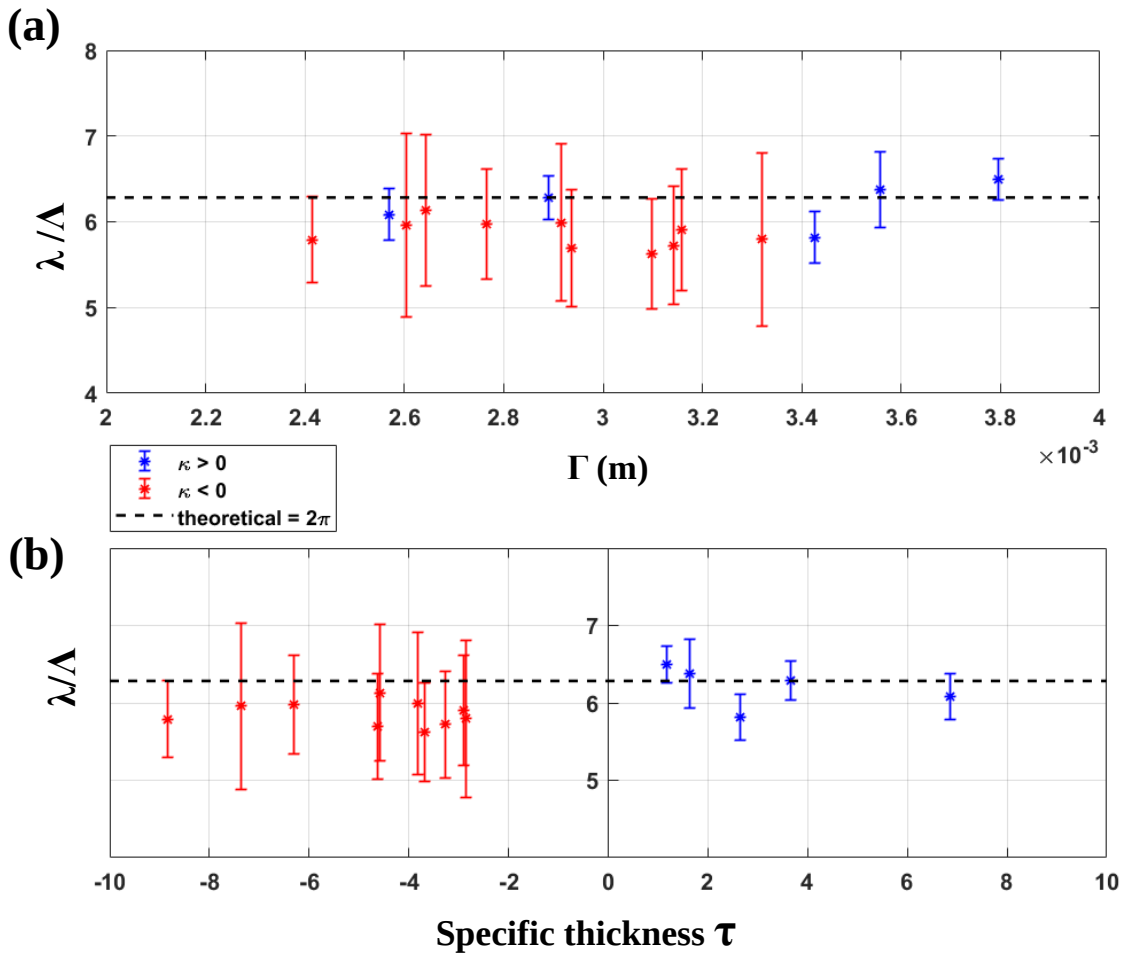

Figure 4.9: The wrinkle wavelength λ, normalised by the deformation length $\Lambda = (B/Kg)^{1/4}$, versus the (a) the length scale $\Gamma = \sqrt{t}/\kappa^{1/4}$ and (b) the specific thickness of the shell, $\tau = Et\,\kappa/K_g$. The dashed lines indicate the elastica model for the normalisations, $\lambda/\Lambda = 2\pi$.

throughout the film. The mean of these values was considered to be representative of the amplitude of the whole film. This process was repeated for the films with different curvatures.

To derive the relation of the amplitude of the wrinkle theoretically, consider a sine wave with the function $y = A\sin(qx)$, where A is the amplitude, and q is the wavenumber of the wave, which is equal to $2\pi/\lambda$. Let L_s be the arc length of the sine wave [159], which is given by:

$$L_s = \int_0^{l_s} \sqrt{1 + \left(\frac{dy}{dx}\right)^2}\, dx \tag{4.4}$$

$$= \int_0^{l_s} \sqrt{1 + A^2 q^2 \cos^2(qx)}\, dx. \tag{4.5}$$

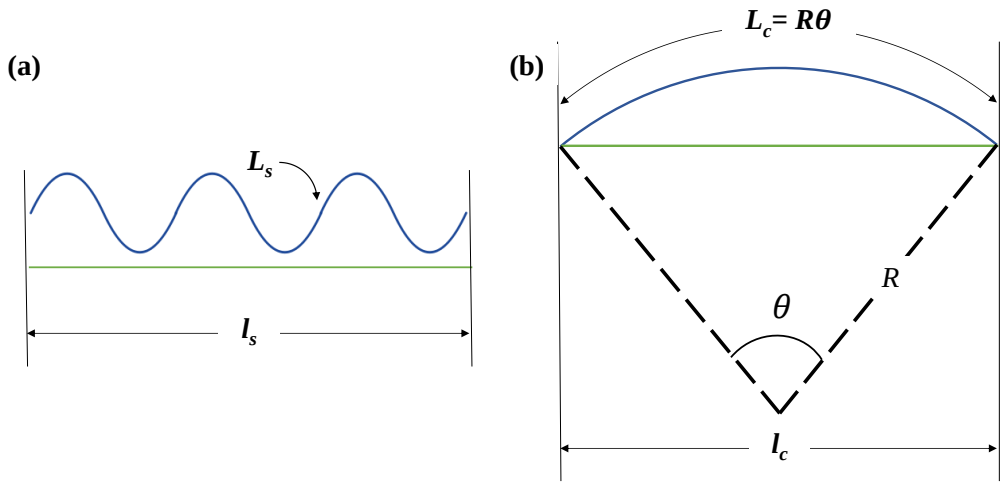

Figure 4.10: Schematic diagram showing the (a) arc length, L_s of a sinusoidal wrinkle along with the projected length, l_s and (b) arc length, L_c of a curved film with the projected length, l_c.

Assuming $Aq \ll 1$, using the Taylor series the arc length can be written as:

$$L_s = \int_0^{l_s} 1 + \frac{A^2q^2cos^2(qx)}{2} + \mathcal{O}\big((Aq)^4\big)dx \tag{4.6}$$

$$= l_s(1 + \frac{A^2q^2}{4} + \mathcal{O}\big((Aq)^4\big)), \tag{4.7}$$

where l_s is the projected length as illustrated in Figure 4.9 (a).

Therefore the effective strain or the relative amount of the excess length for the sinusoidal wrinkle (2D), $\epsilon_s = (L_s - l_s)/l_s$, can be written as:

$$\epsilon_s = \frac{1}{4}A^2q^2 + \mathcal{O}\big(A^4q^4\big) \simeq \ \pi^2A^2/\lambda^2. \tag{4.8}$$

Now, if we consider an arc formed by a circle of radius R, the arc length $L_c = R\theta$, where θ is the angle subtended by the arc at the centre of the circle. Let l_c be the length of the chord as shown in Figure 4.10(b), which is also the projected length of L_c. Therefore, the excess length can be written as the difference between the arc length L_c and the chord length, l_c. It should be noted that l_c also equals the width W of the PDMS film square cut-outs. In the experiments $l_c = W = 55mm$. In contrast to the effective strain formed in a sinusoidal wave (Equation 4.8), the effective strain for the circular arc film (2D), ϵ_c can be evaluated as:

$$\epsilon_c = \frac{l_0}{l_c} = \frac{R\theta}{l_c} - 1. \tag{4.9}$$

Using the Pythagoras theorem,

$$\sin\frac{\theta}{2} = \frac{l_c}{2R}. \tag{4.10}$$

By rearranging Equation 4.10, it can be written as:

$$\frac{\theta}{2} = \arcsin\frac{l_c}{2R}. \tag{4.11}$$

Using the Taylor series for the $\arcsin(l_c/2R)$, Equation 4.11 can be written as:

$$\frac{\theta}{2} = \frac{l_c}{2R} + \frac{\left(\frac{l_c}{2R}\right)^3}{3!} + \mathcal{O}\big((l_c/R)^5\big). \tag{4.12}$$

Substituting the equation for θ in the equation for strain,

$$\epsilon_c = \frac{R\theta}{l_c} - 1 = \left(\frac{l_c}{R}\right)^2 \frac{1}{24} + \mathcal{O}\big((l_c/R)^4\big). \tag{4.13}$$

Ignoring the higher-order terms gives, 4.13 reduces to

$$\epsilon_c = \left(\frac{l_c}{R}\right)^2 \frac{1}{24}. \tag{4.14}$$

Finally, from the definition of Gaussian curvature κ, the factor of $1/R^2$ in equation 4.14 can be substituted as κ.

It should be noted that the sinusoidal arc and the circular arc are representative of the cross-section of the wrinkled curved thin film shells. Since the thin film cutout perimeter remains the same in the water bath (assuming there is minimal stretching of the film), therefore the projected area remains the same as well. Consequently, the effective strains (ϵ_s and ϵ_c can be equated. By equating equation 4.8 and 4.14, the relation for the amplitude A can be written as:

$$\frac{\pi^2 A^2}{\lambda^2} = \frac{l_c^2 \kappa}{24}. \tag{4.15}$$

Replacing l_c by the width W of the film, we get a prediction of:

$$A = \frac{W\lambda}{\pi\sqrt{24}}\sqrt{\kappa} \tag{4.16}$$

$$A \propto W\lambda\sqrt{\kappa}. \tag{4.17}$$

In Equation 4.17, it is important to highlight that the prefactor of $\frac{1}{\pi\sqrt{24}}$ signifies a scaling coefficient which may vary depending on the exact shape of the wave, but the relation $A \propto W\lambda\sqrt{\kappa}$ should hold true generally. In this research, the amplitude of the wrinkled film varies along the extent of any wrinkled domain, rather than remaining constant everywhere. The amplitude of films with both positive and negative curvatures was plotted against the Gaussian curvature, which is given in Figure 4.11.

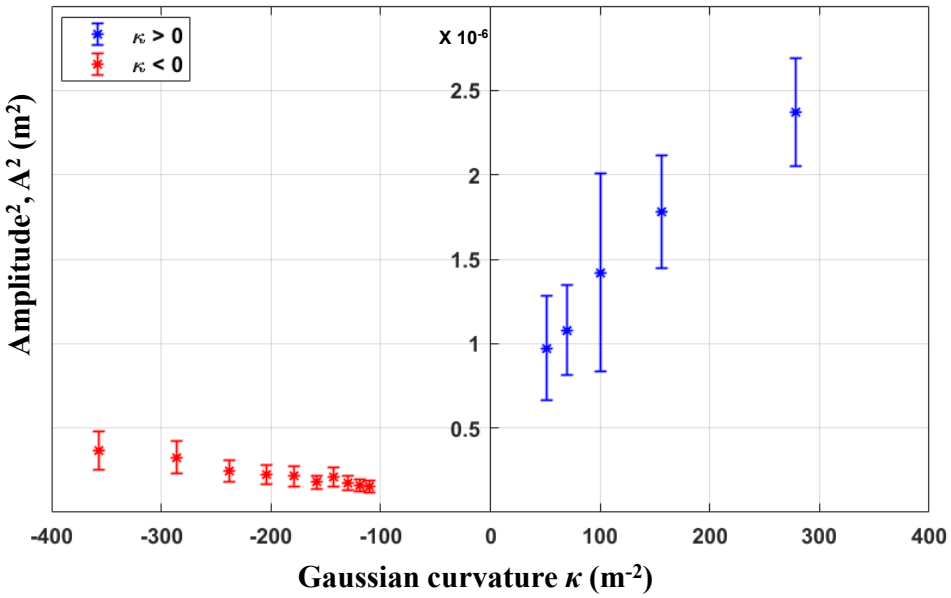

Figure 4.11: Plot showing how the amplitude varies with $\sqrt{\kappa}$. The blue and red data points are the squared values of amplitudes for the wrinkles films with negative and positive Gaussian curvatures respectively.

Figure 4.12 shows the relation between amplitude and Gaussian curvature in dimensionless forms derived from Equation 4.17. The magnitude of the two slopes of the plot were used to find the scaling prefactors for a hemispherical ($\kappa > 0$) and saddle-shaped ($\kappa < 0$) wrinkled film. The slopes were found out to be 0.01986 and -0.00233, resulting in the prefactor values of 0.1409 and 0.0480 for the positive and negative Gaussian curvatures, respectively. The theoretical coefficient ($1/\sqrt{24}\pi = 0.0649$) from the Equation 4.16 lies in the calculated prefactor range i.e., $0.1409 < 0.0646 < 0.0480$. The plot also verifies the dimensionless nature of the relation derived.

In the analysis above, a uniform sinusoidal wave is assumed to be analogous to the cross-section of the wrinkles formed. However, it is important to highlight that the wrinkles observed do not conform to a uniform wave cross-section. Therefore, it becomes imperative to study the effect of amplitude variation across a wrinkled film. The next research question which is answered through this work is how the amplitude develops with the distance from the edge of the film.

Similar, to the method utilised for calculating an amplitude value representative of the whole film, an amplitude value was computed at specific distance intervals from the edge of the films. This included evaluating the vertical distance (height or depth) of the highest or the deepest (respectively) point at ever 0.275 mm distance interval from the edge of the film travelling concentrically towards the centre, providing 100 data points for a film width of 55 mm. The

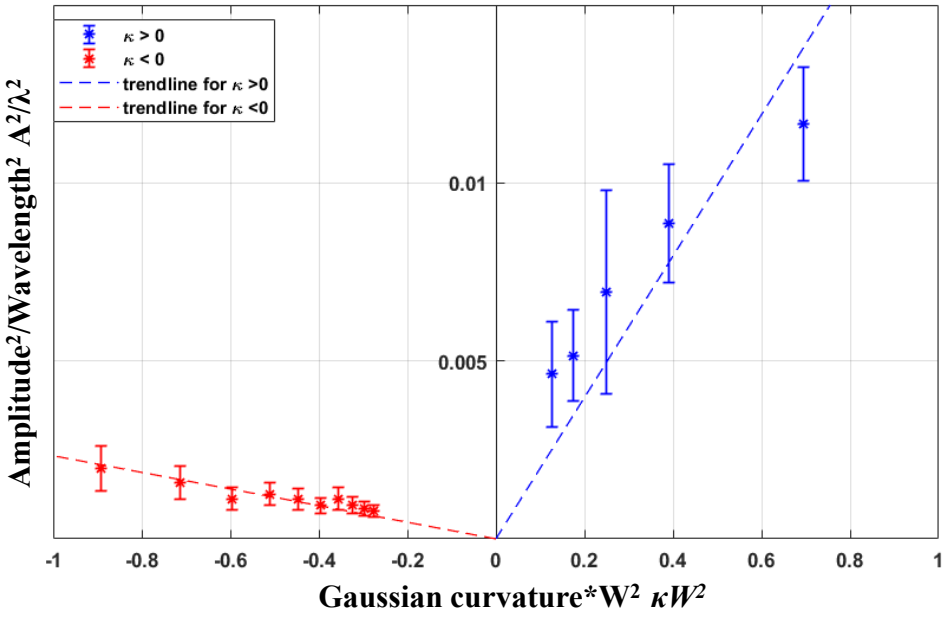

Figure 4.12: A comparison between the dimensionless scales of amplitude and Gaussian curvature. The plot shows a linear relationship with a slope value of -0.00233 and 0.01986 for the negative and positive Gaussian curvature.

interval of 0.275 mm was calculated by dividing the half width of the film by 100 (i.e., $55/2*100 = 0.275mm$) to get 100 concentric discreet levels.

Subsequently, a plot was generated to illustrate the relationship between the amplitude and the distance from the film's centre and edge, for the saddle and hemispherical thin film shells respectively. Figure 4.13 (a), illustrates how the amplitude of a film varies from the centre to the edge for films with negative curvature. The plot in Figure 4.13 (b) shows that for films with negative Gaussian curvature, the amplitude increases as you move towards the edge of the film. On the other hand, the bottom plot in Figure 4.13 (b) suggests that for films with positive curvature, the amplitude is highest at the centre of the film and decreases as you move towards the edge. In both the cases, there seems to be a flattened region of width ~ 5 mm at the edge or the centre of the film which is not predicted by the current theory. This could be the assumption of neglecting the stretching energy developed in the wrinkling process.

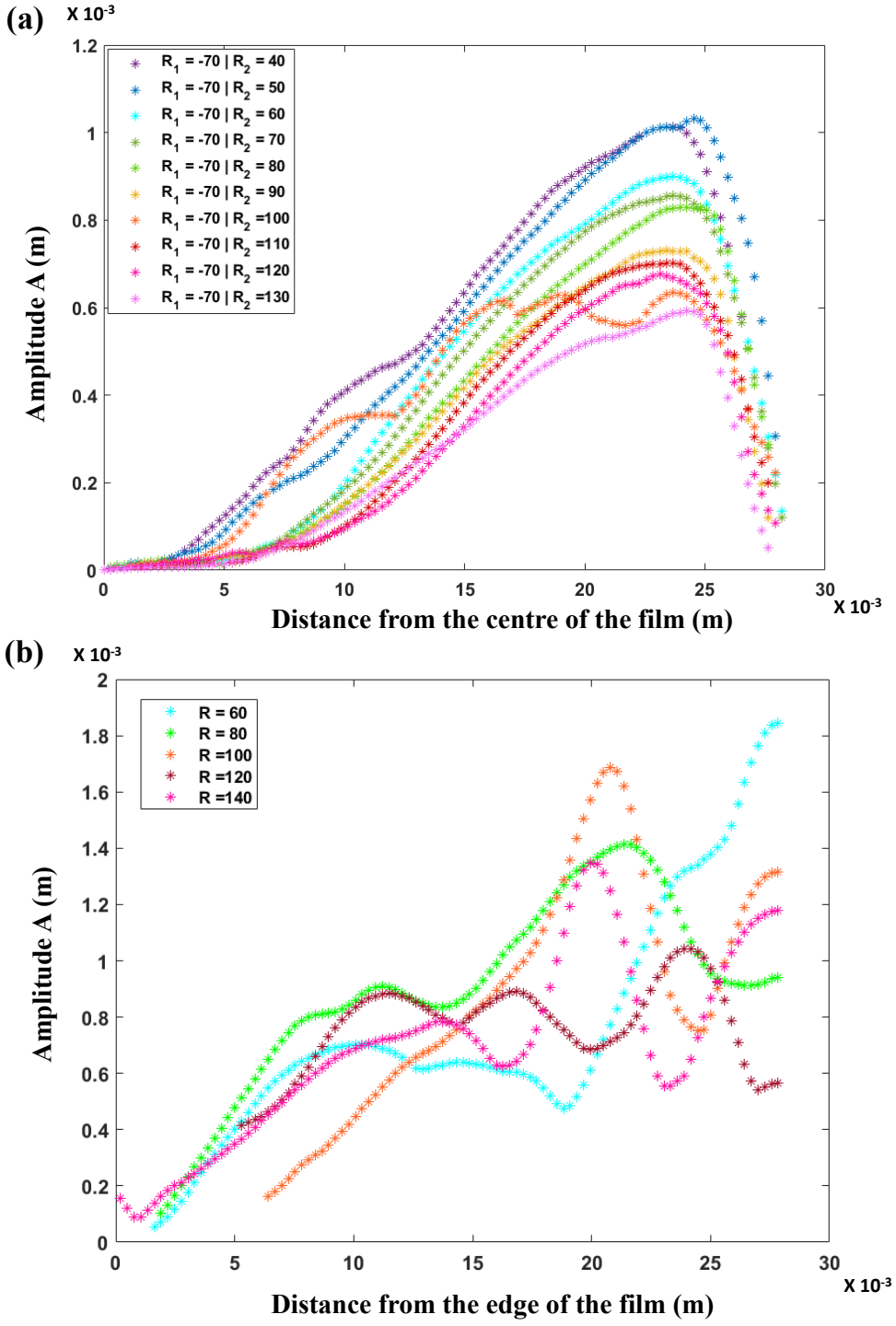

Figure 4.13: Plot showing how the amplitude varies from the centre of the film to the edge for films with (a) negative Gaussian curvature, $\kappa < 0$, and (b) positive Gaussian curvature, $\kappa > 0$. Different colours of data represent films with different radii of curvature.

4.4 Conclusions

In conclusion, this chapter has been devoted to a comprehensive investigation of wrinkling patterns in thin curved films, aiming to study the underlying phenomena and reveal some valuable insights. To begin with, I reviewed the non-dimensionalisation of the wrinkling shell system, which can be represented by a set of dimensionless groups that balance the energetic contributions of behaviours like bending, stretching or buoyancy. These dimensionless groups are fundamental to understanding the dynamics and interactions within the system and serve as essential tools for further analysis and interpretation.

Throughout the course of this research, significant attention was given to observing how the wrinkling patterns vary for different signs of curvature. The careful examination of these patterns has led to the discovery of intriguing variations in the system's behaviour, shedding light on the complex interplay between geometry and material properties.

Another critical aspect of this investigation revolved around the parameter of the wrinkle wavelength. By analysing the wrinkle wavelength for both positive and negative Gaussian curvature, it was observed that the wavelength is independent of curvature, which is in agreement with the recent theoretical predictions [13]. Also, it was verified that the dimensionless wrinkle wavelength, λ/Λ, is equal to a value of 2π, which was predicted by the elastica model [13].

Furthermore, this analysis extended to examining how the amplitude of wrinkling patterns correlates with varying curvatures. It was observed that the amplitude of wrinkles is linearly dependent on the Gaussian curvature, because as the curvature is increased, the excess area of the film is increased, which is compensated with the amplitude of the wrinkles. As an extension to the analysis, I also studied how the amplitude developed from the centre of the film to the edge. It was observed that for positive Gaussian curvatures the amplitude gradually decreases towards the edge of the film whereas for the negative curvature, the amplitude increases towards the edge of the film. There was a flattened region observed towards the centre or the edges of the film, which is different from the theoretical predictions. This could be because of the assumptions considered in the theory, which is the neglect of the stretching energy involved in the wrinkling phenomenon [13, 14].

Also, this chapter explains the emergence of wrinkle patterns on thin curved shells and the concept of stable lines as an order parameter to predict the type and layout of these patterns. The literature predictions were verified in the patterns formed in the films used in this research. The theoretical predictions made in the literature regarding the direction of the paths at which a thin film wrinkle were also compared and verified with the experimental results for both positive and negative curvatures.

By elucidating the details of wrinkling patterns, dimensionless groups, wrinkle wavelength, and amplitude behaviour, this study paves the way for new opportunities in materials science, engineering, and related disciplines [81, 83, 84]. The knowledge acquired herein has the potential to transform various real-world applications, including smart materials, stretchable electronics, and innovative surface engineering techniques.

Chapter 5

Wrinkling patterns on photonic wafers

5.1 Introduction

Thin films are essential in electronics due to their ability to enhance device performance, enable miniaturisation, provide protection, facilitate optoelectronics and sensors, and enable the realisation of flexible electronic devices [160–163]. With unique properties and the ability to engineer and control them at nanoscale dimensions, thin films play a crucial role in the fabrication of semiconductor devices, such as transistors and solar cells [163, 164]. During the course of this project, Demosthenes Koutsogeorgis and Nikolaos Kalfagiannis, two researchers working on thin films at Nottingham Trent University, observed some wrinkling patterns on the surface of their silicon wafers when laser annealed. These instabilities looked similar to the wrinkling patterns formed on thin films, as given in Figure 5.1 (b) [16], and they brought this problem to our attention as an opportunity for collaborative research.

This chapter discusses the methods used for fabricating these thin films, including thermal

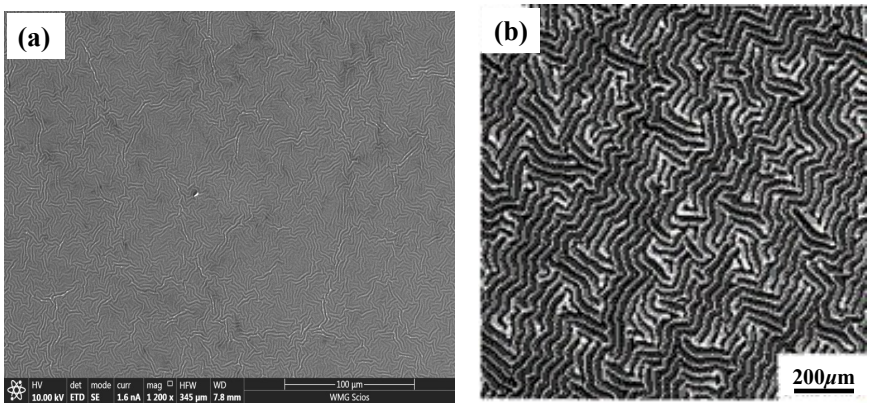

Figure 5.1: (a) Patterns observed on a 40 nm thick oxide layer on silica wafers observed under a scanning electron microscope and (b) patterns formed on PDMS films. Panel (b) adapted from [16].

oxidation, laser annealing treatments done on the silica wafer, and also the imaging technique atomic force microscopy (AFM) used to observe the pattern on the laser-treated wafers. The thermal oxidation and laser annealing treatments were done in Demosthenes lab by a master student Thomas Howe and by a visiting intern student Enora Kerautret involved in this project. This chapter also explains the analysis of the patterns observed and compares the characteristics and results with a theoretical model of heat transport during the annealing process, predicted by Nikolaos Kalfagiannis.

5.2 Methods: Preparation, imaging and analysis of patterned silicon wafers

5.2.1 Cleaving of silicon wafers

Silicon wafers are thin slices of pure single-crystal silicon that are commonly used as a substrate for microelectronic devices, and are also widely used in electronic devices [165–167]. Silicon in its pure form is an insulator but, when a small amount of impurities are mixed into a silicon crystal, called doping, it changes its behaviour into that of a conductor.

The wafer type which was used in this work was the n-type silicon wafer with a crystal orientation of $\langle 100 \rangle$, a thickness of approximately 500 µm, and a resistivity of 1-20 Ω cm. Cleaving is a process in which the wafer surface is scribed with a diamond scribe, after which the wafer is broken by hand, with the aid of a ruler. Here the wafer was placed on a neat cutting surface (A4 sheet of paper) and the diamond scribe was placed perpendicular at the centre of the straight edge of the wafer with a small force in order to initiate a fracture along the crystal plane. The wafer halves were divided into smaller pieces of width about 1 cm and a length of 4-5 cm in a similar way. In some cases, the wafer didn't break apart by cutting with the blade/scribe and in that case, the wafer was dropped onto the cutting surface from a height of 10 cm with the help of tweezers.

5.2.2 Thermal oxidation and measuring thickness

Oxidising silicon wafers involves a number of distinct procedures that use heat to produce a layer of silicon dioxide (SiO_2) or silica on top of the pure silicon [168]. Wet and dry oxidation are two general categories for thermal oxidation procedures. The selected procedure typically depends on the desired oxidation layer characteristics, particularly its thickness [169]. The dry oxidation method was used in this work, and it generates silicon dioxide when one silicon atom reacts with an oxygen molecule.

The cleaved silicon wafers were kept in a high-temperature oven (Carbolite CWF 12/13) for oxidation at a temperature of 1100°C. The thickness of the SiO_2 layer varies depending on the duration of the wafers in the oven. There was already a calibration curve generated by the group of Demosthenes Koutsogeorgis and also it can be calculated from online sites ([17]) as shown in Figure 5.2. It should be noted that a SiO_2 layer of roughly 2 nm in thickness develops naturally on the surface of a silicon wafer whenever the wafer comes into contact with the ambient air. Wafers with different SiO_2 thicknesses were made and in order to confirm the thickness of the SiO_2 layer, it was measured using the equipment called Filmetrics.

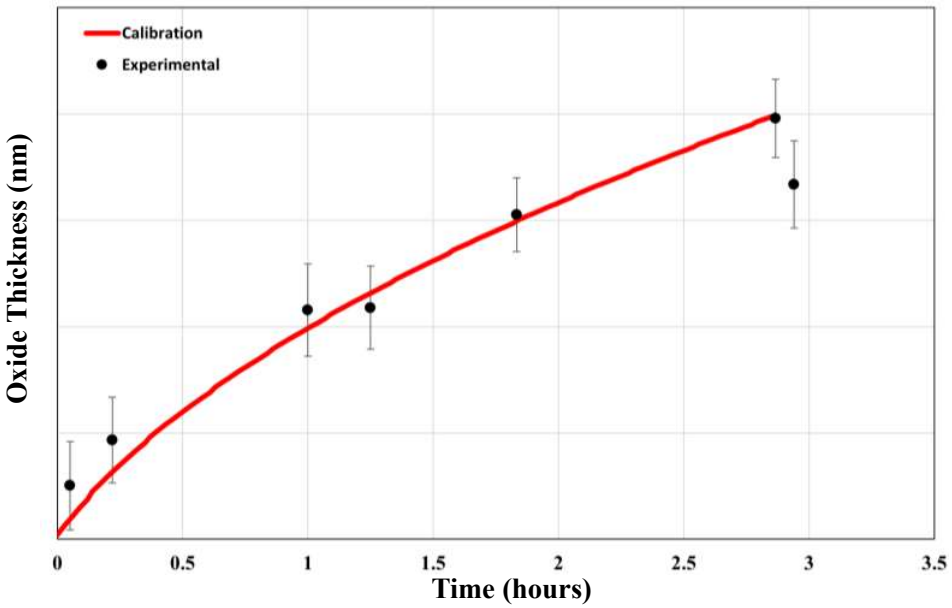

Figure 5.2: Oxide growth on a silicon wafer. The plot shows the expected (red) thickness of silicon dioxide grown on silicon wafers by the thermal oxidation process. The data is from the BYU online oxide growth calculator [17], assuming an initial oxide layer of 2 nm, an oven temperature of 1100 K and a crystal orientation of $\langle 100 \rangle$. The black data points are the experimental data generated during the thermal oxidation process.

The Filmetrics system operates by illuminating a sample using a tungsten-halogen white light source, covering a spectral range from 400 nm to 3000 nm, with an effective measurement span extending from 10 nm to 850 nm of thickness. To achieve this, the light was transmitted to the system via a fibre optic cable connected to the light source's output port. Subsequently, the light reflected by the sample was captured and directed back to the Filmetrics unit through another fibre optic cable, linked to the spectrometer input port. Within the system, the reflectivity spectrum of the sample was compared to an internally stored mathematical reflectivity spectrum corresponding to the specific sample under examination. Based on the pattern of reflected

intensity, covering conditions of constructive and destructive interference, a curve was calculated to best fit the measured reflectivity curve, enabling the determination of the corresponding thickness of the SiO_2 film at the position imaged. This thickness information was then noted down and repeated at different spots to ensure the reliability of values for the thickness of the oxide layer. The predicted and measured SiO_2 film thickness are shown in Figure 5.2.

5.2.3 Laser annealing

Laser annealing is a process used to modify the properties of thin films through the use of a high-energy laser beam. It involves irradiating the thin film with a pulsed laser beam, which causes localised heating and then rapid cooling of the material [18, 170, 171]. A schematic of a laser annealing process is shown in Figure 5.3 [18]. This process can lead to various changes in the film's structure, composition, and properties. A laser beam with a specific wavelength, intensity, and pulse duration is directed onto the thin film. The laser energy is absorbed by the film, leading to localised heating of the irradiated region. The absorbed laser energy can be sufficient to cause the thin film and some underlying silicon to melt within the irradiated area [171]. After the pulsing has finished the molten region solidifies rapidly, due to heat dissipation to the surrounding material and substrate. This rapid cooling can result in unique properties and microstructures in the film.

Laser annealing has been extensively studied and applied to silica-thin films to modify their properties [172, 173]. Silica, also known as silicon dioxide (SiO_2), is a common material used in

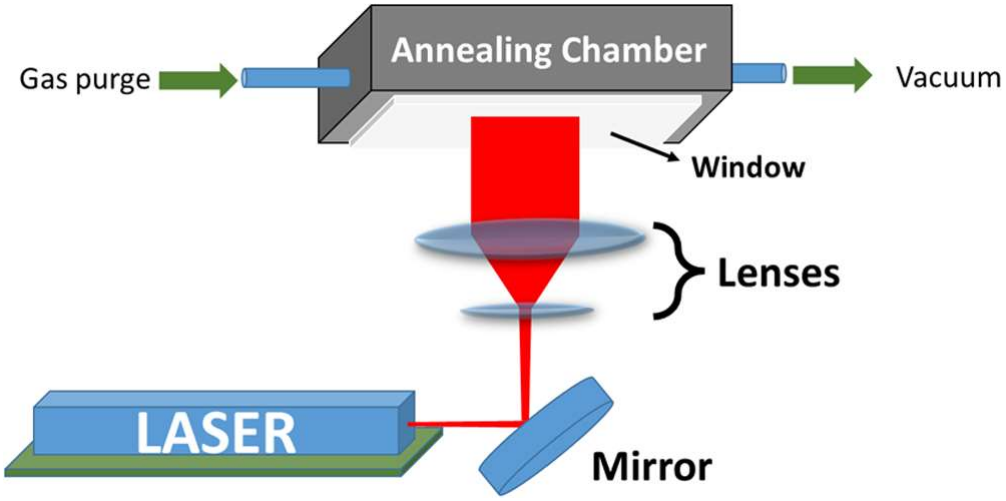

Figure 5.3: A schematic diagram of laser annealing. The figure is adapted from [18]. It should be noted that the laser used in this research was a laser with top-down pulsing.

various applications, including optics, electronics, and coatings. Laser annealing of silica thin films can bring about changes in their structure, refractive index, and optical properties [173]. Laser annealing has been shown to induce structural changes in silica-thin films. High-energy laser pulses can cause localised heating and rapid cooling, leading to the formation of non-equilibrium structures, such as nanocrystals or amorphous phases within the film. The degree of structural modification depends on laser parameters, such as energy density, pulse duration, and repetition rate.

In this research, silicon wafers underwent excimer laser annealing utilising specific equipment. The equipment setup consisted of a Krypton Fluoride (KrF) excimer laser, namely the Lambda Physik LPX 305i, which emitted unpolarised light pulses with a wavelength of 248 nm and a pulse duration of 25 ns. This apparatus was comprised of various components, including mirrors, a field lens, a mask stage, and a projection lens, all collaborating to deliver and shape the laser beam. The laser spot manifested in a square shape measuring 0.25 cm by 0.25 cm. Furthermore, an XYZ movable stage was employed to position and manipulate the samples during the various processing stages [174]. Prior to the annealing process, the laser pulse energy was calculated by assessing the fluence, which represents the ratio of the laser pulse energy to the effective focal spot area. In this research work, the fluence spanned from 250 mJ/cm^2 to 1500 mJ/cm^2, with increments of 250 mJ/cm^2.

5.2.4 Analysing surface patterns using AFM

To study the wrinkling patterns formed on the laser-annealed silica thin films on silicon wafers, the technique of atomic force microscopy (AFM) was used in this work. AFM can image almost all types of surfaces including polymers, ceramics, biological etc., unlike the scanning tunnelling microscope (STM) which can only image conducting and semiconducting samples or the scanning electron microscopy (SEM) from which the height profile can't be determined easily. There are different AFM techniques for different measurable force interactions like van der Waals, thermal, magnetic and electric forces.

The main part of an AFM is the AFM probe that scans across the surface of the sample. The probe used in this research was the RTESP-300 by Bruker. This probe consists of a sharp conical tip of radius ($\sim$ 10 nm) made of silicon attached to the end of a cantilever of length $\sim$ 125 µm. The probe is placed on a piezoelectric scanner which can move in all directions. The AFM operates in three different modes which are contact -mode, tapping mode, and non-contact mode.

In this project, tapping mode was used in order to avoid damage to the sample that might take

place with the contact mode. This process involves oscillating the cantilever vertically in the z-direction while simultaneously scanning across the surface of the sample. Typically, the oscillation frequency matches the inherent (resonant) frequency of the cantilever which was $f_0 = 300$ KHz, one line per second in this research. As the probe approaches the sample surface, its oscillation amplitude phase is altered. In the case of tapping mode, the amplitude was initially set as a reference point. To account for fluctuations in amplitude when the probe contacts the sample, it was adjusted vertically using a piezo mechanism until it returned to the preset amplitude level.

Before the scan, all preliminary adjustments like the alignment of the laser on the cantilever, alignment of the photodiode, laser signals, resonant frequency of the cantilever, etc. were checked using the AFM software. Also, the parameters like the set point, and scan rate, which means the speed at which the tip moves over the sample, etc. were also set before the measurements. The speed at which the tip moves over the sample is a very important parameter since if the tip moves very fast it won't track and trace the surface of the sample properly. In this work, the scanning area of the AFM probe was set to be either 30 µm or 60 µm, which was a tiny section of the 1.25 × 1.25 mm laser pulsed sample area. Scanning was done in four or five different areas of each sample. The height profile data was saved in a raw text format with the help of the Bruker software and used for the subsequent measurement of the pattern parameters.

For analysing the surface patterns for the data saved from AFM, the Gwyddion software and MATLAB were used. The tools used in the Gwyddion software are explained in the following section.

Processing of AFM data using Gywddion

Some of the tools in the Gwyddion software, which was used for processing the AFM data, are explained in this section.

When the raw images from the AFM were opened in Gwyddion, it was observed that the four corners of the images were not on the same level. This could be due to various reasons such as the sample not being at a flat level while doing the AFM, or it could lack levelling because of the various detection systems such as piezoscanner voltage, used in AFM scanning. Therefore, the first important tool which was used in this processing was the levelling. Different levelling tools were used in this project. The most commonly used levelling option was the plane levelling option, which was typically one of the initial processes performed on raw AFM data. Using the plane levelling tool, a best-fit plane was calculated from all the image points and then the plane was subtracted from the data. In some data, even after performing the plane levelling, all the image points were not at the same level, in that case, the three-level point levelling was used. Using this tool, three points that should be at the same level were selected for example at three

similar wave crest, and the software calculated a plane from the selected three points and the plane was subtracted from the original data.

The next important tool that was mostly used in this project is the background subtraction tool. Gwyddion offers various specialised modules for performing background subtraction. Each of these modules provides the capability to separate the subtracted background and extract it into a distinct data window. The most used background subtraction tool in this research was the Polynomial background. This background subtraction was employed to remove more complex and non-uniform background variations from an image. These variations may not be linear or easily corrected with a simple plane levelling. Instead of fitting a flat plane, polynomial background subtraction involves fitting a polynomial function (e.g., quadratic or higher-order polynomial) to the background of the image. Similarly to plane level, polynomial background subtraction can include or exclude the data under the mask.

During the imaging, in a few samples minor instances of scarring were observed. To identify scars, the software detects sharp contrasts and subsequently employs pixel interpolation from neighbouring rows to correct these artefacts. It's important to note that this correction step is not consistently necessary in all the images.

The tools mentioned above are not used in all the images, but used depending on how levelled, smooth and clear the patterns are after the scanning. The raw and the processed images of a sample is shown in Figure 5.4 (a) and (b) respectively. Once the images are processed, the data is saved in the text format in order to analyse the characteristics of the pattern using MATLAB. The detailed description of the analysis done using MATLAB is explained in the next section.

Analysis of AFM data using MATLAB

To analyse the characteristics of the pattern formed on the wafers, the algorithm of 2D fast Fourier transform (FFT2) was used with the help of MATLAB. This is a mathematical algorithm used to compute the discrete Fourier transform of a 2D input signal or image. The FFT2 is an extension of the 1D Fast Fourier Transform (FFT), and it efficiently calculates the frequency components present in the 2D signal. In the context of 2D signals or images, it helps to identify the spatial frequencies present in different directions (horizontal and vertical) within an image.

The spatial frequency or the wavenumber (k) of a wave or pattern describes how frequently it repeats occurs over a unit distance. In the context of spatial frequency analysis, the equation $k = 2\pi/\lambda$ relates the wavenumber (k) to the wavelength (λ) of the wave or pattern.

The processed height data from Gwyddion were exported as a 512-by-512 array. To carry out the processing in the MATLAB environment, the initial step involved importing this data that represented the heights of the wrinkled film's surface at different spatial positions. To enhance

the accuracy of subsequent analysis, the mean height value of the entire surface was subtracted from each data point. This operation effectively removed any baseline height, ensuring that the analysis concentrated solely on variations from this mean height. Following data preprocessing, a 2D fast Fourier transform was applied to the modified height data. The FFT is a powerful tool for converting spatial data into the frequency domain. In this case, it was particularly useful for analysing the spatial variations (wavelengths) present in the wrinkled film's surface. The 2D FFT was calculated by using a function `fft2` in MATLAB. Mathematically, the 2D Fourier transform is given by:

$$A(k_x, k_y) = \iint h(x, y) e^{-i(k_x x + k_y y)} dx dy, \tag{5.1}$$

where $A(k_x, k_y)$ is the Fourier amplitude at the wavenumbers k_x and k_y, corresponding to the x and y directions, respectively. Here also, $h(x, y)$ is the pre-processed height data in the spatial domain, and (x, y) represent the spatial coordinates.

The result of the FFT was a complex-valued matrix with information about the surface's spatial wavenumber components and corresponds to the discrete version of Equation 5.1. To extract meaningful insights from the FFT result, the power spectrum was calculated given by,

$$B(k_x, k_y) = |A(k_x, k_y)|^2. \tag{5.2}$$

The power spectrum represents how the power or intensity of height variations varies with different spatial wavenumbers across the film's surface. Then a radial average of the power spectrum was performed to obtain the spectral power (I) in terms of the absolute value of the wavenumber ($k = \sqrt{k_x^2 + k_y^2}$). The angular distribution of the power at specific spatial wavenumbers was particularly relevant to investigate the directional or angular variations in the surface profile. This is expressed by $I(k)$,

$$I(k) = \frac{1}{2\pi k} \int_0^{2\pi} B(k, \theta) d\theta. \tag{5.3}$$

The discrete version of this operation was computed on the Fourier data, and revealed the spectral power of the height variations at each spatial wavenumber component. High values in the power spectrum indicate strong variations in height at specific spatial wavenumbers, while low values indicate weak variations. This process involved dividing the 2D frequency space into radial bins with equal wavenumber increments. The result was a 1D vector of radial wavenumbers and the corresponding power for each wavenumber. This operation helps analyse the distribution of spatial frequencies in the input field and provides information about dominant and average wavenumbers. The spectrum was then normalised by dividing the power in each wavenumber bin by the total power. This provides a normalised distribution of spatial frequency power, allowing for meaningful comparisons between different samples. The dominant wavenumber

(k_{dom}) was then identified as the wavenumber corresponding to the peak with the highest power in the wavenumber domain, in other words, the mode of the power spectrum. A mean-averaged wavenumber ($\bar{k}$) was also defined from the power spectrum. Finally, a characteristic wavelength was calculated by the relation $\lambda = 2\pi/\bar{k}$.

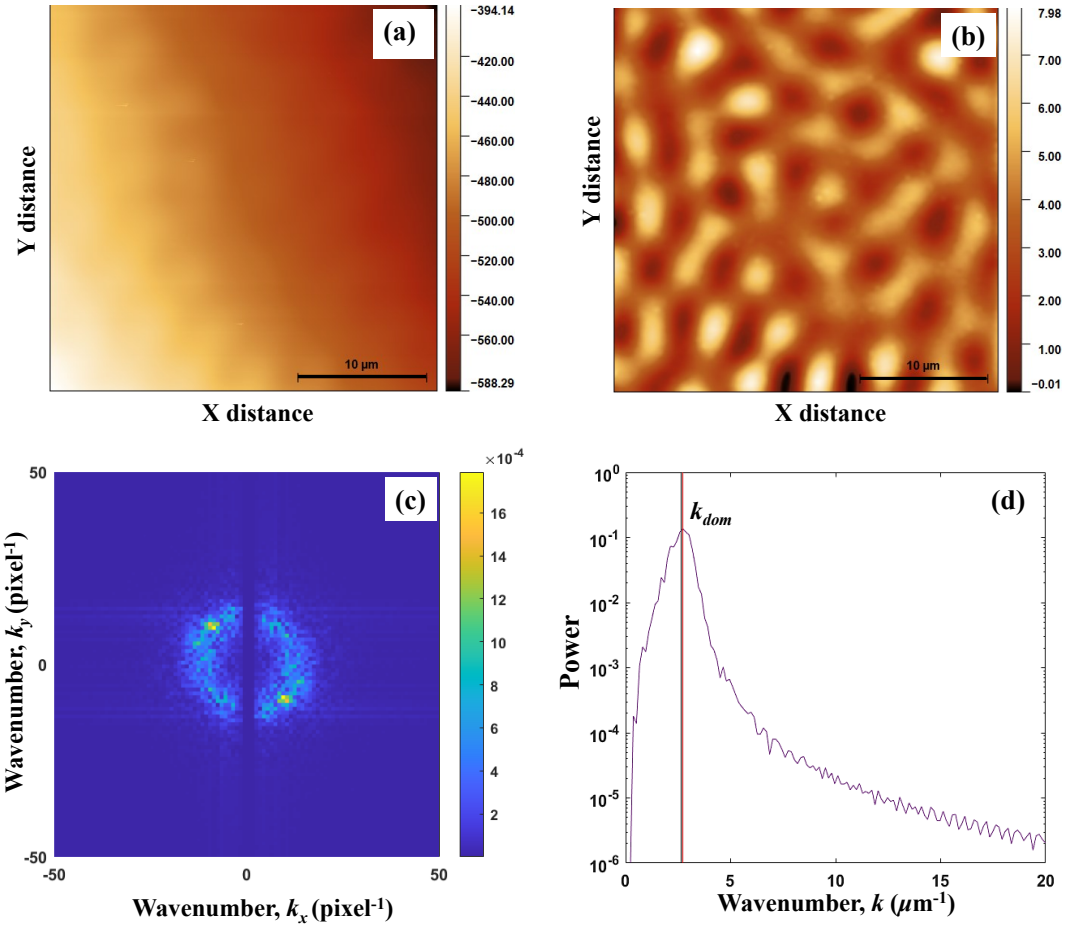

Figure 5.4: Steps involved in the analysis of AFM images. Panel (a) shows the AFM raw image when opened in the Gywddion software, (b) depicts the AFM image after performing levelling, removal of scars, background subtraction etc., (c) shows the plot of the 2D FFT, and (d) shows the power spectrum of the data, with the dominant wavenumber highlighted by a red line.

Figure 5.4 (d) illustrates the power spectrum where the x-y plane represents spatial wavenumbers ($k = 2\pi/\lambda$), and the z-axis corresponds to the power or intensity. Peaks in the power spectrum correspond to dominant spatial wavenumber components in the wrinkled pattern. The amplitude of the wrinkle pattern formed on samples was determined with the help of MATLAB. The function `rms` (Root-mean square) was used to determine the amplitude values for

the samples. Analysing these peaks provides valuable information about the surface's structural characteristics, such as the predominant wrinkle wavelengths and their amplitudes.

5.3 Results and discussion

This section discusses the results of the analysis for the processed silicon wafers along with the characteristics of the patterns formed on these substrates.

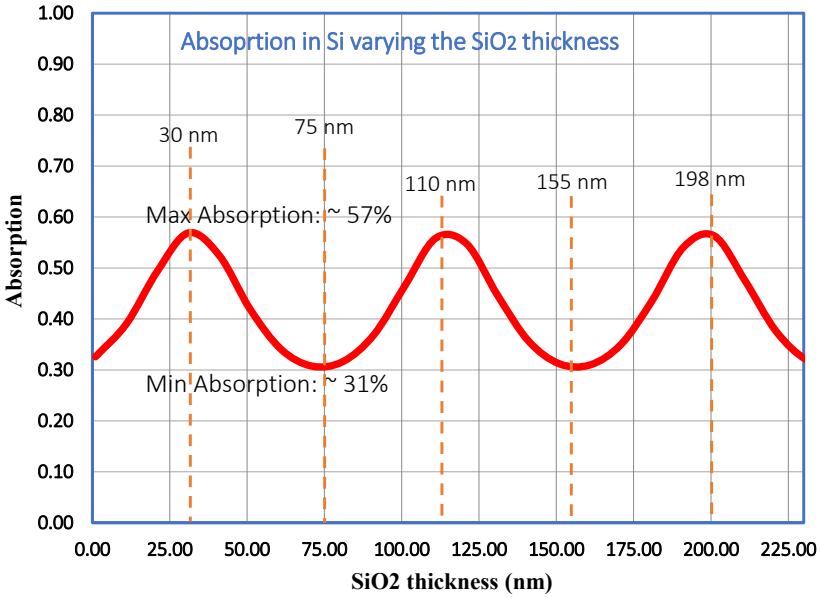

Figure 5.5: The variation of absorption at different thicknesses of oxide layer is shown in the figure. Tha maxima and minima absorption is related to the integer multiple of half wavelength ($\lambda/2n$) where λ is the wavelength of the laser and n is the refractive index of silica.

In the research conducted, multiple oxide thicknesses were aimed for, specifically 30 nm, 75 nm, 110 nm, 155 nm, and 198 nm. This choice of optimum oxide thickness for the experiment involved these thicknesses showing maximum and minimum absorption of the irradiated excimer laser during the annealing process, as shown in Figure 5.5. A specific wavelength of the excimer laser of 248 nm was used to compute the SiO_2 thicknesses with optimum absorption. The maximum and minimum absorption typically occurs when the sample thickness is close to an integer multiple of half the wavelength ($m\lambda/2n$), where λ is the wavelength of the incident light in free space, n is the refractive index of silicon and m is a positive integer.

Figure 5.6 shows the predicted results of the absorption of varying laser pulses of fluence, specifically 250 mJ/cm^2, 500 mJ/cm^2, 750 mJ/cm^2 and 1000 mJ/cm^2, on the temperature and state of a silicon wafer with a 30 nm SiO_2 coating. Similar results were obtained, in the

simulations performed by Nikolaos Kalfagiannis, for all the experimental conditions in this study. These show how the temperature in the film and wafer respond to the absorption of the laser light, and are informed by temperature-dependent material properties, like absorbance, specific heat, and thermal conductivity. Iso-lines of the achieved temperatures are clearly shown in Figure 5.6 (c) and (d) which also indicate the iso-thermal regions indicating solid-liquid phase change. The increase in the fluences can be related to effects like an increase in the maximum achieved temperatures and the extent of the melting depths.

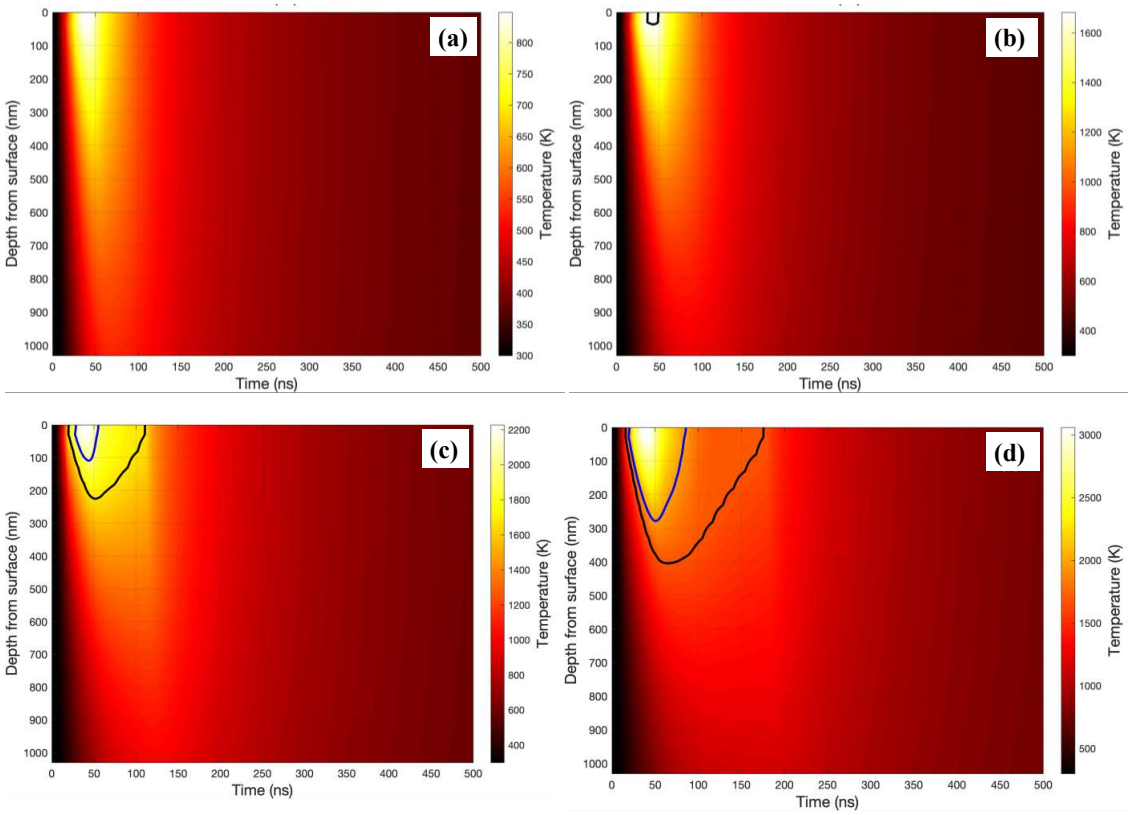

Figure 5.6: Snapshot of the numerical model of how the temperature varied over the sample. These images of the model are for an oxide layer of thickness 30nm. Black and navy blue lines show the expected depth of the solid-liquid transition i.e., they show the region of melting, for Si and SiO^2, respectively.

These two criteria, namely, the laser fluence and oxide thickness, were critical to the conducted experiments for analysing the wrinkle characteristics. For a specific oxide thickness, the irradiating laser induces an increase in sample temperature to certain depths beneath the sample's surface. This temperature elevation generates mechanical stresses within the sample

materials, specifically Si and SiO_2. If the achieved temperatures remain below the melting point of Si (i.e., 1683 K), both layers expand on heating, but then revert to their original states upon cooling. However, higher temperatures can lead to the melting of the Si layer, or both the Si and SiO_2 layers, depending on the attained temperature. Silicon has a melting temperature of 1683 K, while SiO_2 melts at 1986 K. Melting of either layer can induce a mismatch of strain on cooling, as the molten layer will rapidly relax any stresses within it. For example, if a thin layer of silicon is melted, when this layer solidifies again, the interface between it and the SiO_2 will be in a stress-free state, but still at elevated temperatures. As the system cools, the layers will shrink at different rates, leading to a residual stress at room temperature. The extent of this disparity arises from the difference in the thermal expansion coefficients of the two layers, with Si having a coefficient of 2.6×10^{-6} K^{-1} and SiO_2 having a coefficient of 0.55×10^{-6} K^{-1} (typical values at room temperature). As a consequence, the previously melted Si layer will exert a compressive stress along the interface, which can result in the buckling of the upper SiO_2 layer.

The experiments were conducted for different oxide layer thicknesses and laser fluence and the observed results were analysed. After performing the processing steps discussed in section 5.2.4, the patterns observed on different samples of various thicknesses were plotted in an array format to visualise the varying topography.

Figure 5.7 shows the individual wrinkle topographies with clearer wrinkling phenomena observed at smaller values of oxide thickness, i.e., with higher amplitudes and smaller wavelengths. This can be related to the fact that thinner oxide layers allow for higher temperatures, deeper melted layers and more residual stresses during the laser annealing process, causing more driving forces for buckling.

Figure 5.8 shows the array plot, but with a common colour scale, to visually observe how the wrinkle height profiles (amplitude) change with respect to the oxide thickness and fluence.

A key parameter of interest is the maximum temperature reached during this process, as it has a direct impact on whether or not the layers undergo melting and, subsequently, the formation of patterns. It should be highlighted that it is the thickness of the melted layer that acts as the driving force for buckling. The strain energy available per unit surface area, which is required for buckling, can be computed as a product of the stress mismatch across the layer interfaces, and the melting thickness. The melting temperatures of silicon and silicon dioxide are crucial reference points, with silicon melting at 1683 K and silicon dioxide at 1983 K. When the maximum temperature remains below the melting point of silicon (1683 K), neither of the layers experiences melting and as a result, no patterns are formed, as illustrated in Figure 5.8 (Region C). In the scenario where the maximum temperature surpasses the melting point of silicon (1683 K), but still falls short of the melting point of silicon dioxide (1983 K), only the silicon layer

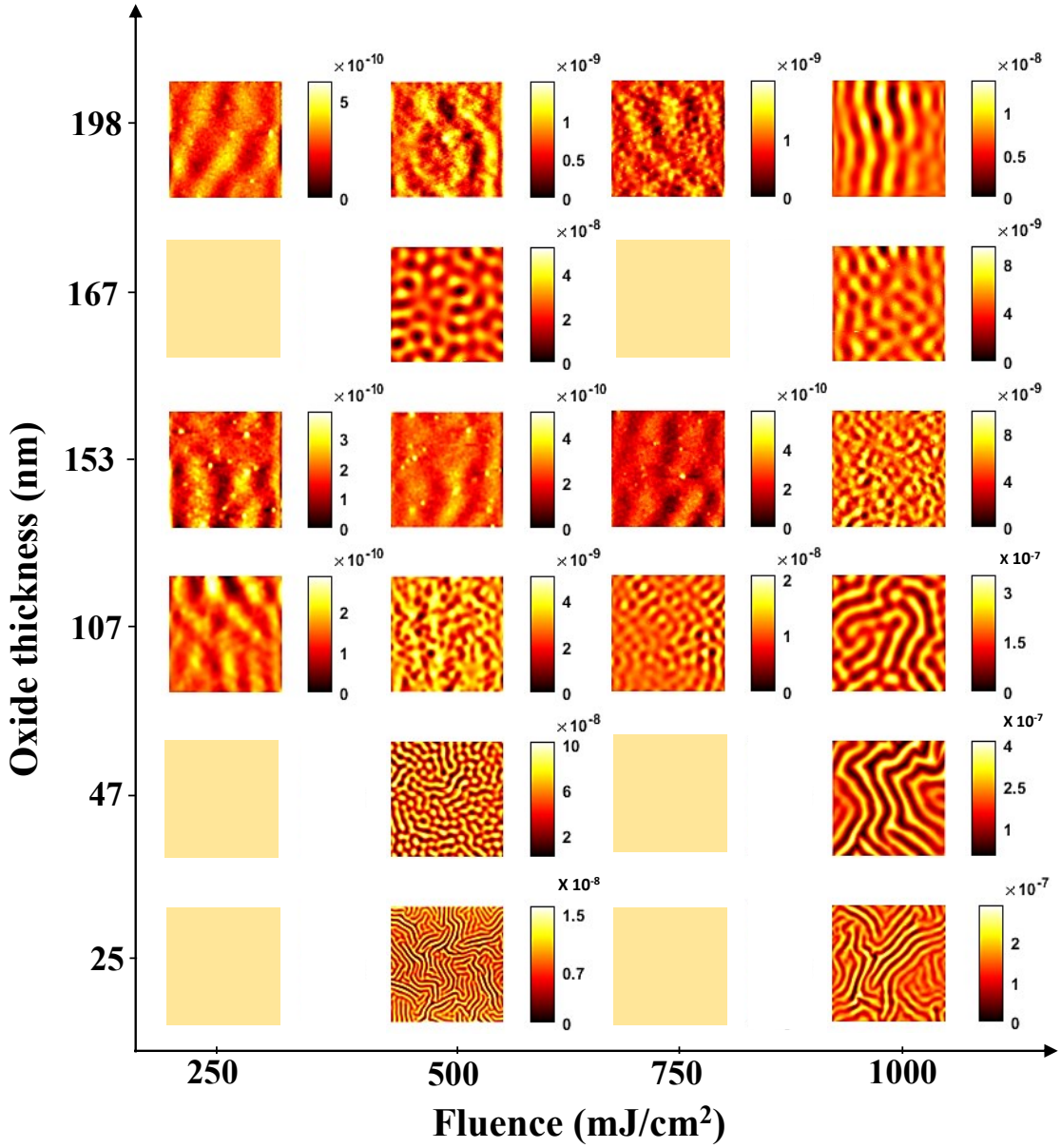

Figure 5.7: Individual plots of heights (in m) of samples having different oxide thickness when laser annealed at different fluences. These are the data after performing the processing like levelling, removal of scares etc. in Gwyddion software. The yellow empty boxes represent data which are not available.

undergoes melting. As a consequence, the subsequent cooling of the melted layer of silicon imparts a mechanical stresses on the interface of the two layers, which can lead to the formation of some wrinkles as shown in Figure 5.8 (Region B). In the case where both Si and SiO_2 melt, the situation will be more complex, but the additional relaxation of stresses in the melted SiO_2

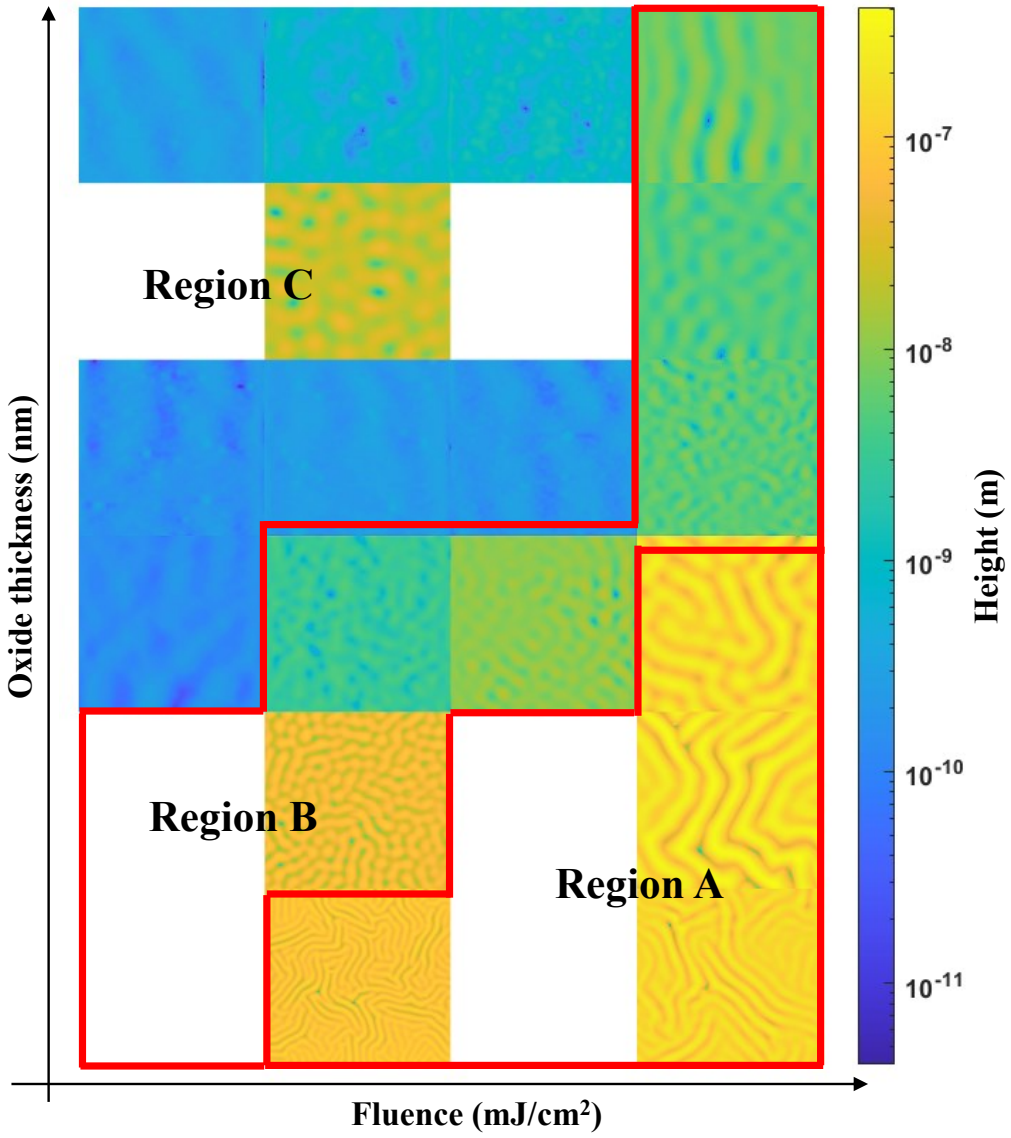

Figure 5.8: Plot showing the array of wrinkle height profiles with all the data shown in Figure 5.7 represented in a common colour scale. The matrix plot is divided into Three regions: Region A shows patterns formed in the samples in which the maximum temperature attained is above the melting point of silicon and silica, Region B shows the patterns when the silicon layer melts and Region C shows the samples in which both the layers didn't melt.

layer should cause a discontinuity in the response of the system. Figure 5.8 (Region A) shows the formation of wrinkles when both the Si and SiO_2 layers are melted and re-solidified. This scenario is associated with the clearest wrinkle pattern, due to the stress differences accumulated as the various layers cool from a molten state, as well as the generally higher thickness of the melted silicon layer driving the pattern, in these cases. The reliability of these findings is underscored

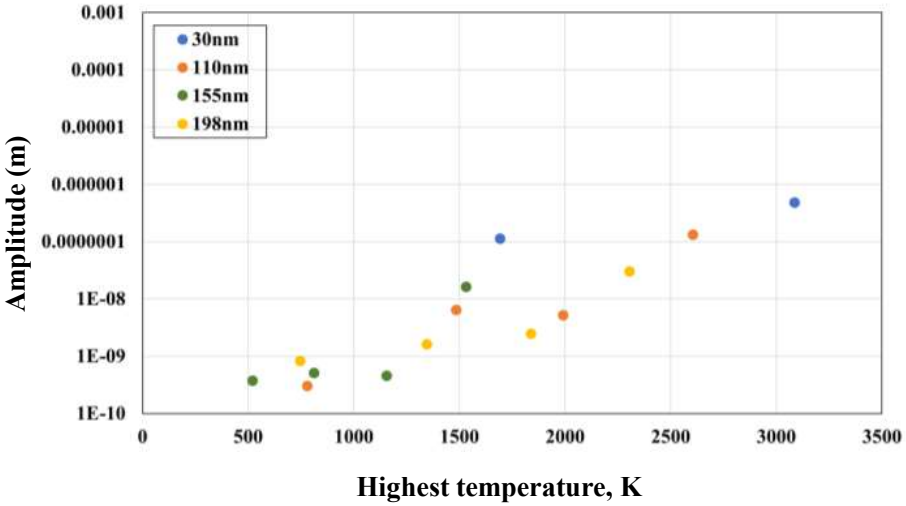

Figure 5.9: Illustration of the amplitudes of the patterns formed on the silicon wafers during the laser annealing process. The RMS value of the amplitude for the patterns in different samples is plotted against the maximum temperature which was determined from numerical simulation. samples of different oxide thickness is represented by different colours in the plot.

by the observed colour gradient in the plot, indicating a gradual rise in wrinkle heights as the laser fluence increases and the oxide layer thickness decreases. Increasing the laser fluence and reducing the oxide layer thickness leads to a higher overall temperature reached, and the influence of this temperature rise on wrinkle amplitude can be observed in Figure 5.9. Effectively, this is the result of an increased available strain energy, due to a thicker melted layer.

Utilising Equation 4.8, the associated effective strains for all the samples, $\epsilon = \pi^2 A^2/\lambda^2$, can be calculated. As depicted in Figure 5.10, the plot reveals a direct relationship between these strain values and the temperatures achieved. Notably, the plot highlights an increase in observed strains as temperatures rise.

This plot also shows some intriguing insights, particularly at the crucial melting temperatures of Si and SiO_2, shedding light on the previously discussed strain mismatch during the cooling phase. It's worth noting that this research is currently a work in progress, involving collaboration with other research groups, aimed at gaining a deeper understanding of these effects. Furthermore, there is a continued focus on enhancing the modelling aspect of the study. This endeavour aims to provide a more comprehensive understanding of how laser fluence influences the maximum temperature obtained and its impact on accurately determining the sample's melting depths when subjected to small laser pulses. As this aspect of the work develops, it will provide more sophisticated means of analysing and predicting the emergent wrinkle patterns.

Additionally, further focus will need to be given to the calculation of the effective strain

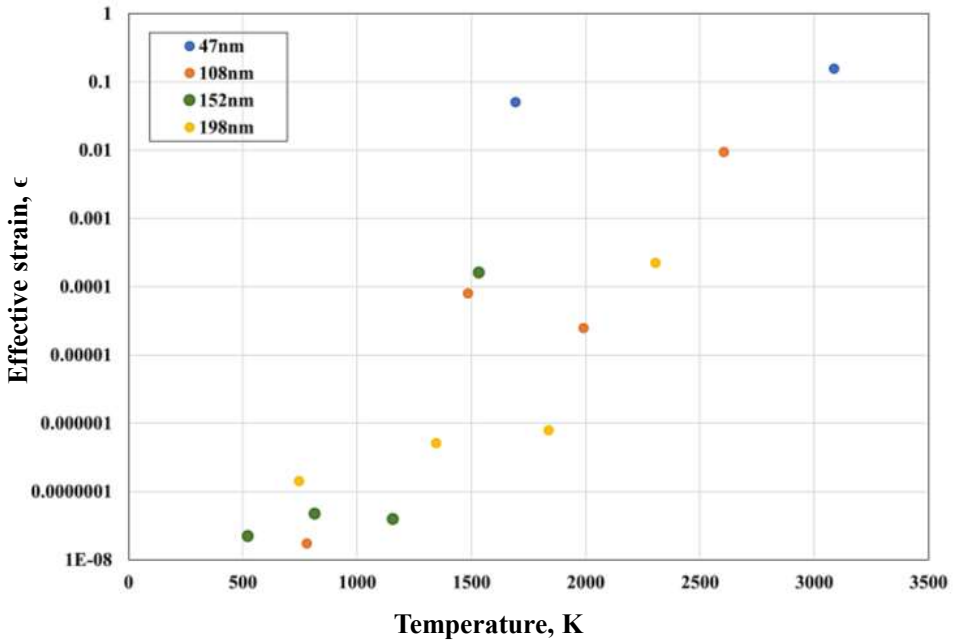

Figure 5.10: Plot showing how the effective strain varies for different maximum temperatures attained by the sample during laser pulsing. Data of different colours represent samples with different oxide thicknesses.

generated during the expansion of both layers. This calculation is pivotal as it will bolster the research's predictive capacity, particularly in terms of amplitude and wavelength variations under different conditions, such as varying oxide thicknesses and fluence levels. These endeavours will aim to fortify the reliability and robustness of the research findings.

5.4 Conclusions

To summarise, this chapter discussed the patterns observed in the photonic wafers during the laser processing of thin films. The wafer which was used in this research was a silicon wafer and its oxide layer. A detailed description of all the methods used in preparation of the samples is included in this chapter. The laser-annealed samples were observed under the atomic force microscope to study the patterns formed on the surface. Moreover, the chapter outlines the subsequent steps of processing and analysis applied to these surface patterns. The processing and analysis of these patterns were done using Gwyddion and MATLAB.

In this study, we collaborated with a research group to develop a numerical model. This model assisted in determining two critical factors: the highest temperature reached during our experiment and the thickness of the layers that melted. These findings were instrumental in

elucidating the reasons behind the observed surface patterns.

It was observed that, when the sample's temperature during laser pulsing exceeded the melting points of the silicon and silica layers, it caused both layers to briefly transition into a liquid state. This allowed a relaxation of the thermal stresses accumulated in the layers due to heating from room temperature, which in turn allowed for residual stresses to build up as the once-molten layers cooled back down to ambient conditions. This insight provides a clear explanation for the appearance of the observed surface patterns. Our study contributes to a deeper comprehension of the intricate interplay between temperature, material characteristics, and surface pattern formation. The research remains a work in progress, with further steps planned for advancement. To enhance the accuracy of the numerical model, efforts are underway to refine the step size used in calculations, ultimately allowing for more precise measurements of the thickness of the melted layer.

Chapter 6

Hydrogel swelling and patterns

6.1 Introduction

Swelling is a fundamental process with widespread significance across diverse fields, including biology, engineering, and earth sciences [175–177]. At its core, swelling involves the expansion of a material's volume, for example as it absorbs additional fluid within a porous structure. Swelling in polymer materials happens when liquid diffuses into them, making them change in size or volume [178, 179]. This phenomenon is encountered in a variety of real-world scenarios, each with its unique implications.

In the realm of biology, swelling plays a pivotal role in the healing process and inflammation response. When injured, tissue swells as cells and tissues absorb extra fluid [180–182]. This natural biological mechanism aids in protecting and repairing damaged areas. Similarly, wooden structures can expand when exposed to high humidity levels. This expansion can affect the structural integrity and longevity of wooden constructions, making it essential to account for swelling properties in architectural and woodworking applications [183, 184]. The interaction between a porous material's structure and the changing fluid distribution makes swelling a dynamic and poromechanical process [185].

When materials absorb liquid or swell, it can lead to mechanical instabilities in both natural and man-made substances. In nature, we see examples like pine cones opening and closing due to changes in the shape of their scales caused by swelling [186]. Another example is articular cartilage, which can stretch, bend, and curl when it swells [187]. In synthetic materials, when they soak up a solvent and swell, they can buckle, wrinkle, or even separate into layers [188]. Thin polymer films, for instance, may bend as they swell [189]. This swelling effect is also the basis for things like artificial muscles, wearable electronics, and soft robots, where soft and flexible polymer materials expand and contract because of the solvent they absorb [175, 190].

Hydrogels are three-dimensional structures made of polymer chains with a unique arrangement that can absorb a lot of water [191–193]. Unlike some other materials, they don't usually dissolve because of the way their molecules are linked together chemically or physically, or because their long chains of molecules get tangled up [191]. Hydrogels can be found in nature as

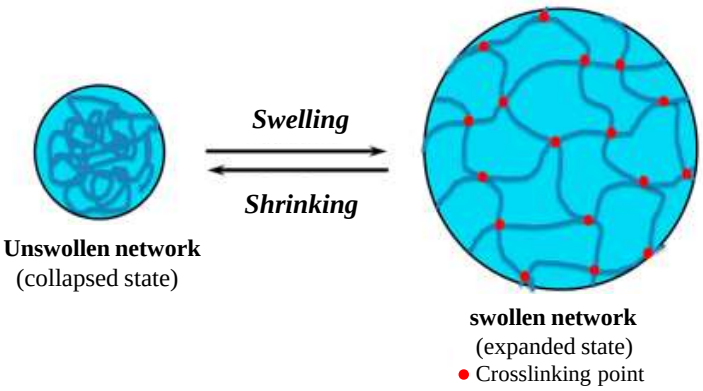

Figure 6.1: Swelling and shrinking of hydrogel. The diagram shows the structure of a dried hydrogel and the structure of a swollen hydrogel with crosslinking points. Adapted from [19].

polymer networks, like collagen or gelatin [194, 195], or they can be created artificially. One can imagine them as tiny sponges made of a three-dimensional mesh that can soak up water and hold onto it as shown in Figure 6.1. This ability to hold water makes them useful in various applications, from medical uses like wound dressings to creating soft contact lenses [115,196–198].

Nearly twenty years ago, a group of scientists led by Tanaka made a discovery about how acrylamide hydrogels change when they're placed on a flat surface and absorb water [199–201]. They noticed that interesting patterns formed on the surface of the hydrogel as in Figure 6.2. This pattern was explained by a competition between two things: the osmotic pressure from the absorbed water and the constraints from being confined within the gel. Even though the gel was originally evenly connected, because it was stuck on a hard flat surface, only the top layer could expand freely. This created a kind of osmotic pressure difference between the edge and the bottom of the hydrogel layer. Similarly, another work was done on hydrogel beads, where it was discovered that on the swelling of the bead, the rapid expansion of the outer area is restrained due to its connection to the less expanded core, resulting in significant tensile stress radiating outward in the outer region. This stress gradually diminishes as the swelling progresses towards the centre. As time passed and the gel absorbed more water and reached its equilibrium state. This is similar to misfit in strain which was discussed in the previous chapters. However, these patterns are not permanent, they disappear when they reach an equilibrium state during the swelling and drying of the hydrogels.

Much research has been focused on manipulating elastic instabilities caused by swelling in elastomeric films to create intricate patterns [109, 140, 202]. One of the example is illustrated in Figure 6.2. However, there has been limited work done in the deliberate control of pattern formation and arrangement in hydrogel films recently [109, 199, 203, 204].In the case of a soft

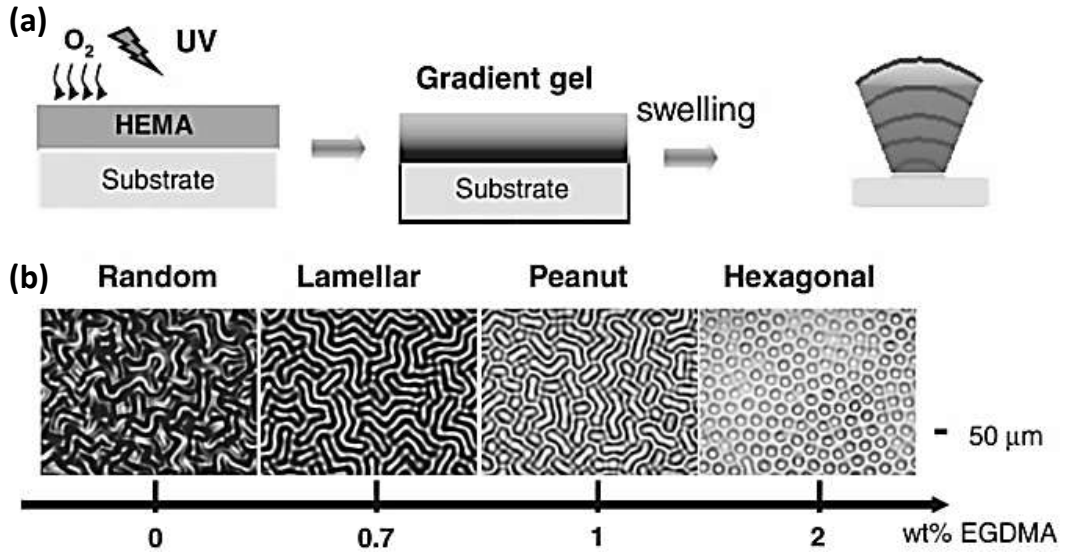

Figure 6.2: (a) diagram depicting how poly-hydroxyethyl methacrylate (PHEMA) films are made with varying stiffness and they develop wrinkled patterns when they absorb water. (b) As the films become stiffened by the addition of a crosslinker, EGDMS the structures of the patterns that form on the surfaces of these water-swollen PHEMA films change. Adapted from [20, 21].

elastomer featuring a thin rigid outer layer, the application of relatively minor compressive stresses results in the emergence of surface patterns [16, 205, 206]. However, when it comes to hydrogels, the instabilities induced by swelling stem from the confinement of the highly swollen film to a substrate. Consequently, this confinement gives rise to anisotropic osmotic pressure and relatively higher compressive stresses. Therefore, factors such as film modulus, strain level, cross-linking density, and homogeneity within the film, as well as film thickness, may also prove to be pivotal in the control of pattern morphology and characteristic size.

In addition to changes in the periodic patterns on the hyrdogel surface, the development of wrinkles and folds on the surfaces of hydrogel structures was also observed [20]. These irregularities or instabilities in the surface can be harnessed to advance various engineering and medical applications [207–209]. For instance, the wrinkling of hydrogels can be intentionally used to create tiny mechanical components, like micro gears. It can also be employed in the production of multi-cellular clusters, such as spheroids, which have applications in biological research [210]. Moreover, these surface instabilities can be controlled to influence how cells spread, which is useful in various biomedical contexts. Additionally, there have been recent experiments demonstrating the creation of nano-scale wrinkled structures using laser-based assembly techniques [211]. These innovations open up new avenues for manipulating hydrogel structures for a wide range of applications.

In this chapter, I will be describing different exploratory experiments that were performed in order to understand how the effect of curvature affects the patterns and the wrinkles formed during the swelling phenomenon on thin curved hydrogel films. As an initial trial, I explored the swelling in gelatin. Later experiments were performed on hydrogels beads, because of their high elastic nature and swelling capacity compared to gelatin. Patterns formed on hydrogel beads motivated for the synthesis of hydrogel which is also included in this following sections along with their patterns on the surface. In the following sections, the results of different swelling studies performed during this project will be discussed.

6.2 Swelling study using gelatin

Gelatin is a large protein molecule derived from collagen [212]. Its high molecular weight makes it a valuable material for gelatin films. These particles can have a wide range of applications in various industries, such as pharmaceuticals and food production [213–215]. One of the key attributes of gelatin is its biocompatibility [216]. This means that it can be safely used in biological systems without causing harm or adverse reactions. This property is particularly important when considering applications involving interactions with living organisms. Furthermore, gelatin exhibits bioadhesive properties, which means it can adhere or stick to biological surfaces [213, 217]. This characteristic is highly advantageous in medical and pharmaceutical contexts where substances need to remain in contact with specific tissues or cells.

The swelling behaviour of gelatin can vary significantly at different pH levels. Gelatin is a protein-based polymer, and its behaviour is influenced by the ionisation state of its functional groups (such as amino and carboxyl groups) as well as the charge distribution on its molecular structure [218]. According to the literature [219], at lower pH values (acidic conditions), gelatin tends to be positively charged due to the protonation of its amino groups. In this state, gelatin molecules repel each other because of their positive charges, leading to increased solubility and swelling. Therefore, gelatin exhibits the most significant swelling in acidic conditions due to increased electrostatic repulsion between molecules [220]. At neutral pH, the swelling behaviour is less pronounced, and in alkaline conditions, the swelling tends to be reduced as the molecules become less soluble and experience increased intermolecular attraction.

For the experiments presented here, gelatin solutions with different concentrations of gelatin powder were made. This was done by dissolving 10, 15, 20 and 30 grams of gelatin powder in 100 mL of deionised water at 60°C with mild agitation using a magnetic stirrer for 1 hour. Once the added gelatin powder was fully dissolved, the solution was transferred to a rectangular container and was allowed to cool down and cure at room temperature. Then the cured gelatin was cut into

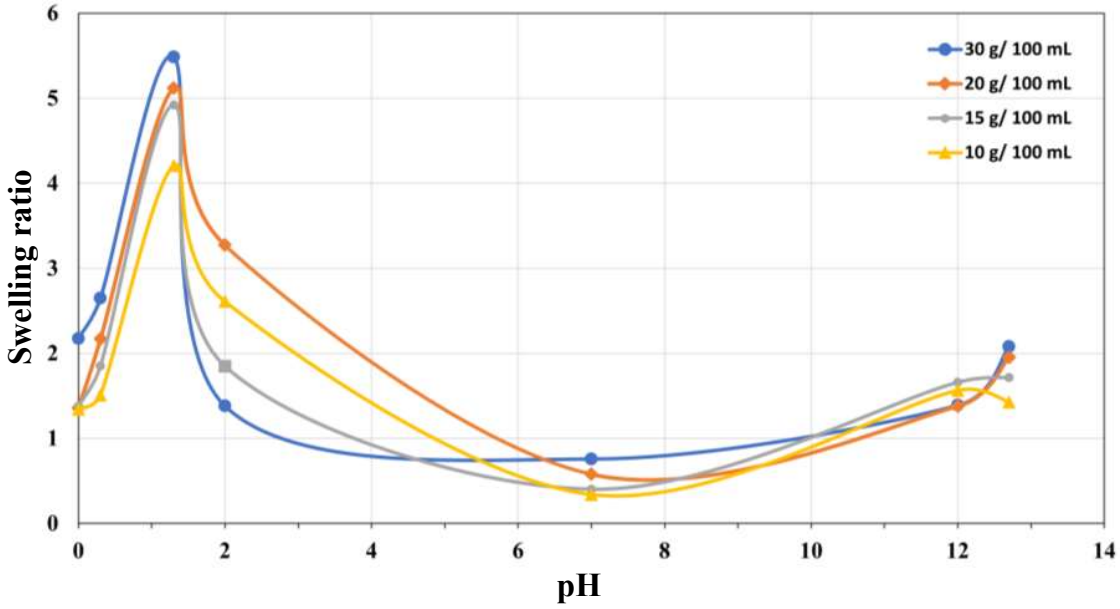

Figure 6.3: Variation of swelling ratio for different pH. The image shows how the swelling ratio of gelatin varies with pH. The experiment was repeated for different concentrations of gelatin.

small cubes and weighed for the swelling study. Different concentrations (different molarity) of salt solution were made using sodium hydroxide (NaOH) and hydrochloric acid (HCl) whose pH ranged from 0-13. The gelatin cubes were placed in the salt solutions having different molarities and allowed to swell fully by keeping them for 3 days. Once the gelatine cubes were fully swollen the weight of the gelatin cubes was measured and the swelling ratios were calculated. The swelling ratio of polymers here refers to the fractional increase in the weight of the hydrogel due to water absorption [221]. This ratio is often expressed as the change in the polymer's weight before and after swelling and is used to characterise a polymer's ability to absorb or retain fluids [221]. The swelling ratio of the gelatin cubes for different gelatin concentrations was measured and plotted against the pH in figure 6.3.

The gelatin solution was prepared and subsequently utilised for the fabrication of thin curved films by employing saddle-shaped 3D printed moulds as mentioned in Chapter 3. Following the casting process, the solution was allowed to undergo drying and curing. These gelatin films, synthesised via this methodology, were employed for the investigation of wrinkle patterns. However, it was observed that these films possessed a thin and brittle nature after the curing process. Moreover, in contrast to PDMS material, the thickness of these gelatin films could not be precisely controlled to meet our specific requirements. This limitation arose because, upon casting one layer and allowing it to dry, the application of another layer of the gelatin solution would

negatively affect the integrity of the preceding layer due to the influence of solution temperature. Because of these limitations, a more efficient material was thought of for further studies. The polyacrylamide hydrogels, which have a higher swelling capacity compared to gelatin were decided to be used further in this study. A detailed description of polyacrylamide and the swelling study with polyacrylamide is given in the following sections.

6.3 Swelling study using hydrogel

Polyacrylamide

Hydrogel beads, also known as polyacrylamide beads are tiny, squishy balls made of a special kind of material that can hold a lot of water. They look like little jelly balls, which are available in different colours. One might find them in gardens, where they help keep plants hydrated by releasing water slowly. They're also used in some diapers to keep babies dry and comfortable. Some scientists also use hydrogel beads in labs because they can soak up liquids and release them when needed. The colourful beads available commercially are made of polyacrylamide, known as poly (2-propenamide) or poly (1-carbamoyl ethylene), which is a polymer made up of acrylamide units that can be easily interconnected [222].

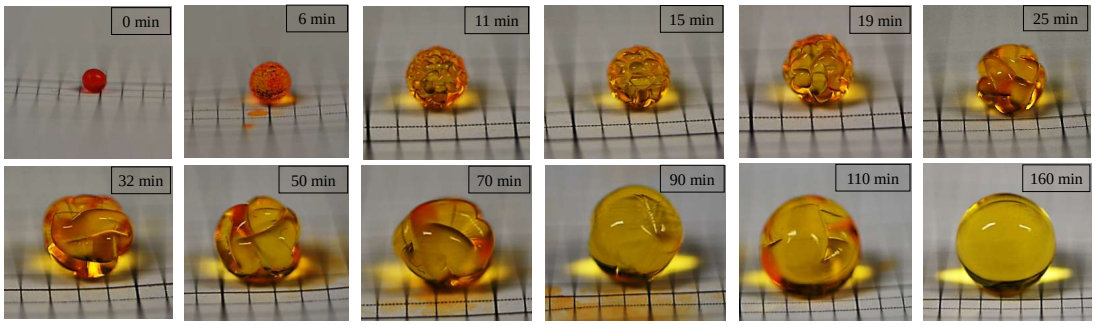

Figure 6.4: Swelling of hydrogel beads. Photographs of a swelling hydrogel at different times of swelling, as indicated, where the initial radius is 0.5 mm and the final radius is 5 mm. The grid lines are 1 mm apart.

As an initial trial, the commercially available hydrogel beads (orange in colour) were bought. These beads were placed on a graph sheet to measure the diameter of the swelling hydrogel beads. Once the diameter of the dried bead was measured, they were placed in deionised water and the diameter and patterns formed on the surface were measured and captured using a digital camera. Detailed visual representations of these hydrogel beads at various stages of their swelling process

can be observed in Figure 6.4, providing insights into the dynamic patterns that emerged on the bead surfaces during the swelling phenomenon.

In order to study the effect of the pH of the water in which the beads swell, these hydrogel beads were allowed to swell in different pH conditions. The diameters of the beads during the swelling process were measured using a graph sheet by taking out the beads from the solution. Figure 6.5 shows the swelling of the beads over time for different pH (3,6.5,8.5,11). From the plot, it was observed that the hydrogel beads, when dispersed in solutions of lower pH (3) reach their equilibrium state (fully swollen state) much faster than the other higher pH.

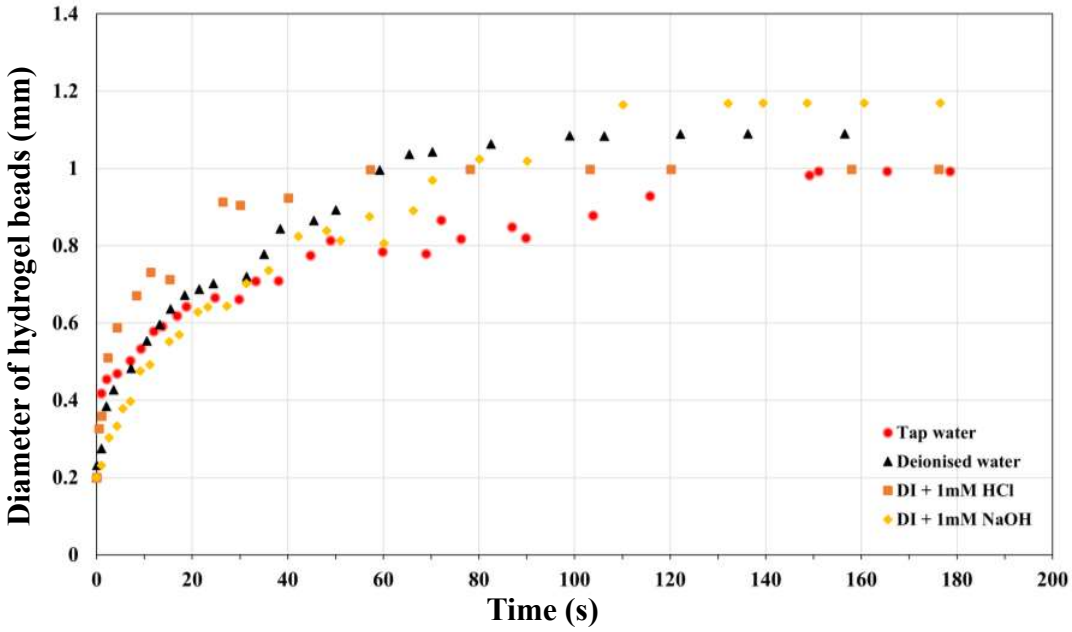

Figure 6.5: Swelling of hydrogel beads in different pH. The plot shows the increment in the diameter of the beads during the swelling over time.

More attention and detailed study were required on the patterns formed on the beads during the swelling. Based on the above results it was decided to synthesise the hydrogels directly, which enabled casting the hydrogel on the moulds having different curvatures and different swelling conditions. This could also help in understanding whether the curvature of the mould also affects the patterns formed on the surface during the swelling process.

Hydrogel synthesis

To create hydrogels, three main components are required: monomers, crosslinkers, and initiators. Monomers serve as the building blocks for the polymer. In the context of hydrogel synthesis, monomers like acrylamide are polymerised to form long chains. The polymerisation of acrylamide

begins with the initiation step, where a radical initiator (e.g., ammonium persulfate or other similar compounds) breaks the C=C double bond in acrylamide, creating two highly reactive sites known as free radicals. When free radicals are generated, they initiate a reaction by binding to the monomers, causing them to link together and form the polymer's main chain [223, 224]. Crosslinkers are molecules that contain multiple reactive sites, such as double bonds or functional groups. They play a critical role in connecting the polymer chains in a three-dimensional network [223]. This network structure is characteristic of hydrogels and imparts their unique properties, such as the ability to absorb water while maintaining their structural integrity. Initiators are compounds that stimulate the polymerisation process by generating free radicals. Free radicals are highly reactive species with unpaired electrons. In free radical polymerisation, initiators break down into free radicals when exposed to the appropriate conditions, such as heat or light. These free radicals then initiate the reaction by binding to monomers, creating new free radicals in the process [223]. This reaction continues until the monomers are consumed or until terminated by other reactions. Dilutents like water are often used to control the heat generated during the reaction. This controlled synthesis process enables the production of hydrogels with varying properties, making them suitable for a wide range of applications in science and industry.

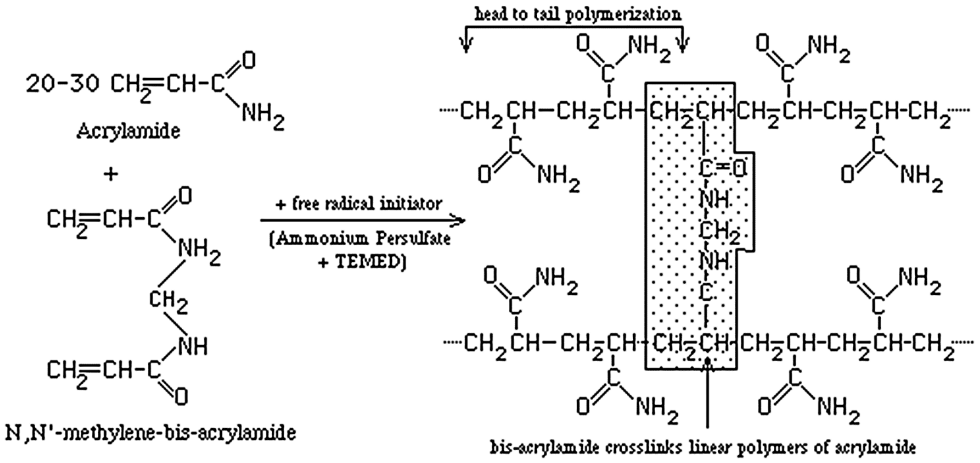

Figure 6.6: Illustration of the polymerisation reaction of acrylamide forming the polyacrylamide hydrogel. Adapted from [22].

There are several methods for cross-linking hydrogels [224,225]. Firstly, polymeric chains can be linked through chemical reactions as described above. Alternatively, ionising radiation can be employed to generate free radicals, which, upon recombination, form cross-links within the hydrogel structure [224]. Additionally, cross-links can be formed through mechanisms such as entanglements, electrostatic interactions, and crystalline formations. But mostly, polyacrylamide

hydrogels are synthesised using a technique called free radical polymerisation [226] as sketched in Figure 6.6. These hydrogels are composed of a covalent polymer network mixed with water. Typically, the molar ratio of the monomer to the crosslinker falls within the range of 10 to 10^4, while the volume fraction of water can vary between 70% and 90%. Under normal conditions, the polyacrylamide network remains stable, allowing water to move within the polymer structure.

The synthesis of polyacrylamide hydrogels involves several materials and steps. In this project, the protocol given by Nishi et al. was followed [224]. The necessary materials for this process include acrylamide (AAm), acrylic acid (AAc), N, N, N', N'-Tetramethylene ethylene diamine (TEMED), potassium peroxodisulfate (KPS), N, N'-methylene bis(acrylamide) (MBA), methanol, and distilled water. To initiate the synthesis, 5 g of acrylamide is dissolved in 100 mL of deionised water, forming a solution. Subsequently, 1 mL of the activator, TEMED, is introduced into the solution, and the mixture is allowed to stir for 20 minutes using a stir bar and hotplate. It's crucial to maintain a constant temperature of 60°C throughout the reaction. Following this initial phase, 0.5 grams of acrylic acid and MBA, which serve as the cross-linking agent, are gradually added to the stirring solution in the beaker [224]. After 30 minutes, the initiator, KPS (0.1 g in 10 mL distilled water), is introduced drop by drop into the mixture. This controlled addition of the initiator leads to the formation of a highly viscous and translucent gel.

Depending on the quantity of KPS and TEMED, the time required for the solution to transform into a gel is determined. A few moulds in different shapes were used to try this. The solution was transferred into different moulds and slowly the initiator KPS was added drop by drop. After becoming the gel, it was submerged in methanol, in in order to dehydrate the gel and was dried after that. The dried hydrogel was then dispersed in water to study the swelling behaviour. The patterns formed on the synthesised hydrogels were captured and are shown in Figure 6.7. The patterns look similar to the patterns formed on the hydrogel beads.

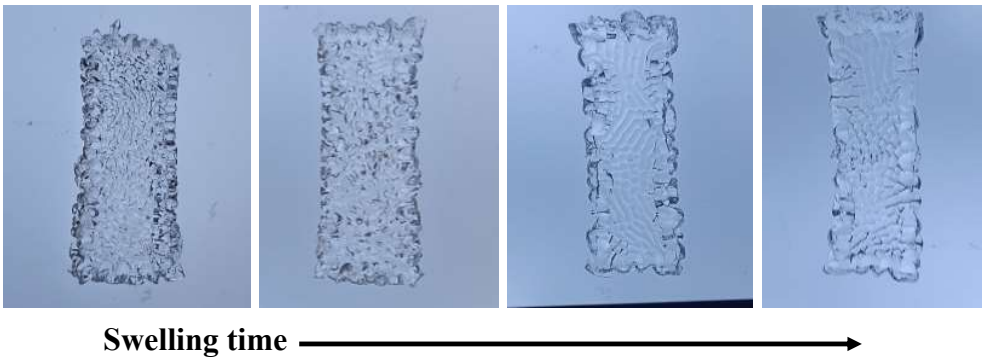

Figure 6.7: Swelling of polyacrylamide hydrogels. Images showing the variation in patterns formed on the synthesised hydrogels over the swelling time.

The swelling behaviour of these hydrogels is a crucial aspect that requires investigation, especially when comparing it to hydrogel beads. Additionally, the degree of cross-linking, controlled by the amount of cross-linker (potassium persulfate or KPS), plays a significant role in determining the swelling ratio of these hydrogels. However, this aspect warrants further exploration and study.

Once a better understanding of the factors influencing the swelling ratio is obtained, the question of how the curvature of thin hydrogel sheets or films impacts the patterns formed during the swelling process could be examined. This is an aspect that has received relatively little attention so far, but it holds the potential to reveal valuable insights into the behaviour of these hydrogels when they undergo swelling. Unfortunately, because of time limitations, notably those imposed by the COVID-19 pandemic, this particular aspect of the project was deferred to be addressed in future work.

6.4 Conclusion

This chapter highlighted some of the observations on the exploratory experiments on the swelling behaviour of thin films. In our study, we conducted experiments involving the synthesis and analysis of hydrogels, starting with gelatin and later transitioning to polyacrylamide hydrogels.

For gelatin, solutions with varying gelatin powder concentrations were prepared and assessed their swelling behaviour when exposed to salt solutions with different molarities. It was observed that gelatin swelled significantly in acidic conditions due to increased electrostatic repulsion between molecules, while it swelled less in neutral and alkaline conditions These results were compared with the results in the literature.

However, the attempts to create gelatin-based thin curved films led to brittleness and difficulties in controlling thickness. Consequently, the focus was shifted to polyacrylamide hydrogel beads, which are renowned for their water-absorption properties. We analysed the swelling behaviour of these beads, measuring diameter changes and capturing surface patterns during swelling.

Furthermore in this chapter, the impact of pH on the swelling kinetics of these hydrogel beads was explored. Lower pH levels led to quicker attainment of full swelling compared to higher pH levels. Additionally, we delved into the synthesis of polyacrylamide hydrogels, highlighting the key components involved in their creation, such as monomers, crosslinkers, and initiators. These hydrogels were synthesised using free radical polymerisation, resulting in stable polymer networks with varying properties. The patterns were observed on the surface of these hydrogels whose characteristics and features need more extensive study. Also, the effect of curvature on thin

hydrogel sheets or films on the patterns needs to be explored in the future.

Chapter 7

Summary and Future Work

This thesis has uncovered intriguing behaviours exhibited by wrinkling patterns in surfaces of various curvatures. In alignment with the project's objectives, a novel imaging technique was developed to delve into these patterns and scrutinise their distinctive characteristics will be elucidated. In this chapter, the primary findings from this thesis will be presented and the significance of these discoveries. Finally, I will conclude by highlighting potential research inquiries for future exploration.

7.1 Summary

7.1.1 Imaging of wrinkles

Chapter 3 introduced a practical and efficient approach for capturing images of wrinkled PDMS films on a water surface by utilising the optical displacement of features such as small dots projected through the film. This innovative technique was employed to discern key properties of these wrinkled films, specifically their height variations (amplitude) and the distances between wrinkles (wavelength). Using MATLAB, I solved the partial differential equation derived from optical theory to acquire height profiles and discern the characteristics of the wrinkled surface. I applied this methodology in experiments involving both positively and negatively curved thin films and provided insights into the iterative process of development, experimentation, and validation. I employed MATLAB to solve this equation, which was crucial for accurately assessing the characteristics of the wrinkles, including their amplitude and wavelength.

To ensure the reliability of our results, we included two validation methods that compared the computed surface profiles with known exact solutions. We also identified the limitations and constraints of our methodology. Ultimately, our developed approach allows for the dependable analysis of curved wrinkled films with an accuracy of better than 1% for surface slopes less than 10°. Additionally, our method is capable of reliably resolving wrinkle wavelengths as small as 1 mm using 10,000 random dots, or to a minimum wavelength of 0.5mm when employing 40,000 dots.

7.1.2 Effect of curvature on wrinkling patterns

In summary, chapter 4 thoroughly examined wrinkling patterns in thin curved films to understand how they work and gain valuable insights into the process of wrinkle scale selection.A dimensional analysis of the wrinkling shell system was made. This involved expressing the system in terms of dimensionless groups, which effectively balance the energetic contributions of various behaviours like bending, stretching, or buoyancy [14]. These dimensionless groups are pivotal for grasping the dynamics and interactions within the system, serving as indispensable tools for further analysis and interpretation.

Throughout this research, I devoted significant attention to observing how wrinkling patterns vary when curvature changes sign. This meticulous observation unveiled intriguing variations in the system's behaviour, highlighting the intricate interplay between geometry and material properties.

Another crucial facet of this investigation centred around the wrinkle wavelength parameter. By scrutinising wrinkle wavelength for both positive and negative Gaussian curvatures, it was found that the wavelength remains independent of curvature, in agreement with recent theoretical predictions. Additionally, I also confirmed that the dimensionless wrinkle wavelength (λ/Λ) equals 2π, as predicted by the elastica model [13, 155].

Furthermore, my analysis extended to examining how the wrinkle amplitude correlates with varying curvatures. A linear dependence between the wrinkle amplitude and Gaussian curvature was observed, where increasing curvature leads to increased amplitude to compensate for the increased excess area of the film. Additionally, I explored how amplitude varies from the centre of the film to its edges, noting differences between positive and negative Gaussian curvatures. For instance, wrinkle amplitude gradually decreases toward the edge for positive curvature, while it increases toward the edge for negative curvature. We also observed flattened regions near the centre and edges of the film, which diverged from theoretical predictions [15], possibly due to assumptions made in the theory, particularly the neglect of stretching energy.

This chapter also elucidated the emergence of wrinkle patterns on thin curved shells and reviewed the concept of stable lines [15] as an order parameter for predicting the type and layout of these patterns. Our experimental findings aligned with the literature's predictions [14, 15] regarding the patterns and paths of thin film wrinkles for both positive and negative curvatures.

By providing in-depth insights into wrinkling patterns, dimensionless groups, wrinkle wavelength, and amplitude behaviour, this study opens up new avenues in materials science, engineering, and related fields. The knowledge acquired here has the potential to revolutionise various real-world applications, including smart materials, stretchable electronics, and innovative surface

engineering techniques.

7.1.3 Patterns on photonic wafers

In Chapter 5, we explore the observations made on photonic wafers during the laser processing of thin films. The study focused on a silicon wafer and its oxide layer, including detailing the methods employed to prepare the samples. Laser-annealed samples were examined using an atomic force microscope to analyse the surface patterns. Additionally, the chapter outlines the subsequent processing and analysis steps carried out using Gwyddion and MATLAB.

During the research, collaboration with another research group led to the development of a numerical model of the thermal variations during the annealing process. This model played a crucial role in determining two key factors that influence the wrinkling pattern: the maximum temperature reached during the experiment and the thickness of the melted layers. These findings were essential in understanding the reasons behind the observed surface patterns.

It was noted that when the sample's temperature exceeded the melting points of the silicon and silica layers during laser pulsing, both layers briefly transformed into a liquid state. This allowed for the relaxation of thermal stresses that had accumulated in the layers due to heating from room temperature. Subsequently, residual stresses then built up as the once-molten layers cooled back to ambient conditions. This insight offers a clear explanation for the driving forces behind the emergence of the observed surface patterns.

Our study contributes to a deeper understanding of the complex relationship between temperature, material properties, and the formation of surface patterns. This research is an ongoing project, with plans for further advancement. To enhance the accuracy of the numerical model, ongoing efforts aim to refine the step size used in calculations, enabling more precise measurements of the thickness of the melted layer.

7.1.4 Patterns on hydrogels

Chapter 6 presents findings from our exploratory experiments on the swelling behaviour of thin films. Our research involved conducting experiments in which we synthesised and analysed the swelling behaviour of hydrogels, initially using gelatin and later transitioning to polyacrylamide hydrogels.

With gelatin, we prepared solutions containing varying concentrations of gelatin powder and examined how they swelled when exposed to salt solutions with different molarities and pH. We observed that gelatin exhibited significant swelling in acidic conditions due to increased electrostatic repulsion between its molecules. In contrast, it exhibited less swelling in neutral

and alkaline conditions.

However, our attempts to create thin curved films using gelatin led to issues with brittleness and thickness control. As a result, we shifted our focus to polyacrylamide hydrogel beads, well-known for their water-absorption properties [185]. We conducted an analysis of the swelling behaviour of these beads, measuring changes in diameter and documenting surface patterns during the swelling process.

Furthermore, we explored the influence of pH on the swelling kinetics of these hydrogel beads. Lower pH levels resulted in a faster achievement of full swelling, compared to higher pH levels. Additionally, we delved into the synthesis of polyacrylamide hydrogels, emphasising the essential components involved in their creation, including monomers, crosslinkers, and initiators. These hydrogels were synthesised using free radical polymerisation, resulting in stable polymer networks with varying properties. We also observed patterns on the surface of these hydrogels, the characteristics and features of which warrant further in-depth study. Additionally, there is a need for future exploration regarding the impact of curvature on the patterns formed in thin hydrogel sheets or films.

Bibliography

[1] Eran Sharon, Michael Marder, and Harry L Swinney. Leaves, flowers and garbage bags: Making waves. *American Scientist*, 92(3):254–261, 2004.

[2] Michael Allen. Physics of brain folding recreated in the lab – Physics World — physicsworld.com. https://physicsworld.com/a/physics-of-brain-folding-recreated-in-the-lab/, 2016. [Accessed 25-09-2023].

[3] Jiangshui Huang, Megan Juszkiewicz, Wim H De Jeu, Enrique Cerda, Todd Emrick, Narayanan Menon, and Thomas P Russell. Capillary wrinkling of floating thin polymer films. *Science*, 317(5838):650–653, 2007.

[4] Andrew K Schulz, Madeline Boyle, Colin Boyle, Sophia Sordilla, Catalina Rincon, Scott Hooper, Catie Aubuchon, Joy S Reidenberg, Claire Higgins, and David L Hu. Skin wrinkles and folds enable asymmetric stretch in the elephant trunk. *Proceedings of the National Academy of Sciences*, 119(31):e2122563119, 2022.

[5] Bo Li, Yan-Ping Cao, Xi-Qiao Feng, and Huajian Gao. Mechanics of morphological instabilities and surface wrinkling in soft materials: a review. *Soft Matter*, 8(21):5728–5745, 2012.

[6] Joseph D Paulsen, Vincent Démery, K Buğra Toga, Zhanlong Qiu, Thomas P Russell, Benny Davidovitch, and Narayanan Menon. Geometry-driven folding of a floating annular sheet. *Physical Review Letters*, 118(4):048004, 2017.

[7] A Cutolo, V Pagliarulo, F Merola, S Coppola, P Ferraro, and M Fraldi. Wrinkling prediction, formation and evolution in thin films adhering on polymeric substrata. *Materials & Design*, 187:108314, 2020.

[8] Yinlong Tan, Biru Hu, Jia Song, Zengyong Chu, and Wenjian Wu. Bioinspired multiscale wrinkling patterns on curved substrates: An overview. *Nano-Micro Letters*, 12:1–42, 2020.

[9] Long Ma, Linghui He, and Yong Ni. Tunable hierarchical wrinkling: From models to applications. *Journal of Applied Physics*, 127(11):111101, 03 2020.

[10] Stephanie Hiltl and Alexander Böker. Wetting phenomena on (gradient) wrinkle substrates. *Langmuir*, 32(35):8882–8888, 2016.

[11] Euroextrusions Ltd. Thermoforming. Available at http://www.euroextrusions.com/thermoforming/ (2023/01/16).

[12] Kaili Xie, Alizée Glasser, Shekhar Shinde, Zaicheng Zhang, Jean-Michel Rampnoux, Abdelhamid Maali, Eric Cloutet, Georges Hadziioannou, and Hamid Kellay. Delamination and wrinkling of flexible conductive polymer thin films. *Advanced Functional Materials*, 31(21):2009039, 2021.

[13] O Albarran, DV Todorova, E Katifori, and L Goehring. Curvature controlled pattern formation in floating shells. *ArXiv:1806.03718*, 2018.

[14] Ian Tobasco, Yousra Timounay, Desislava Todorova, Graham C Leggat, Joseph D. Paulsen, and Eleni Katifori. Exact solutions for the wrinkle patterns of confined elastic shells. *Nature Physics*, 18:1099–1104, 2022.

[15] Ian Tobasco. Curvature-driven wrinkling of thin elastic shells. *Archive for Rational Mechanics and Analysis*, 239:1211–1325, 2021.

[16] Ned Bowden, Scott Brittain, Anthony G Evans, John W Hutchinson, and George M Whitesides. Spontaneous formation of ordered structures in thin films of metals supported on an elastomeric polymer. *Nature*, 393(6681):146–149, 1998.

[17] Brigham Young University. Oxide Growth Calculator — cleanroom.byu.edu. https://cleanroom.byu.edu/oxidetimecalc, 2023. [Accessed 28-09-2023].

[18] Brian J Simonds, Helene J Meadows, Sudhajit Misra, Christos Ferekides, Phillip J Dale, and Michael A Scarpulla. Laser processing for thin film chalcogenide photovoltaics: a review and prospectus. *Journal of Photonics for Energy*, 5(1):050999–050999, 2015.

[19] Maria Bercea. Bioinspired hydrogels as platforms for life-science applications: Challenges and opportunities. *Polymers*, 14(12):2365, 2022.

[20] Shu Yang, Krishnacharya Khare, and Pei-Chun Lin. Harnessing surface wrinkle patterns in soft matter. *Advanced Functional Materials*, 20(16):2550–2564, 2010.

[21] Juan Rodriguez-Hernandez. Wrinkled interfaces: Taking advantage of surface instabilities to pattern polymer surfaces. *Progress in Polymer Science*, 42:1–41, 2015.

[22] Farzaneh Sabbagh and Ida Idayu Muhamad. Acrylamide-based hydrogel drug delivery systems: release of acyclovir from mgo nanocomposite hydrogel. *Journal of the Taiwan Institute of Chemical Engineers*, 72:182–193, 2017.

[23] Evan Hohlfeld and L. Mahadevan. Scale and nature of sulcification patterns. *Physical Review Letters*, 109:025701, 2012.

[24] Enrique Cerda and Lakshminarayanan Mahadevan. Geometry and physics of wrinkling. *Physical Review Letters*, 90(7):074302, 2003.

[25] Jie Yin, Gregory J Gerling, and Xi Chen. Mechanical modeling of a wrinkled fingertip immersed in water. *Acta Biomaterialia*, 6(4):1487–1496, 2010.

[26] Eleni Katifori, Silas Alben, Enrique Cerda, David R Nelson, and Jacques Dumais. Foldable structures and the natural design of pollen grains. *Proceedings of the National Academy of Sciences*, 107(17):7635–7639, 2010.

[27] Jan Genzer and Jan Groenewold. Soft matter with hard skin: From skin wrinkles to templating and material characterization. *Soft Matter*, 2:310–323, 2006.

[28] P. Ball. *The Self-made Tapestry: Pattern Formation in Nature*. Oxford University Press, 2001.

[29] Ilka Straehler-Pohl, Chad L Widmer, Andre C Morandini, et al. Characterizations of juvenile stages of some semaeostome scyphozoa (cnidaria), with recognition of a new family (phacellophoridae). *Zootaxa*, 2741(1):1–37, 2011.

[30] Charles R Steele. Shell stability related to pattern formation in plants. *Journal of Applied Mechanics*, 67(2):237–247, 2000.

[31] Dahl-Young Khang, Hanqing Jiang, Young Huang, and John A Rogers. A stretchable form of single-crystal silicon for high-performance electronics on rubber substrates. *Science*, 311(5758):208–212, 2006.

[32] Sk. Faruque Ahmed, Geon-Ho Rho, Kwang-Ryeol Lee, Ashkan Vaziri, and Myoung-Woon Moon. High aspect ratio wrinkles on a soft polymer. *Soft Matter*, 6:5709–5714, 2010.

[33] Ned Bowden, Wilhelm TS Huck, Kateri E Paul, and George M Whitesides. The controlled formation of ordered, sinusoidal structures by plasma oxidation of an elastomeric polymer. *Applied Physics Letters*, 75(17):2557–2559, 1999.

[34] J Song, Hanqing Jiang, ZJ Liu, DY Khang, Y Huang, JA Rogers, C Lu, and CG1169 Koh. Buckling of a stiff thin film on a compliant substrate in large deformation. *International Journal of Solids and Structures*, 45(10):3107–3121, 2008.

[35] B. Audoly and Y. Pomeau. *Elasticity and Geometry: From Hair Curls to the Non-linear Response of Shells*. OUP Oxford, 2010.

[36] Z.Y. Huang, W. Hong, and Z. Suo. Nonlinear analyses of wrinkles in a film bonded to a compliant substrate. *Journal of the Mechanics and Physics of Solids*, 53(9):2101–2118, 2005.

[37] Gang Xu, Philip V Bayly, and Larry A Taber. Residual stress in the adult mouse brain. *Biomechanics and Modeling in Mechanobiology*, 8:253–262, 2009.

[38] Patrick D. Shipman and Alan C. Newell. Phyllotactic patterns on plants. *Physical Review Letters*, 92:168102, 2004.

[39] C. R. Steele. Shell Stability Related to Pattern Formation in Plants . *Journal of Applied Mechanics*, 67(2):237–247, 1999.

[40] Amy E. Shyer, Tuomas Tallinen, Nandan L. Nerurkar, Zhiyan Wei, Eun Seok Gil, David L. Kaplan, Clifford J. Tabin, and L. Mahadevan. Villification: How the gut gets its villi. *Science*, 342(6155):212–218, 2013.

[41] Evan Benjamin Hohlfeld. *Creasing, point-bifurcations, and the spontaneous breakdown of scale-invariance*. Harvard University, 2008.

[42] Lihua Jin, Shengqiang Cai, and Zhigang Suo. Creases in soft tissues generated by growth. *Europhysics Letters*, 95(6):64002, 2011.

[43] PV Bayly, LA Taber, and CD Kroenke. Mechanical forces in cerebral cortical folding: a review of measurements and models. *Journal of the Mechanical Behavior of Biomedical Materials*, 29:568–581, 2014.

[44] W Yang, TC Fung, KS Chian, and CK Chong. Instability of the two-layered thick-walled esophageal model under the external pressure and circular outer boundary condition. *Journal of Biomechanics*, 40(3):481–490, 2007.

[45] Xi Chen and John W Hutchinson. Herringbone buckling patterns of compressed thin films on compliant substrates. *Journal of Applied Mechanics*, 71(5):597–603, 2004.

[46] Mai T Lam, Sylvie Sim, Xiaoyue Zhu, and Shuichi Takayama. The effect of continuous wavy micropatterns on silicone substrates on the alignment of skeletal muscle myoblasts and myotubes. *Biomaterials*, 27(24):4340–4347, 2006.

[47] Won Mook Choi, Jizhou Song, Dahl-Young Khang, Hanqing Jiang, Yonggang Y Huang, and John A Rogers. Biaxially stretchable "wavy" silicon nanomembranes. *Nano Letters*, 7(6):1655–1663, 2007.

[48] Won Hoe Koo, Soon Moon Jeong, Fumito Araoka, Ken Ishikawa, Suzushi Nishimura, Takehiro Toyooka, and Hideo Takezoe. Light extraction from organic light-emitting diodes enhanced by spontaneously formed buckles. *Nature Photonics*, 4:222–226, 2010.

[49] Dae-Hyeong Kim, Jong-Hyun Ahn, Won Mook Choi, Hoon-Sik Kim, Tae-Ho Kim, Jizhou Song, Yonggang Y Huang, Zhuangjian Liu, Chun Lu, and John A Rogers. Stretchable and foldable silicon integrated circuits. *Science*, 320(5875):507–511, 2008.

[50] Enrique Cerda, K Ravi-Chandar, and L Mahadevan. Wrinkling of an elastic sheet under tension. *Nature*, 419(6907):579–580, 2002.

[51] Krassimir D Danov, Peter A Kralchevsky, and Simeon D Stoyanov. Elastic langmuir layers and membranes subjected to unidirectional compression: wrinkling and collapse. *Langmuir*, 26(1):143–155, 2010.

[52] Jérémy Hure, Benoît Roman, and José Bico. Stamping and wrinkling of elastic plates. *Physical review letters*, 109(5):054302, 2012.

[53] Chi-Mon Chen and Shu Yang. Wrinkling instabilities in polymer films and their applications. *Polymer International*, 61(7):1041–1047, 2012.

[54] Pil J Yoo and Hong H Lee. Morphological diagram for metal/polymer bilayer wrinkling: Influence of thermomechanical properties of polymer layer. *Macromolecules*, 38(7):2820–2831, 2005.

[55] Hyun Suk Kim and Alfred J. Crosby. Solvent-responsive surface via wrinkling instability. *Advanced Materials*, 23(36):4188–4192, 2011.

[56] E.P. Chan, E.J. Smith, R.C. Hayward, and A.J. Crosby. Surface wrinkles for smart adhesion. *Advanced Materials*, 20(4):711–716, 2008.

[57] Jun Young Chung, Adam J Nolte, and Christopher M Stafford. Surface wrinkling: a versatile platform for measuring thin-film properties. *Advanced Materials*, 23(3):349–368, 2011.

[58] Takuya Ohzono and Masatsugu Shimomura. Ordering of microwrinkle patterns by compressive strain. *Physical Review B*, 69(13):132202, 2004.

[59] Christopher M Stafford, Christopher Harrison, Kathryn L Beers, Alamgir Karim, Eric J Amis, Mark R VanLandingham, Ho-Cheol Kim, Willi Volksen, Robert D Miller, and Eva E Simonyi. A buckling-based metrology for measuring the elastic moduli of polymeric thin films. *Nature Materials*, 3(8):545–550, 2004.

[60] Takuya Ohzono, Hirosato Monobe, and Yo Shimizu. Liquid crystal alignment on self-organized microwrinkles. *Applied Physics Express*, 1(6):065001, 2008.

[61] Michael P. Hitchman. GCT Curvature — mphitchman.com. https://mphitchman.com/geometry/section7-1.html#:~:text=The%20curvature%20of%20the%20curve,the%20curve%20at%20this%20point. [Accessed 17-09-2023].

[62] Thomas F Banchoff and Stephen Lovett. *Differential geometry of curves and surfaces*. CRC Press, 2022.

[63] Norbert Stoop, Romain Lagrange, Denis Terwagne, Pedro M. Reis, and Jörn Dunkel. Curvature-induced symmetry breaking determines elastic surface patterns. *Nature Materials*, 14:337–342, 2015.

[64] Francisco López Jiménez, Norbert Stoop, Romain Lagrange, Jörn Dunkel, and Pedro M Reis. Curvature-controlled defect localization in elastic surface crystals. *Physical Review Letters*, 116(10):104301, 2016.

[65] Norbert Stoop, Romain Lagrange, Denis Terwagne, Pedro M Reis, and Jörn Dunkel. Curvature-induced symmetry breaking determines elastic surface patterns. *Nature Materials*, 14(3):337–342, 2015.

[66] Qiming Wang and Xuanhe Zhao. Phase diagrams of instabilities in compressed film-substrate systems. *Journal of Applied Mechanics*, 81(5):051004, 2014.

[67] Qiming Wang and Xuanhe Zhao. A three-dimensional phase diagram of growth-induced surface instabilities. *Scientific Reports*, 5(1):8887, 2015.

[68] Anesia Auguste, Lihua Jin, Zhigang Suo, and Ryan C Hayward. Post-wrinkle bifurcations in elastic bilayers with modest contrast in modulus. *Extreme Mechanics Letters*, 11:30–36, 2017.

[69] R Zhao, T Zhang, M Diab, H Gao, and K-S Kim. The primary bilayer ruga-phase diagram i: Localizations in ruga evolution. *Extreme Mechanics Letters*, 4:76–82, 2015.

[70] Jan Genzer and Jan Groenewold. Soft matter with hard skin: From skin wrinkles to templating and material characterization. *Soft Matter*, 2(4):310–323, 2006.

[71] Guoxin Cao, Xi Chen, Chaorong Li, Ailing Ji, and Zexian Cao. Self-assembled triangular and labyrinth buckling patterns of thin films on spherical substrates. *Physical Review Letters*, 100(3):036102, 2008.

[72] Yan Zhao, Yanping Cao, Xi-Qiao Feng, and Kang Ma. Axial compression-induced wrinkles on a core–shell soft cylinder: Theoretical analysis, simulations and experiments. *Journal of the Mechanics and Physics of Solids*, 73:212–227, 2014.

[73] Run Wang, Nan Jiang, Jian Su, Qu Yin, Yue Zhang, Zhongsheng Liu, Haibao Lin, Francisco A Moura, Ningyi Yuan, Siegmar Roth, et al. A bi-sheath fiber sensor for giant tensile and torsional displacements. *Advanced Functional Materials*, 27(35):1702134, 2017.

[74] Jie Yin, Eyal Bar-Kochba, and Xi Chen. Mechanical self-assembly fabrication of gears. *Soft Matter*, 5(18):3469–3474, 2009.

[75] Yan-Ping Cao, Bo Li, and Xi-Qiao Feng. Surface wrinkling and folding of core–shell soft cylinders. *Soft Matter*, 8(2):556–562, 2012.

[76] Tianjiao Ma, Jing Bai, Tiantian Li, Shuai Chen, Xiaodong Ma, Jie Yin, and Xuesong Jiang. Light-driven dynamic surface wrinkles for adaptive visible camouflage. *Proceedings of the National Academy of Sciences*, 118(48):e2114345118, 2021.

[77] Senta Schauer, Raphael Schmager, Ruben Hünig, Kaining Ding, Ulrich W Paetzold, Uli Lemmer, Matthias Worgull, Hendrik Hölscher, and Guillaume Gomard. Disordered diffraction gratings tailored by shape-memory based wrinkling and their application to photovoltaics. *Optical Materials Express*, 8(1):184–198, 2018.

[78] Fudong Li, Honghao Hou, Jie Yin, and Xuesong Jiang. Near-infrared light–responsive dynamic wrinkle patterns. *Science Advances*, 4(4):eaar5762, 2018.

[79] Jong Bok Kim, Pilnam Kim, Nicolas C Pégard, Soong Ju Oh, Cherie R Kagan, Jason W Fleischer, Howard A Stone, and Yueh-Lin Loo. Wrinkles and deep folds as photonic structures in photovoltaics. *Nature Photonics*, 6(5):327–332, 2012.

[80] Jiale Yong, Qing Yang, Feng Chen, Dongshi Zhang, Umar Farooq, Guangqing Du, and Xun Hou. A simple way to achieve superhydrophobicity, controllable water adhesion, anisotropic sliding, and anisotropic wetting based on femtosecond-laser-induced line-patterned surfaces. *Journal of Materials Chemistry A*, 2(15):5499–5507, 2014.

[81] Dongjoon Rhee, Won-Kyu Lee, and Teri W Odom. Crack-free, soft wrinkles enable switchable anisotropic wetting. *Angewandte Chemie*, 129(23):6623–6627, 2017.

[82] Baolai Jiang, Luntao Liu, Zongpeng Gao, and Wenshou Wang. A general and robust strategy for fabricating mechanoresponsive surface wrinkles with dynamic switchable transmittance. *Advanced Optical Materials*, 6(13):1800195, 2018.

[83] Myoung-Woon Moon and Ashkan Vaziri. Wrinkling instability and its applications: From biomimetic tilted pillars to optics grating. *Procedia Engineering*, 10:224–227, 2011. 11th International Conference on the Mechanical Behavior of Materials (ICM11).

[84] Tianjiao Ma, Shuai Chen, Jin Li, Jie Yin, and Xuesong Jiang. Strain-ultrasensitive surface wrinkles for visual optical sensors. *Mater. Horiz.*, 9:2233–2242, 2022.

[85] Kartikeya Walia, Ahmed Khan, and Philip Breedon. Polymer-based additive manufacturing: Process optimisation for low-cost industrial robotics manufacture. *Polymers*, 13(16):2809, 2021.

[86] N. Shahrubudin, T.C. Lee, and R. Ramlan. An overview on 3d printing technology: Technological, materials, and applications. *Procedia Manufacturing*, 35:1286–1296, 2019. The 2nd International Conference on Sustainable Materials Processing and Manufacturing, SMPM 2019, 8-10 March 2019, Sun City, South Africa.

[87] Formlabs. Formlabs Customer Support — support.formlabs.com. https://support.formlabs.com/s/article/Form-Wash-Time-Settings?language=en_US, 2023. [Accessed 13-09-2023].

[88] Formlabs. Formlabs Customer Support — support.formlabs.com. https://support.formlabs.com/s/article/Form-Cure-Time-and-Temperature-Settings?language=en_US, 2022. [Accessed 13-09-2023].

[89] Bastien Venzac, Shanliang Deng, Ziad Mahmoud, Aufried Lenferink, Aurélie Costa, Fabrice Bray, Cees Otto, Christian Rolando, and Séverine Le Gac. Pdms curing inhibition on 3d-printed molds: Why? also, how to avoid it? *Analytical Chemistry*, 93(19):7180–7187, 2021.

[90] Smooth-On. Inhibit X™ Product Information — smooth-on.com. https://www.smooth-on.com/products/inhibit-x/, 2023. [Accessed 13-09-2023].

[91] P.J. Martin. *12 - Thermoforming of polymers*. Woodhead Publishing, 2009.

[92] ID Johnston, MC Tracey, JB Davis, and CKL Tan. Micro throttle pump employing displacement amplification in an elastomeric substrate. *Journal of Micromechanics and Microengineering*, 15(10):1831, 2005.

[93] Erwin Berthier, Edmond WK Young, and David Beebe. Engineers are from pdms-land, biologists are from polystyrenia. *Lab on a Chip*, 12(7):1224–1237, 2012.

[94] Kiran Raj M and Suman Chakraborty. Pdms microfluidics: A mini review. *Journal of Applied Polymer Science*, 137(27):48958, 2020.

[95] Weiqiang Chen, Raymond HW Lam, and Jianping Fu. Photolithographic surface micromachining of polydimethylsiloxane (pdms). *Lab on a Chip*, 12(2):391–395, 2012.

[96] Andrews Victor, JE Ribeiro, and Fernando F Araújo. Study of pdms characterization and its applications in biomedicine: A review. *Journal of Mechanical Engineering and Biomechanics*, 4(1):1–9, 2019.

[97] Tiziana Bardelli, Claudia Marano, and Francesco Briatico Vangosa. Polydimethylsiloxane crosslinking kinetics: A systematic study on sylgard184 comparing rheological and thermal approaches. *Journal of Applied Polymer Science*, 138(39):51013, 2021.

[98] Angelina Müller, Matthias C Wapler, and Ulrike Wallrabe. A quick and accurate method to determine the poisson's ratio and the coefficient of thermal expansion of pdms. *Soft Matter*, 15(4):779–784, 2019.

[99] Arnaud Hemmerle, Yuta Yamaguchi, Marcin Makowski, Oliver Bäumchen, and Lucas Goehring. Measuring and upscaling micromechanical interactions in a cohesive granular material. *Soft Matter*, 17(23):5806–5814, 2021.

[100] A. Lee, P.T. Brun, J. Marthelot, G. Balestra, F. Gallaire, and P. M. Reis. Fabrication of slender elastic shells by the coating of curved surfaces. *Nature Communications*, 7(11155), 2016.

[101] Wolfgang Drexler and James G Fujimoto. *Optical coherence tomography: technology and applications*. Springer Science & Business Media, 2008.

[102] Selin Manukyan, Hans M Sauer, Ilia V Roisman, Kyle A Baldwin, David J Fairhurst, Haida Liang, Joachim Venzmer, and Cameron Tropea. Imaging internal flows in a drying sessile polymer dispersion drop using spectral radar optical coherence tomography (sr-oct). *Journal of Colloid and Interface Science*, 395:287–293, 2013.

[103] James G Fujimoto, Wolfgang Drexler, Joel S Schuman, and Christoph K Hitzenberger. Optical coherence tomography (oct) in ophthalmology: introduction. *Optics Express*, 17(5):3978–3979, 2009.

[104] Chi Cheung and Haida Liang. Ultra-high resolution Fourier domain optical coherence tomography for resolving thin layers in painted works of art. *Proc SPIE*, 8790:10145–10157, 05 2013.

[105] CS Cheung, M Spring, and H Liang. Ultra-high resolution fourier domain optical coherence tomography for old master paintings. *Optics Express*, 23(8):10145–10157, 2015.

[106] Samuel Lawman and Haida Liang. High precision dynamic multi-interface profilometry with optical coherence tomography. *Applied Optics*, 50(32):6039–6048, 2011.

[107] Ee Hou Yong, David R. Nelson, and L. Mahadevan. Elastic platonic shells. *Physical Review Letters*, 111:177801, 2013.

[108] A. Cutolo, V. Pagliarulo, F. Merola, S. Coppola, P. Ferraro, and M. Fraldi. Wrinkling prediction, formation and evolution in thin films adhering on polymeric substrata. *Materials and Design*, 187:108314, 2020.

[109] Jun Young Chung, Adam J Nolte, and Christopher M Stafford. Diffusion-controlled, self-organized growth of symmetric wrinkling patterns. *Advanced Materials*, 21(13):1358–1362, 2009.

[110] Hugues Vandeparre, Sylvain Gabriele, Fabian Brau, Cyprien Gay, Kevin Kit Parker, and Pascal Damman. Hierarchical wrinkling patterns. *Soft Matter*, 6(22):5751–5756, 2010.

[111] Tomo Veldin, Boštjan Brank, and Miha Brojan. Computational finite element model for surface wrinkling of shells on soft substrates. *Communications in Nonlinear Science and Numerical Simulation*, 78:104863, 2019.

[112] AL Volynskii, S Bazhenov, OV Lebedeva, and NF Bakeev. Mechanical buckling instability of thin coatings deposited on soft polymer substrates. *Journal of Materials Science*, 35:547–554, 2000.

[113] R Huang. Kinetic wrinkling of an elastic film on a viscoelastic substrate. *Journal of the Mechanics and Physics of Solids*, 53(1):63–89, 2005.

[114] Hanqing Jiang, Dahl-Young Khang, Jizhou Song, Yugang Sun, Yonggang Huang, and John A Rogers. Finite deformation mechanics in buckled thin films on compliant supports. *Proceedings of the National Academy of Sciences*, 104(40):15607–15612, 2007.

[115] X Sun, G Zhang, Q Shi, B Tang, and ZJ Wu. Preparation and characterization of water-swellable natural rubbers. *Journal of Applied Polymer Science*, 86:3212–717, 2002.

[116] Qiming Wang, Lin Zhang, and Xuanhe Zhao. Creasing to cratering instability in polymers under ultrahigh electric fields. *Physical Review Letters*, 106(11):118301, 2011.

[117] Lihua Jin, Anesia Auguste, Ryan C Hayward, and Zhigang Suo. Bifurcation diagrams for the formation of wrinkles or creases in soft bilayers. *Journal of Applied Mechanics*, 82(6):061008, 2015.

[118] Jinook Kim and Hong H Lee. Wave formation by heating in thin metal film on an elastomer. *Journal of Polymer Science Part B: Polymer Physics*, 39(11):1122–1128, 2001.

[119] Pil J Yoo. Fabrication of complexly patterned wavy structures using self-organized anisotropic wrinkling. *Electronic Materials Letters*, 7:17–23, 2011.

[120] Pil J Yoo and Hong H Lee. Evolution of a stress-driven pattern in thin bilayer films: Spinodal wrinkling. *Physical Review Letters*, 91(15):154502, 2003.

[121] Pei-Chun Lin and Shu Yang. Spontaneous formation of one-dimensional ripples in transit to highly ordered two-dimensional herringbone structures through sequential and unequal biaxial mechanical stretching. *Applied Physics Letters*, 90(24):241903, 2007.

[122] Bernhard A. Glatz, Moritz Tebbe, Badr Kaoui, Roland Aichele, Christian Kuttner, Andreas E. Schedl, Hans-Werner Schmidt, Walter Zimmermann, and Andreas Fery. Hierarchical line-defect patterns in wrinkled surfaces. *Soft Matter*, 11:3332–3339, 2015.

[123] Joseph D. Paulsen, Evan Hohlfeld, Hunter King, Jiangshui Huang, Zhanlong Qiu, Thomas P. Russell, Narayanan Menon, Dominic Vella, and Benny Davidovitch. Curvature-induced stiffness and the spatial variation of wavelength in wrinkled sheets. *Proceedings of the National Academy of Sciences*, 113(5):1144–1149, 2016.

[124] Johannes Schindelin, Ignacio Arganda-Carreras, Erwin Frise, Verena Kaynig, Mark Longair, Tobias Pietzsch, Stephan Preibisch, Curtis Rueden, Stephan Saalfeld, Benjamin Schmid, et al. Fiji: an open-source platform for biological-image analysis. *Nature Methods*, 9(7):676–682, 2012.

[125] Sulaiman Mad-Ali, Soottawat Benjakul, Thummanoon Prodpran, and Sajid Maqsood. Characteristics and gelling properties of gelatin from goat skin as affected by drying methods. *Journal of Food Science and Technology*, 54:1646–1654, 2017.

[126] IV Yannas and AV Tobolsky. High-temperature transformations of gelatin. *European Polymer Journal*, 4(2):257–264, 1968.

[127] G David Scott and D Marc Kilgour. The density of random close packing of spheres. *Journal of Physics D: Applied Physics*, 2(6):863, 1969.

[128] Vasili Baranau and Ulrich Tallarek. Random-close packing limits for monodisperse and polydisperse hard spheres. *Soft Matter*, 10(21):3826–3841, 2014.

[129] A. Goriely, D. E. Moulton, and R. Vandiver. Elastic cavitation, tube hollowing, and differential growth in plants and biological tissues. *Europhysics Letters*, 91(1):18001, 2010.

[130] Julien Dervaux and Martine Ben Amar. Morphogenesis of growing soft tissues. *Physical Review Letters*, 101:068101, 2008.

[131] Sujit S. Datta, Shin-Hyun Kim, Jayson Paulose, Alireza Abbaspourrad, David R. Nelson, and David A. Weitz. Delayed buckling and guided folding of inhomogeneous capsules. *Physical Review Letters*, 109:134302, 2012.

[132] P. Ciarletta, V. Balbi, and E. Kuhl. Pattern selection in growing tubular tissues. *Physical Review Letters*, 113:248101, 2014.

[133] Xi Chen and Jie Yin. Buckling patterns of thin films on curved compliant substrates with applications to morphogenesis and three-dimensional micro-fabrication. *Soft Matter*, 6:5667–5680, 2010.

[134] Paul B Green. Expression of pattern in plants: combining molecular and calculus-based biophysical paradigms. *American Journal of Botany*, 86(8):1059–1076, 1999.

[135] P. B. GREEN, C. S. STEELE, and S. C. RENNICH. Phyllotactic Patterns: A Biophysical Mechanism for their Origin. *Annals of Botany*, 77(5):515–528, 1996.

[136] Bo Li, Yan-Ping Cao, Xi-Qiao Feng, and Huajian Gao. Mechanics of morphological instabilities and surface wrinkling in soft materials: a review. *Soft Matter*, 8:5728–5745, 2012.

[137] Mir Jalil Razavi, Tuo Zhang, Tianming Liu, and Xianqiao Wang. Cortical folding pattern and its consistency induced by biological growth. *Scientific Reports*, 5(1):14477, 2015.

[138] Yosra A Fouda and Ahmed A El Mansi. Skin pattern structure and function of juvenile ages of chameleo chameleon. *Egyptian Journal of Basic and Applied Sciences*, 4(1):22–29, 2017.

[139] Soumendra K Basu, Alon V McCormick, and LE Scriven. Stress generation by solvent absorption and wrinkling of a cross-linked coating atop a viscous or elastic base. *Langmuir*, 22(13):5916–5924, 2006.

[140] Derek Breid and Alfred J Crosby. Surface wrinkling behavior of finite circular plates. *Soft Matter*, 5(2):425–431, 2009.

[141] Takuya Ohzono and Masatsugu Shimomura. Geometry-dependent stripe rearrangement processes induced by strain on preordered microwrinkle patterns. *Langmuir*, 21(16):7230–7237, 2005.

[142] Siavash Nikravesh and Yu-Lin Shen. Evolution of thin-film wrinkle patterns on a soft substrate: Direct simulations and the effects of the deformation history. *Nanomaterials*, 12(19):3505, 2022.

[143] Yan Zhao, Hanlin Zhu, Chao Jiang, Yanping Cao, and Xi-Qiao Feng. Wrinkling pattern evolution on curved surfaces. *Journal of the Mechanics and Physics of Solids*, 135:103798, 2020.

[144] Fei Jia, Simon P Pearce, and Alain Goriely. Curvature delays growth-induced wrinkling. *Physical Review E*, 98(3):033003, 2018.

[145] Hillel Aharoni, Desislava V. Todorova, Octavio Albarrán, Lucas Goehring, Randall D. Kamien, and Eleni Katifori. The smectic order of wrinkles. *Nature Communications*, page 15809, 2017.

[146] J Clerk Maxwell. Xlv. on reciprocal figures and diagrams of forces. *The London, Edinburgh, and Dublin Philosophical Magazine and Journal of Science*, 27(182):250–261, 1864.

[147] Edgar Buckingham. On physically similar systems; illustrations of the use of dimensional equations. *Physical Review*, 4(4):345, 1914.

[148] G.I. Barenblatt and P. Makinen. *Dimensional Analysis*. Gordon and Breach Science Publishers, 1987.

[149] Ain A. Sonin. A generalization of the π-theorem and dimensional analysis. *Proceedings of the National Academy of Sciences*, 101(23):8525–8526, 2004.

[150] Karl Friedrich Gauss and Peter Pesic. *General investigations of curved surfaces*. Courier Corporation, 2005.

[151] Barrett O'neill. *Elementary differential geometry*. Elsevier, 2006.

[152] Jana Kalová and Radim Mareš. Reference values of surface tension of water. *International Journal of Thermophysics*, 36:1396–1404, 2015.

[153] Hamid Ebrahimi, Amin Ajdari, Dominic Vella, Arezki Boudaoud, and Ashkan Vaziri. Anisotropic blistering instability of highly ellipsoidal shells. *Physical Review Letters*, 112(9):094302, 2014.

[154] L Pauchard and S Rica. Contact and compression of elastic spherical shells: the physics of a 'ping-pong'ball. *Philosophical Magazine B*, 78(2):225–233, 1998.

[155] Benny Davidovitch, Yiwei Sun, and Gregory M Grason. Geometrically incompatible confinement of solids. *Proceedings of the National Academy of Sciences*, 116(5):1483–1488, 2019.

[156] Lev Davidovich Landau, Evgenii Mikhailovich Lifshitz, Arnold Markovich Kosevich, and Lev Petrovich Pitaevskii. *Theory of elasticity: volume 7*, volume 7. Elsevier, 1986.

[157] Hunter King, Robert D Schroll, Benny Davidovitch, and Narayanan Menon. Elastic sheet on a liquid drop reveals wrinkling and crumpling as distinct symmetry-breaking instabilities. *Proceedings of the National Academy of Sciences*, 109(25):9716–9720, 2012.

[158] Finn Box, Doireann O'Kiely, Ousmane Kodio, Maxime Inizan, Alfonso A Castrejón-Pita, and Dominic Vella. Dynamics of wrinkling in ultrathin elastic sheets. *Proceedings of the National Academy of Sciences of the United States of America*, 116:20875–20880, 2019.

[159] Gilbert Strang. *Calculus v1*. OpenStax, 2020.

[160] Fu-Chien Chiu, Tung-Ming Pan, Tapas Kumar Kundu, Chun-Hsing Shih, et al. Thin film applications in advanced electron devices, 2014.

[161] KL Choy. Chemical vapour deposition of coatings. *Progress in Materials Science*, 48(2):57–170, 2003.

[162] G Khrypunov, A Romeo, F Kurdesau, DL Bätzner, H Zogg, and Ayodhya N Tiwari. Recent developments in evaporated cdte solar cells. *Solar Energy Materials and Solar Cells*, 90(6):664–677, 2006.

[163] Mehran Arbab and James J Finley. Glass in architecture. *International Journal of Applied Glass Science*, 1(1):118–129, 2010.

[164] N Setter, D Damjanovic, L Eng, G Fox, Spartak Gevorgian, S Hong, A Kingon, H Kohlstedt, NY Park, GB Stephenson, et al. Ferroelectric thin films: Review of materials, properties, and applications. *Journal of Applied Physics*, 100(5):051606, 2006.

[165] Pascal M Seiler, Galina Georgieva, Georg Winzer, Anna Peczek, Karsten Voigt, Stefan Lischke, Adel Fatemi, and Lars Zimmermann. Toward coherent o-band data center interconnects. *Frontiers of Optoelectronics*, 14:414–425, 2021.

[166] Jing Shang, Fang Cheng, Manish Dubey, Justin M Kaplan, Meghana Rawal, Xi Jiang, David S Newburg, Philip A Sullivan, Rodrigo B Andrade, and Daniel M Ratner. An organophosphonate strategy for functionalizing silicon photonic biosensors. *Langmuir*, 28(6):3338–3344, 2012.

[167] Anna Cattani-Scholz, Daniel Pedone, Manish Dubey, Stefan Neppl, Bert Nickel, Peter Feulner, Jeffrey Schwartz, Gerhard Abstreiter, and Marc Tornow. Organophosphonate-based pna-functionalization of silicon nanowires for label-free dna detection. *ACS Nano*, 2(8):1653–1660, 2008.

[168] T Fukuda. Handbook of sensors and actuators. *Micro Mechanical Systems (Principles and Technology)*, 6, 1998.

[169] Zujun Shi, Shiqian Shao, and Yi Wang. Improved the surface roughness of silicon nanophotonic devices by thermal oxidation method. In *Journal of Physics: Conference Series*, volume 276, page 012087. IOP Publishing, 2011.

[170] WM Cranton, N Kalfagiannis, X Hou, R Ranson, DC Koutsogeorgis, et al. Enhanced electrical and optical properties of room temperature deposited aluminium doped zinc oxide (azo) thin films by excimer laser annealing. *Optics and Lasers in Engineering*, 80:45–51, 2016.

[171] Emre Yarali, Christina Koutsiaki, Hendrik Faber, Kornelius Tetzner, Emre Yengel, Panos Patsalas, Nikolaos Kalfagiannis, Demosthenes C Koutsogeorgis, and Thomas D Anthopoulos. Recent progress in photonic processing of metal-oxide transistors. *Advanced Functional Materials*, 30(20):1906022, 2020.

[172] Ya'nan Wang, Yi Luo, Changzheng Sun, Bing Xiong, Jian Wang, Zhibiao Hao, Yanjun Han, Lai Wang, and Hongtao Li. Laser annealing of sio 2 film deposited by icpecvd for fabrication of silicon based low loss waveguide. *Frontiers of Optoelectronics*, 9:323–329, 2016.

[173] B Gallas, C-C Kao, S Fisson, G Vuye, J Rivory, Y Bernard, and C Belouet. Laser annealing of siox thin films. *Applied Surface Science*, 185(3-4):317–320, 2002.

[174] S.O. El hamali, W.M. Cranton, N. Kalfagiannis, X. Hou, R. Ranson, and D.C. Koutsogeorgis. Enhanced electrical and optical properties of room temperature deposited aluminium

doped zinc oxide (azo) thin films by excimer laser annealing. *Optics and Lasers in Engineering*, 80:45–51, 2016.

[175] Baoyi Wu, Huanhuan Lu, Xiaoxia Le, Wei Lu, Jiawei Zhang, Patrick Théato, and Tao Chen. Recent progress in the shape deformation of polymeric hydrogels from memory to actuation. *Chemical Science*, 12(19):6472–6487, 2021.

[176] Gilles Barast, Andry-Rico Razakamanantsoa, Irini Djeran-Maigre, Timothy Nicholson, and David Williams. Swelling properties of natural and modified bentonites by rheological description. *Applied Clay Science*, 142:60–68, 2017.

[177] Lee Jones, Vanessa Banks, and Ian Jefferson. Chapter 8 swelling and shrinking soils. *Geological Society, London, Engineering Geology Special Publications*, 29(1):223–242, 2020.

[178] Friederike Katharina Metze, Sabrina Sant, Zhao Meng, Harm-Anton Klok, and Kuljeet Kaur. Swelling-activated, soft mechanochemistry in polymer materials. *Langmuir*, 39(10):3546–3557, 2023.

[179] T Komori and R Sakamoto. On tanaka-fillmore's kinetics swelling of gels. *Colloid and Polymer Science*, 267:179–183, 1989.

[180] Kuen Yong Lee and David J Mooney. Hydrogels for tissue engineering. *Chemical Reviews*, 101(7):1869–1880, 2001.

[181] Jeroen Leijten, Jungmok Seo, Kan Yue, Grissel Trujillo-de Santiago, Ali Tamayol, Guillermo U Ruiz-Esparza, Su Ryon Shin, Roholah Sharifi, Iman Noshadi, Mario Moisés Álvarez, et al. Spatially and temporally controlled hydrogels for tissue engineering. *Materials Science and Engineering: R: Reports*, 119:1–35, 2017.

[182] Ruijiao Dong, Yan Pang, Yue Su, and Xinyuan Zhu. Supramolecular hydrogels: synthesis, properties and their biomedical applications. *Biomaterials Science*, 3(7):937–954, 2015.

[183] Carl A Eckelman. *The shrinking and swelling of wood and its effect on furniture*. Purdue University Cooperative Extension Service, 1998.

[184] Dina A Emarah and Safwat A Seleem. Swelling soils treatment using lime and sea water for roads construction. *Alexandria Engineering Journal*, 57(4):2357–2365, 2018.

[185] Thibault Bertrand, Jorge Peixinho, Shomeek Mukhopadhyay, and Christopher W MacMinn. Dynamics of swelling and drying in a spherical gel. *Physical Review Applied*, 6(6):064010, 2016.

[186] Etienne Reyssat and Lakshminarayanan Mahadevan. Hygromorphs: from pine cones to biomimetic bilayers. *Journal of the Royal Society Interface*, 6(39):951–957, 2009.

[187] LA Setton, H Tohyama, and VC Mow. Swelling and curling behaviors of articular cartilage. *Journal of Biomedical Enegineering*, pages 355–361, 1998.

[188] Julien Dervaux and Martine Ben Amar. Mechanical instabilities of gels. *Annual Reviews of Condensed Matter Physics*, 3(1):311–332, 2012.

[189] Mahdi Askari-Sedeh and Mostafa Baghani. ph-sensitive hydrogel bilayers: Investigation on transient swelling-induced bending through analytical and fem approaches. *Gels*, 9(7):563, 2023.

[190] Leonid Ionov. Biomimetic hydrogel-based actuating systems. *Advanced Functional Materials*, 23(36):4555–4570, 2013.

[191] Enas M. Ahmed. Hydrogel: Preparation, characterization, and applications: A review. *Journal of Advanced Research*, 6(2):105–121, 2015.

[192] Nikolas A Peppas, P Bures, WS Leobandung, and H Ichikawa. Hydrogels in pharmaceutical formulations. *European Journal of Pharmaceutics and Biopharmaceutics*, 50(1):27–46, 2000.

[193] Zhijie Sui, William J King, and William L Murphy. Protein-based hydrogels with tunable dynamic responses. *Advanced Functional Materials*, 18(12):1824–1831, 2008.

[194] Panupong Jaipan, Alexander Nguyen, and Roger J Narayan. Gelatin-based hydrogels for biomedical applications. *Mrs Communications*, 7(3):416–426, 2017.

[195] Kuljit Kaur, Rajeev Jindal, and Dhruvi Jindal. Controlled release of vitamin b1 and evaluation of biodegradation studies of chitosan and gelatin based hydrogels. *International Journal of Biological Macromolecules*, 146:987–999, 2020.

[196] Wen Zhao, Xing Jin, Yang Cong, Yuying Liu, and Jun Fu. Degradable natural polymer hydrogels for articular cartilage tissue engineering. *Journal of Chemical Technology & Biotechnology*, 88(3):327–339, 2013.

[197] Peter Krsko, Thomas E McCann, Thu-Trang Thach, Tracy L Laabs, Herbert M Geller, and Matthew R Libera. Length-scale mediated adhesion and directed growth of neural cells by surface-patterned poly (ethylene glycol) hydrogels. *Biomaterials*, 30(5):721–729, 2009.

[198] Ling Zhang, Kuifeng Li, Wenqian Xiao, Li Zheng, Yumei Xiao, Hongsong Fan, and Xingdong Zhang. Preparation of collagen–chondroitin sulfate–hyaluronic acid hybrid hydrogel scaffolds and cell compatibility in vitro. *Carbohydrate Polymers*, 84(1):118–125, 2011.

[199] Toyoichi Tanaka and David J Fillmore. Kinetics of swelling of gels. *The Journal of Chemical Physics*, 70(3):1214–1218, 1979.

[200] Xingkun Man and Masao Doi. Swelling dynamics of a disk-shaped gel. *Macromolecules*, 54(10):4626–4632, 2021.

[201] Hans Schott. Kinetics of swelling of polymers and their gels. *Journal of Pharmaceutical Sciences*, 81(5):467–470, 1992.

[202] Douglas P Holmes and Alfred J Crosby. Snapping surfaces. *Advanced Materials*, 19(21):3589–3593, 2007.

[203] Toyoichi Tanaka, Shao-Tang Sun, Yoshitsugu Hirokawa, Seiji Katayama, John Kucera, Yoshiharu Hirose, and Takayuki Amiya. Mechanical instability of gels at the phase transition. *Nature*, 325(6107):796–798, 1987.

[204] Verónica Trujillo, Jungwook Kim, and Ryan C Hayward. Creasing instability of surface-attached hydrogels. *Soft Matter*, 4(3):564–569, 2008.

[205] Jan Groenewold. Wrinkling of plates coupled with soft elastic media. *Physica A: Statistical Mechanics and its Applications*, 298(1-2):32–45, 2001.

[206] Kirill Efimenko, Mindaugas Rackaitis, Evangelos Manias, Ashkan Vaziri, L Mahadevan, and Jan Genzer. Nested self-similar wrinkling patterns in skins. *Nature Materials*, 4(4):293–297, 2005.

[207] Maria Tenje, Federico Cantoni, Ana María Porras Hernández, Sean S Searle, Sofia Johansson, Laurent Barbe, Maria Antfolk, and Hannah Pohlit. A practical guide to microfabrication and patterning of hydrogels for biomimetic cell culture scaffolds. *Organs-on-a-Chip*, 2:100003, 2020.

[208] Julien Barthes, Hayriye Özçelik, Mathilde Hindié, Albana Ndreu-Halili, Anwarul Hasan, Nihal Engin Vrana, et al. Cell microenvironment engineering and monitoring for tissue engineering and regenerative medicine: the recent advances. *BioMed Research International*, 2014:921905, 2014.

[209] Bin Xu and Ryan C Hayward. Low-voltage switching of crease patterns on hydrogel surfaces. *Advanced Materials*, 25(39):5555–5559, 2013.

[210] Luiz E Bertassoni, Martina Cecconi, Vijayan Manoharan, Mehdi Nikkhah, Jesper Hjortnaes, Ana Luiza Cristino, Giada Barabaschi, Danilo Demarchi, Mehmet R Dokmeci, Yunzhi Yang, et al. Hydrogel bioprinted microchannel networks for vascularization of tissue engineering constructs. *Lab on a Chip*, 14(13):2202–2211, 2014.

[211] Xuhao Fan, Chunsan Deng, Hui Gao, Binzhang Jiao, Yuncheng Liu, Fayu Chen, Leimin Deng, and Wei Xiong. 3d printing of nanowrinkled architectures via laser direct assembly. *Science Advances*, 8(31):eabn9942, 2022.

[212] VN Pandey, Neha Tiwari, VS Pandey, Anita Rao, and Ishwar Das. Targeted drug delivery and gene therapy through natural biodegradable nanostructures in pharmaceuticals. In *Nanoarchitectonics in biomedicine*, pages 437–472. Elsevier, 2019.

[213] Tanbir Ahmad, Amin Ismail, Siti Aqlima Ahmad, Khalilah A Khalil, Yogesh Kumar, Kazeem D Adeyemi, and Awis Q Sazili. Recent advances on the role of process variables affecting gelatin yield and characteristics with special reference to enzymatic extraction: A review. *Food Hydrocolloids*, 63:85–96, 2017.

[214] Jong-Whan Rhim, Hwan-Man Park, and Chang-Sik Ha. Bio-nanocomposites for food packaging applications. *Progress in Polymer Science*, 38(10-11):1629–1652, 2013.

[215] Michelly CG Pellá, Otavio A Silva, Matheus G Pellá, Adriana G Beneton, Josiane Caetano, Márcia R Simões, and Douglas C Dragunski. Effect of gelatin and casein additions on starch edible biodegradable films for fruit surface coating. *Food Chemistry*, 309:125764, 2020.

[216] Akira Hayashi and Shin-Chol Oh. Gelation of gelatin solution. *Agricultural and Biological Chemistry*, 47(8):1711–1716, 1983.

[217] Hossein Montazerian, Avijit Baidya, Reihaneh Haghniaz, Elham Davoodi, Samad Ahadian, Nasim Annabi, Ali Khademhosseini, and Paul S Weiss. Stretchable and bioadhesive gelatin methacryloyl-based hydrogels enabled by in situ dopamine polymerization. *ACS Applied Materials & Interfaces*, 13(34):40290–40301, 2021.

[218] Ting Zhang, Jiamin Xu, Yangyi Zhang, Xichang Wang, José M Lorenzo, and Jian Zhong. Gelatins as emulsifiers for oil-in-water emulsions: Extraction, chemical composition, molecular structure, and molecular modification. *Trends in Food Science & Technology*, 106:113–131, 2020.

[219] KJ Goudie, SJ McCreath, JA Parkinson, CM Davidson, and JJ Liggat. Investigation of the influence of ph on the properties and morphology of gelatin hydrogels. *Journal of Polymer Science*, 2023.

[220] Xian Jin Yang, Pei Jie Zheng, Zhen Duo Cui, Nai Qin Zhao, Yu Fen Wang, and Kang De Yao. Swelling behaviour and elastic properties of gelatin gels. *Polymer International*, 44(4):448–452, 1997.

[221] Hansoo Park, Xuan Guo, Johnna S Temenoff, Yasuhiko Tabata, Arnold I Caplan, F Kurtis Kasper, and Antonios G Mikos. Effect of swelling ratio of injectable hydrogel composites on chondrogenic differentiation of encapsulated rabbit marrow mesenchymal stem cells in vitro. *Biomacromolecules*, 10(3):541–546, 2009.

[222] Mahnaz Amiri, Payam Khazaeli, Ali Salehabadi, and Masoud Salavati-Niasari. Hydrogel beads-based nanocomposites in novel drug delivery platforms: Recent trends and developments. *Advances in Colloid and Interface Science*, 288:102316, 2021.

[223] George Odian. *Principles of polymerization*. John Wiley & Sons, 2004.

[224] Nishi Panchal, Dhruv Patel, and Nimish Shah. Synthesis of hydrogels. In *4th international conference on multidisciplinary research & practice (4ICMRP-2017)*, pages 64–72, 2017.

[225] Enrica Caló and Vitaliy V Khutoryanskiy. Biomedical applications of hydrogels: A review of patents and commercial products. *European Polymer Journal*, 65:252–267, 2015.

[226] Marcus J Caulfield, Greg G Qiao, and David H Solomon. Some aspects of the properties and degradation of polyacrylamides. *Chemical Reviews*, 102(9):3067–3084, 2002.